Accelerometer Calibration for Next Generation Gravity Mission

Srujan Vaidya

Delft University of Technology

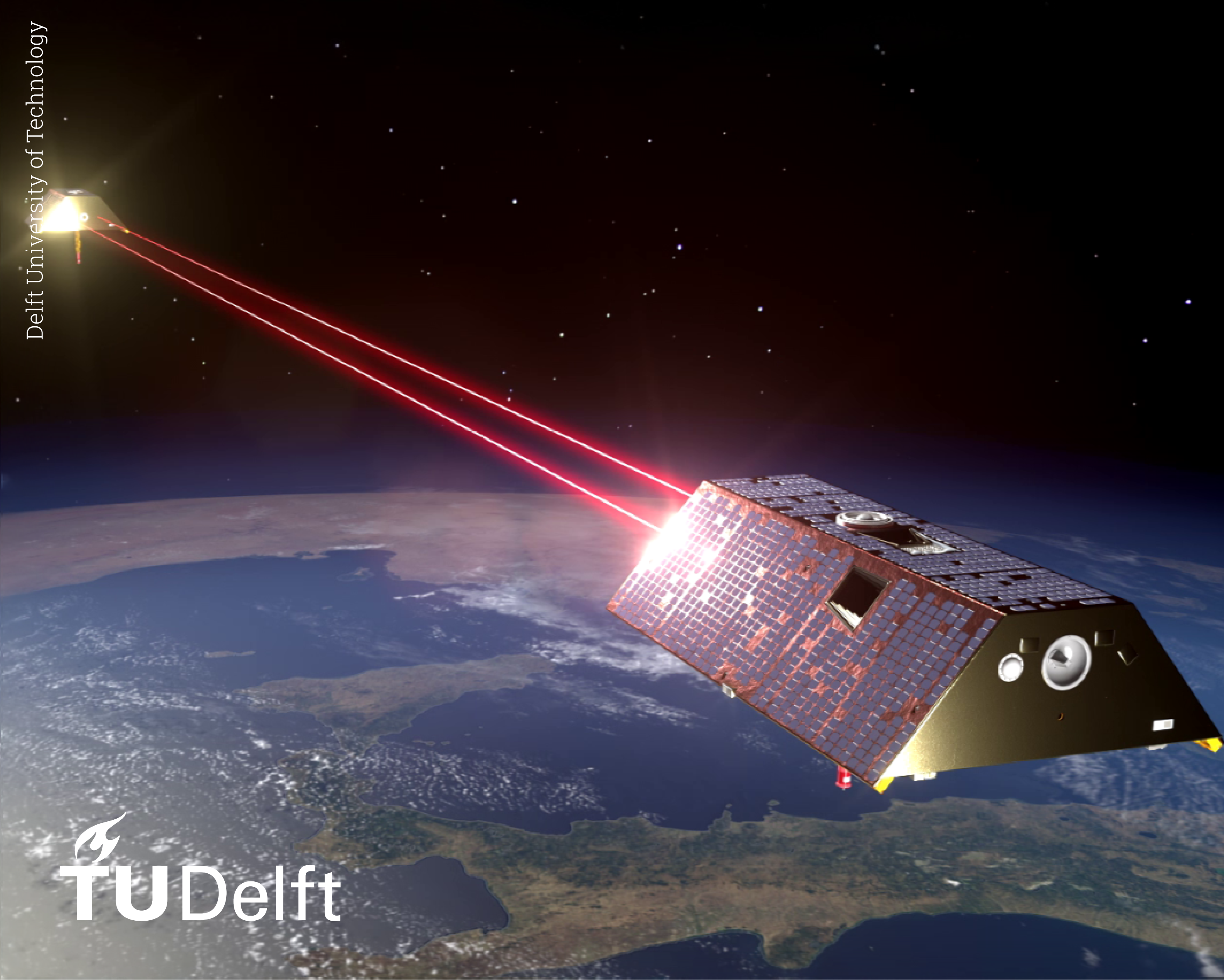

Accelerometer Calibration for Next Generation Gravity Mission

by

Srujan Vaidya

to obtain the degree of Master of Science
at the Faculty of Aerospace Engineering,
Delft University of Technology,
to be defended publicly on Monday, April 14, 2025 at 1:00 PM.

Student Number:	5072034	
Thesis Committee:	Dr.ir. E.J.O. Schrama	TU Delft, Committee chair
	Dr.ir. J.G. De Teixeira da Encarnação	TU Delft, Supervisor
	Dr.ing. C. Siemes	TU Delft, Supervisor
	Dr. S. Gehly	TU Delft, External examiner

Cover: Inter Satellite Laser Ranging (credit: DLR)

Acknowledgements

With this report, I find myself at the end of an incredible five-year chapter as a student at TU Delft. These years have been filled with challenges, growth, and invaluable experiences that I will carry with me. I would like to express my deepest gratitude to my supervisors, Christian Siemes and João Encarnação. Their guidance, expertise, and patience have been instrumental in shaping this thesis. I am also deeply grateful to my family for their unwavering support and belief in me, even from afar. Their encouragement has been my foundation throughout this journey. To my friends, thank you for making this journey truly memorable. As I close this chapter and look ahead to new opportunities, I do so with immense gratitude for the people and experiences that have shaped me along the way.

Srujan Vaidya
Delft, April 2025

Contents

Abstract

This study investigates the calibration of accelerometer data for the Next Generation Gravity Mission (NGGM), proposed by the European Space Agency. With improved precision, NGGM aims to continue gravity field observations beyond the Gravity Recovery and Climate Experiment Follow-On (GRACE-FO) mission. The mission consists of a satellite pair measuring Earth's gravity field using an onboard laser tracking instrument. To isolate the gravity field signature in these observations, each satellite carries accelerometers to estimate non-gravitational accelerations. This thesis supports the accelerometer calibration process by applying lessons from previous gravity field missions.

A historical review of gravity missions highlights the evolution of scientific and hardware requirements. The study examines accelerometer principles, sources of instrumental imperfections, and existing data calibration techniques. NGGM's preliminary design includes multiple accelerometers placed away from the satellite's center of mass, allowing the use of shaking manoeuvres—first introduced in the GOCE mission—for calibration.

A comprehensive model is developed that can generate shaking manoeuvres with varying thrust magnitudes, shaking durations, and shaking frequencies to excite the satellite. This model is used in conjunction with various accelerometer units (two, three, and four accelerometer layouts are considered) and their placement in the satellite's body frame to evaluate the calibration quality against the scientific requirements posed for the mission.

Results indicate that along-track accelerometer placement minimizes non-gravitational acceleration measurement errors due to enhanced centrifugal acceleration from the satellite's pitch rate during calibration. Furthermore, the along-track placement performs better than radial placement, even though it has the same centrifugal acceleration boost. The suspected cause is the electrode layout of the accelerometer, which boosts the acceleration signal due to the projection of the angular acceleration about the y-axis onto the z component of the linear acceleration. The radial placement of the accelerometers provides no additional signal to the x-component of the linear acceleration due to a lack of projection. Lower shaking frequencies improve calibration by accumulating higher angular rates over time. However, due to volume constraints imposed by the laser tracking instrument, cross-track placement may be more favourable. This configuration requires higher thrust levels, as the absence of a pitch rate signal on the cross-track axis worsens the signal-to-noise ratio of the observations, which warrants a revision of the thruster requirements and accelerometer performance. Moreover, more than two accelerometers reduce measurement errors by providing redundancy in the observations. Even with three accelerometers placed in the along-track direction, at least 24 hours of shaking at maximum thrust, as stated by the thruster requirement, is required for effective calibration. Lower thrust or shorter shaking durations would necessitate four accelerometers, two on the x-axis and two on the y-axis. Finally, the accelerometer pair's arm length is treated as a free variable, as it has minimal impact on calibration performance.

This report provides foundational insight for future gravity missions. Smart accelerometer placement and shaking manoeuvre parameters can improve the measurement quality of the non-gravitational forces and subsequently improve gravity field recovery, which is crucial for tackling the climate crisis.

List of Figures

List of Tables

Abbreviations

Notation	Description
ASD	Amplitude Spectral Density
CCD	Charged-Coupled Device
CHAMP	Challenging Mini-Satellite Payload
CMOS	Complementary Metal-Oxide Semiconductor
COM	Center of Mass
DCT	Drag Control Thruster
DFACS	Drag-Free and Attitude Control System
DLR	Deutsches Zentrum für Luft- und Raumfahrt
DORIS	Doppler Orbitography and Radiopositioning
DTU	Danmarks Tekniske Universitet
DWS	Differential Wavefront Sensor
EGG	Electrostatic Gravity Gradiometer
ESA	European Space Agency
FCT	Fine Control Thruster
FFT	Fast Fourier Transform
FSM	Fast Steering Mirror
GNSS	Global Navigation Satellite System
GOCE	Gravity Field and Steady-State Ocean Circulation Explorer
GPS	Global Positioning System
GRACE	Gravity Recovery and Climate Experiment
GRACE-FO	GRACE Follow On
IQR	Inter-Quartile Range
LEO	Low Earth Orbit
LIGO	Laser Interferometer Gravitational-Wave Observatory
LISA	Laser Interferometer Space Antenna
LL-SST	Low-Low Satellite-to-Satellite Tracking
LoS	Line of Sight
LRI	Laser Ranging Interferometer
LTI	Laser Tracking Instrument
MAGIC	Mass change And Geosciences International Constellation
MBW	Measurement Bandwidth
MWI	Microwave Instrument

Notation	Description
NASA	National Aeronautics and Space Administration
NGGM	Next Generation Gravity Mission
PID	Proportional-Integrative-Derivative
POD	Precise Orbit Determination
PSD	Power Spectral Density
RMS	Root Mean Square
SLR	Satellite Laser Ranging
SNR	Signal-to-Noise ratio
TMA	Triple Mirror Assembly

Symbols

Symbol	Description	Units
a	Semi-major axis of an orbit	$[km]$
$\boldsymbol{V}$	Gravity gradient tensor	$[1/s^2]$
$A(f)$	Amplitude spectral density of a given variable	$[Amp/\sqrt{Hz}]$
df	Frequency bin width	$[Hz]$
f_{LB}	Lower bound frequency of the shaking signal	$[Hz]$
f_{UB}	Upper bound frequency of the shaking signal	$[Hz]$
f	Frequency	$[Hz]$
f_s	Sampling frequency	$[Hz]$
F_{cap}	Capacitive force	$[N]$
$F_{x,y,z}$	Linear force acting on the satellite's COM	$[N]$
$\boldsymbol{M}$	External moment acting on the satellite	$[Nm]$
$V_d(t)$	AC detection voltage of proof mass	$[V]$
V_p	DC polarisation voltage of proof mass	$[V]$
V	Control voltage of electrodes	$[V]$
E_i	Electric field between the proof mass and electrode plates	$[V/m]$
P_{BW}	Power of a signal in a given frequency band	$[W]$
P	Power of a signal in frequency domain	$[W]$
ω	Argument of periapsis of an orbit	[°]
i	Inclination of an orbit	[°]
Ω	Longitude of ascending node of an orbit	[°]
θ	True anomaly of an orbit or angle between two vectors	[°]
ρ	Atmospheric density at current satellite position	$[kg/m^3]$
$\dot{m}$	Fuel mass rate of the thruster	$[kg/s]$
R_E	Radius of Earth	$[km]$
h	Altitude of an orbit	$[km]$
μ	Gravitational parameter of Earth	$[km^3/s^2]$
Δd_G	Distance variation between two satellites' COM due to gravitational forces	$[m]$
Δd_D	Distance variation between two satellites' COM due to non-gravitational forces	$[m]$
Δd	Total distance variation between two satellite's COM	$[m]$
d	Gap size between the proof mass and electrode	$[m]$
L_x, L_y, L_z	Gradiometer arm length in x, y or z direction	$[m]$

L_{ISR}	Inter-satellite range	$[m]$
$\boldsymbol{r}_{cij}^{np}$	Nominal position in common mode	$[m]$
$\boldsymbol{r}_{dij}^{np}$	Nominal position in differential mode	$[m]$
$\boldsymbol{r}_{i}^{np}$	Nominal position of an accelerometer	$[m]$
$\delta\boldsymbol{r}_i$	Deviation from nominal position	$[m]$
$\boldsymbol{r}_{Es}$	Position of satellite relative to Earth in the pseudo-inertial J2000 frame	$[m]$
$\boldsymbol{r}_i$	Real position of an accelerometer	$[m]$
S_{ref}	Reference area of the satellite	$[m]$
c	Speed of light in vacuum	$[m/s]$
v_{air}	Satellite's airspeed w.r.t. Earth's atmosphere	$[m/s]$
$\boldsymbol{a}_{ng}^{rcst}$	Reconstructed non-gravitational acceleration	$[m/s^2]$
$\boldsymbol{a}_{ng}^{true}$	True non-gravitational acceleration	$[m/s^2]$
$a_{sh}(t)$	Shaking acceleration time series	$[m/s^2]$
$\boldsymbol{b}_{cij}$	Common mode acceleration bias	$[m/s^2]$
$\boldsymbol{b}_{dij}$	Differential mode acceleration bias	$[m/s^2]$
$\boldsymbol{b}_i$	Acceleration bias	$[m/s^2]$
$\boldsymbol{a}_{i}^{cal,np}$	Calibrated acceleration at nominal position	$[m/s^2]$
$\boldsymbol{a}_{i}^{cal}$	Calibrated acceleration at real position	$[m/s^2]$
$\boldsymbol{a}_{cij}$	Common mode acceleration at real position	$[m/s^2]$
$\Delta\ddot{d}_D$	Non-gravitational acceleration difference between two satellites COM	$[m/s^2]$
$\boldsymbol{a}_{dij}$	Differential mode acceleration at real position	$[m/s^2]$
$\epsilon_{ng,LoS,rel}$	Relative non-gravitational acceleration measurement error of the pair projected onto the Line of Sight	$[m/s^2]$
$\epsilon_{ng,LoS,i}$	Non-gravitational acceleration measurement error projected onto the Line of Sight for a satellite	$[m/s^2]$
$\boldsymbol{\epsilon}_{ng}$	Non-gravitational acceleration measurement error	$[m/s^2]$
g	Gravitational acceleration	$[m/s^2]$
g_0	Gravitational acceleration at sea level	$[m/s^2]$
$\boldsymbol{a}_{cij}^{meas}$	Measured common mode acceleration	$[m/s^2]$
$\boldsymbol{a}_{dij}^{meas}$	Measured differential mode acceleration	$[m/s^2]$
$\boldsymbol{a}_{i}^{meas}$	Measured acceleration by an accelerometer	$[m/s^2]$
$\boldsymbol{n}_{cij}$	Common mode measurement noise	$[m/s^2]$
$\boldsymbol{n}_{dij}$	Differential mode measurement noise	$[m/s^2]$
$\boldsymbol{n}_i$	Measurement noise	$[m/s^2]$
$\boldsymbol{a}_{cij}^{np}$	True common mode acceleration at nominal position	$[m/s^2]$
$\boldsymbol{a}_{dij}^{np}$	True differential mode acceleration at nominal position	$[m/s^2]$
$\boldsymbol{a}_{i}^{np}$	True acceleration at nominal position	$[m/s^2]$
$\boldsymbol{a}_{ng}$	Non-gravitational acceleration	$[m/s^2]$

$\ddot{\boldsymbol{r}}_{aero}$	Aerodynamic acceleration acting on the satellite in the inertial frame	[m/s^2]
$\ddot{\boldsymbol{r}}_{ng}$	Non-gravitational acceleration exerted by Earth on the satellite in the pseudo-inertial J2000 frame	[m/s^2]
$\ddot{\boldsymbol{r}}_{rad}$	Radiation pressure acceleration acting on the satellite in the inertial frame	[m/s^2]
$\ddot{\boldsymbol{r}}_{tot}$	Total acceleration exerted acting on the satellite's COM in the pseudo-inertial frame J2000 frame	[m/s^2]
$\boldsymbol{a}_i$	True acceleration at real position	[m/s^2]
$w(t)$	White noise using a standard normal distribution or Symmetric impulse response in time domain	[m/s^2]
T_{acc}	Thrust acceleration magnitude of shaking signal ASD in acceleration units per square root of frequency	[$m/s^2/\sqrt{Hz}$]
A	Area of the electrode plate	[m^2]
$\Sigma_{\boldsymbol{y}}$	Noise covariance matrix	[m^2/s^4]
$\boldsymbol{\Omega}$	Angular rate matrix	[rad/s]
$\boldsymbol{\omega}_i$	True angular rates	[rad/s]
$\dot{\boldsymbol{\Omega}}$	Angular acceleration matrix	[rad/s^2]
$\dot{\boldsymbol{\omega}}_i$	True angular acceleration	[rad/s^2]
I_{sp}	Specific impulse of the thruster	[s]
$\boldsymbol{K}_i$	Diagonal quadratic factor matrix	[s^2/m]
$\boldsymbol{x}$	Calibration parameters vector	[s^2/m]
u	Inverse of the amplitude spectral density of a given variable	[$unit/\sqrt{Hz}$]
$\boldsymbol{J}$	Jacobian/Design matrix of a generalised least-squares fit or Mass moment of inertia of the satellite	[-,kgm^2]
C_r	Radiation pressure coefficient of the satellite	[-]
$\Delta\bar{\boldsymbol{y}}$	Decorrelated reduced observation vector	[-]
$\Delta\boldsymbol{y}$	Reduced observation vector	[-]
G	Matrix containing the effect of gravity gradients, centrifugal, and Euler accelerations	[-]
$\bar{\boldsymbol{J}}$	Decorrelated Jacobian/Design matrix of a generalised least-squares fit	[-]
$\boldsymbol{J}^{ext}$	Jacobian/Design matrix of a generalised least-squares fit extended	[-]
$\boldsymbol{S}$	Diagonal scale factor matrix	[-]
$\boldsymbol{W}_{cij}$	Angular acceleration coupling matrix common mode	[-]
$\boldsymbol{W}_{dij}$	Angular acceleration coupling matrix differential mode	[-]
$\boldsymbol{W}_i$	Angular acceleration coupling matrix	[-]
BW	Bandwidth of the shaking signal rectangular pulse	[-]
$\boldsymbol{M}_{cij}$	Calibration matrix of common mode	[-]
$\boldsymbol{M}_{dij}$	Calibration matrix of differential mode	[-]
$\boldsymbol{M}_i$	Calibration matrix containing scale factors, misalignments and non-orthogonality of sensitive axes	[-]

C_D	Drag coefficient in satellite's aerodynamic frame	[-]
e	Eccentricity of an orbit	[-]
ϵ_0	Dielectric constant	[-]
k	Power ratio between high frequency and low frequency ASD filter	[-]
$Q1$	First quartile of the data	[-]
$Q3$	Third quartile of the data	[-]
$\boldsymbol{q}$	Quaternions	[-]
$\boldsymbol{R}^{I/AF}$	Rotation matrix from satellite's aerodynamic frame to inertial frame	[-]
σ_i	Standard deviation of estimated parameter from least sqaures.	[-]
v	Impulse response	[-]
N	Window length in Welch's method for estimating Amplitude Spectral Density (ASD)	[-]
$\boldsymbol{x}^{(ext)}$	Calibration parameters vector extended	[-]
$\boldsymbol{x}_0$	Approximation of calibration parameters vector	[-]
$\boldsymbol{x}_B$	x-axis of body-fixed frame	[-]
$\hat{\boldsymbol{x}}_0$	Updated calibration parameters vector	[-]
$\boldsymbol{y}_0$	Observation vector of approximated data of a generalised least-squares fit	[-]
$\boldsymbol{x}_B$	y-axis of body-fixed frame	[-]
$\boldsymbol{y}$	Observation vector of measured data of a generalised least-squares fit	[-]
$\boldsymbol{x}_B$	z-axis of body-fixed frame	[-]
t_{sh}	Shaking duration	[hrs]
m	Satellite's mass	[kg]

1

Introduction

Since the early 2000s, the field of space geodesy has made a giant leap. For the first time, measuring Earth's gravity globally and consistently with high accuracy was possible. By measuring both spatial and temporal variations of gravity, one could get a deeper understanding of the underlying dynamics of mass changes in the interior and on the surface of the Earth. It allows us to monitor processes such as water-cycle changes, sea level rise and glacial activity (Chen et al., 2006; National Research Council et al., 1997; Tapley et al., 2019), which have become increasingly important recently against the backdrop of climate change and global warming.

In the very early stages of spaceflight, analysis of deviations from a Keplerian orbit induced by the local gravity field made it possible to determine the flattening and pear shape of the Earth corresponding to the lower degree and order coefficients of the spherical harmonic representation of Earth's gravity field (O'Keefe et al., 1959). In the following years, with greater coverage of Earth with more satellites, increased global distribution of tracking stations, and the improvement of satellite tracking technology like Satellite Laser Ranging (SLR) (D. E. Smith et al., 1972; Strugarek et al., 2019), Doppler Orbitography and Radiopositioning (DORIS) (Willis et al., 2010), and Global Navigation Satellite System (GNSS) (Y. Bock & Melgar, 2016; Strugarek et al., 2019) provided greater resolution and thus determination of higher order terms (Flechtner et al., 2021; Kornfeld et al., 2019). However, extracting gravity data as a tertiary objective with the use of satellites reached its natural limits due to insufficient accurate observations and modelling of non-gravitational forces such as atmospheric drag and solar and Earth radiation pressure (Flechtner et al., 2021). Thus, this warranted the need for dedicated gravitational field missions.

The following features were envisaged for these dedicated missions (Flechtner et al., 2021):

1. Low Earth Orbit (LEO) satellites with altitudes between 250 and 500 km.
2. Global coverage of Earth by using polar circular orbits.
3. Uninterrupted 3D determination of position through high-low satellite orbit tracking.
4. Recording of non-gravitational forces acting on the satellite with high-precision accelerometers.
5. Using observation techniques such as low-low satellite-to-satellite tracking or in-situ measurement of gravitational gradients for dedicated measurement of gravitational field signal.

The first flight of a French-made ASTRE electrostatic accelerometer aboard Columbus (Nati et al., 1994), and the development of the Global Positioning System (GPS) constellation for high-low satellite tracking were significant milestones for the realisation of gravitational missions such as Challenging Mini-Satellite Payload (CHAMP)[1], Gravity Recovery and Climate Experiment (GRACE), GRACE Follow On (GRACE-FO)[2], and GOCE[3].

The accelerometer is a crucial component for these gravity missions. As mentioned, the deviations in orbital trajectory are due to the local gravity field and the non-gravitational forces acting on the satellite. The accelerometers can accurately measure the non-gravitational forces and separate their effects on the satellite's Center of Mass (COM) from the impact of gravitational variations, which are of interest. However, the accelerometers are not perfect. They are riddled with noise, biases, and scale factors (section 2.2); therefore, the data must be calibrated. But due to the high resolution and sensitivity of accelerometers to measure accelerations as small as $10^{-10}\,\mathrm{ms^{-2}Hz^{-1/2}}$ (Touboul et al., 2004) to measure the non-gravitational forces in LEO in all three axes, the electrostatic force for controlling the proof mass are not strong enough to lift the proof mass in a 1-g environment for testing (Touboul, Foulon, & Willemenot, 1999). Over the past two decades, several calibration techniques have been formulated ranging from using GPS observations (Helleputte et al., 2009; Visser & van den IJssel, 2016; Visser, 2007) to using global gravity fields, star tracker data (Rispens & Bouman, 2009), force modelling (Wöske et al., 2019) or even dedicating shaking manoeuvres (Frommknecht et al., 2011; Siemes et al., 2019).

The 2018 US Earth Science Decadal Report listed mass transport observations as one of the top priorities of Earth observation (National Academies of Sciences, Engineering, and Medicine, 2018). GRACE-FO is contributing to it by continuing the time series from GRACE. More studies are being carried out to determine a new concept named Next Generation Gravity Mission (NGGM) to be launched at the end of the current decade to improve the spatial and temporal resolution of gravity data. NGGM follows the footsteps of its predecessors and applies the lessons learnt from them through better performing accelerometers used on GOCE and Low-Low Satellite-to-Satellite Tracking (LL-SST) via laser tracking tested on GRACE-FO.

This thesis focuses on the critical aspect of the upcoming NGGM mission that is yet to be addressed: the data calibration of onboard accelerometers. It explores the different configurations of accelerometers and shaking manoeuvres that would suit the strict science requirements posed. By analysing the past calibration techniques and adapting them to the anticipated design of future gravity missions, this research aims to identify the effective strategies for minimizing the measurement errors and ultimately aid in high-quality gravity field observation.

The report is structured in the following way. Chapter 2 aims to understand the evolution of gravity missions and highlight the main takeaways. It describes the state-of-the-art by reviewing the electrostatic accelerometer concept and what each gravity mission offers. Based on satellite designs, the different calibration techniques developed are discussed. Chapter 3 then provides an overview of the recent studies published on NGGM to determine its preliminary design. Chapter 4 then establishes the research gap, the main research question, sub-questions and requirements on methodology to guide the thesis. In Chapter 5, the algorithms to generate the accelerometer data and tools to calibrate the accelerometer are outlined in detail. Chapter 6 presents the verification checks to ensure the correct implementation of the method laid out in Chapter 5. Chapter 7 presents the calibration performance results for different configurations and shaking manoeuvres and compares them against the scientific requirement posed on non-gravitational acceleration measurement. Finally, Chapter 8 concludes the findings by answering the research question and providing recommendations for future work.

---

[1] https://www.gfz-potsdam.de/en/section/geomagnetism/infrastructure/gfz-satellite-mission-champ

[2] https://grace.jpl.nasa.gov/

[3] https://www.esa.int/Enabling_Support/Operations/GOCE

2

A Review of Satellite Missions with Accelerometers

This chapter assesses the history of the gravity missions and the electrostatic accelerometers used onboard. Section 2.1 briefly motivates the need for an accelerometer on board the satellites, with its working principle explained in Section 2.2. Then, Section 2.3 outlines the previous flown gravity missions with their scientific contributions and primary instruments. Finally, Section 2.4 discusses the accelerometer data calibration techniques used on these missions.

2.1. Significance of Accelerometers for Space Missions

Numerous space applications require dedicated accelerometers with ranges and sensitivities optimized for the in-orbit environment. For microgravity experiments onboard the International Space Station, acceleration and vibration levels must be closely monitored for a controlled environment (McPherson et al., 2009).

In the field of physics experiments researching observation of gravity waves, measurements of very weak accelerations are required for the drag compensation systems on board Laser Interferometer Space Antenna (LISA) satellites to maintain a soft environment to detect the gravitational waves (Danzmann, 2000). The LISA mission will benefit from a very quiet environment, contrary to ground-based experiments like VIRGO or Laser Interferometer Gravitational-Wave Observatory (LIGO) limited by the low-frequency seismic noise (Josselin et al., 2001).

Furthermore, ultra-sensitive accelerometers have two main applications in the field of Earth observation. First, measuring surface forces acting on LEO satellites provides information about Earth's atmospheric density, high-altitude winds, and the radiation pressure from the Sun and Earth. Second, the accelerometers are crucial to the global and accurate recovery of the Earth's gravity field. The accelerometers are used to quantify the non-gravitational forces acting on the satellite and extract a gravity signal which is purely dictated by the Earth's mass distribution, both on the surface and the interior. The accelerometer is generally installed at the COM in order to be not affected by centrifugal and Euler accelerations (Touboul, Willemenot, et al., 1999; Touboul, Foulon, & Willemenot, 1999).

2.2. Working Principle of an Electrostatic Accelerometer

The measurement principle of an electrostatic accelerometer is based on the levitation of a proof mass (generally parallelepipedal shape) inside a cage surrounded by electrode pairs

(Figure 2.1a). The electrode pairs are used for capacitive position sensing and electrostatic restoring force generation. Figure 2.1b shows the diagram of a single axis for accelerometers used in gravity missions. The proof mass (grey square) is suspended between two electrodes (thin black rectangles) with a control voltage V. The proof mass is charged by a thin wire[1] with a polarisation DC voltage V_p and an AC detection voltage $V_d(t)$, thus giving proof mass a total voltage

$$V_t = V_p + V_d(t).$$

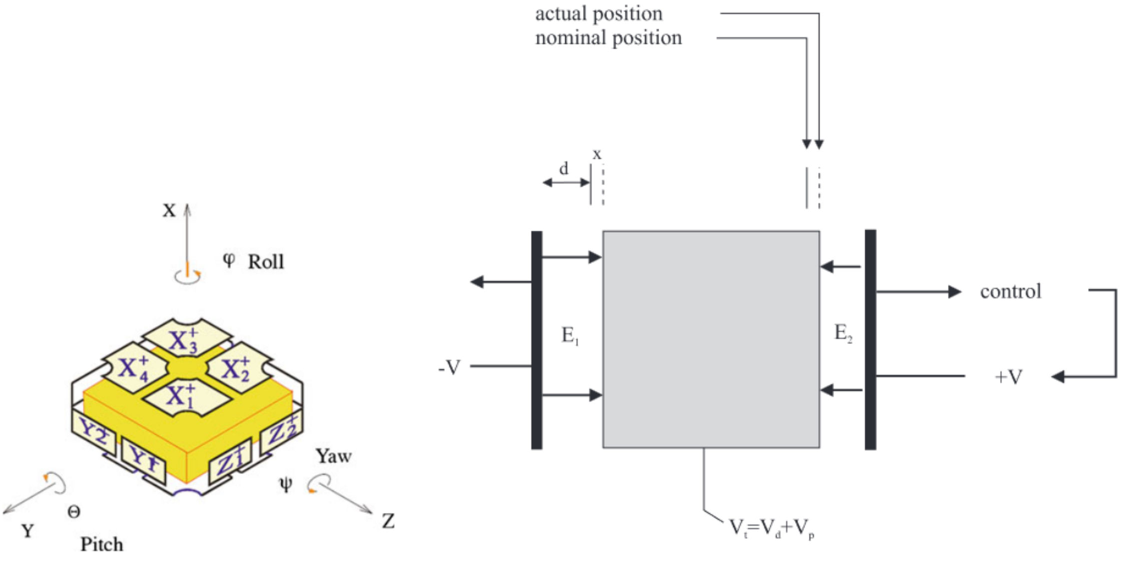

(a) **(b)**

Figure 2.1: a) An individual accelerometer electrode pairs and layout (Frommknecht et al., 2011). b) Concept of a capacitive accelerometer for one axis (Frommknecht et al., 2003).

Considering that V and V_t are positive, the system is inherently unstable as the proof mass will start moving towards the $-V$ electrode. Therefore, a servo control mechanism with a Proportional-Integrative-Derivative (PID) feedback loop is used to keep the proof mass motionless in the centre of the cage with a gap of d from the cage. The position of the proof mass is measured using a detection mechanism by comparing the capacitance values between the proof mass and the electrode (Frommknecht et al., 2003). The overall capacitive force is given by

$$F_{cap} = \frac{1}{2}\epsilon_0 A(E_1^2 - E_2^2), \tag{2.1}$$

where ϵ_0 is the dielectric constant, A is the area of the electrode, and E_i is the electric field between the proof mass and the electrode plates. Given the relation that $E = V/s$, V is the voltage difference between the proof mass and the electrode, and $s = d + x$ is the true distance. For first-order analysis, the distance x is considered small compared to d, and the AC detection voltage $V_d(t)$ does not affect the proof mass (Nati et al., 1994).

Thus, the capacitive force is

$$F_{cap} \approx \frac{1}{2}\epsilon_0 A\left(\frac{(V - V_p)^2}{d^2} - \frac{(V + V_p)^2}{d^2}\right), \tag{2.2}$$

(2.3)

---

[1] The wire is a feature of accelerometers made by ONERA.

which is equivalent to the acceleration

$$a = -2\frac{\epsilon_0 A}{md^2} V_p V. \tag{2.4}$$

The capacitive acceleration imparted is proportional to the electrode area A and inversely proportional to the square of the gap size d. The advantage of a smaller gap size is that the proof mass can be lifted under 1-g conditions for ground testing, but it greatly reduces the measurement precision because the noise in the control voltage has an amplified effect on the acceleration due to the increase in slope.

Figure 2.2 shows the main contributors to the accelerometer measurement noise. The detector circuit noise of the control loop (pink line) and the measurement noise (dark blue) due to the digitisation by the Analog-to-Digital Converter dominate the noise spectrum above and below $0.1\,\mathrm{Hz}$, respectively. At even lower frequencies, the electronic bias (light blue) creeps in due to thermal variations from the satellite undergoing eclipse phases in LEO. Therefore, electronics should preferably be housed in a thermally stable structure.

Furthermore, due to the imperfect alignment of accelerometer axes, scale factors $\boldsymbol{M}_i$, non-linearity due to quadratic dependency in the measurement $\boldsymbol{K}_i$, and projection of angular acceleration due to electrode layout $\boldsymbol{W}_i$ leads to a measurement model deviating from the perfect measurements represented by Equation 2.5, where $\boldsymbol{b}_i$ and $\boldsymbol{n}_i$ add a constant bias and frequency-dependent noise, respectively (Siemes et al., 2019; Touboul et al., 2016).

$$\boldsymbol{a}_i^{meas} = \boldsymbol{b}_i + \boldsymbol{M}_i \boldsymbol{a}_i + \boldsymbol{K}_i \boldsymbol{a}_i^2 + \boldsymbol{W}_i \dot{\boldsymbol{w}}_i + \boldsymbol{n}_i \tag{2.5}$$

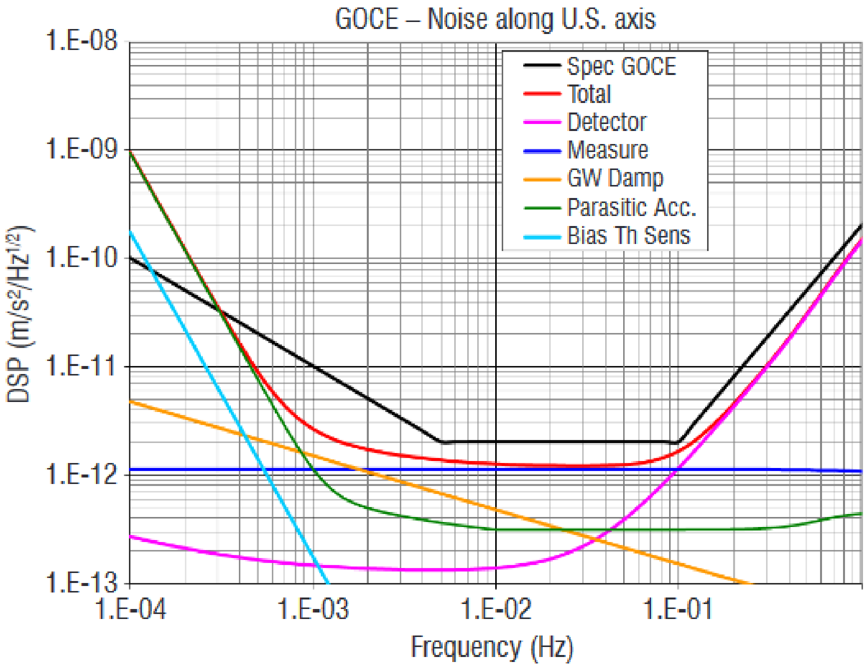

Figure 2.2: Noise performance of the GOCE accelerometer along their ultra-sensitive axis (Touboul et al., 2016).

When external forces act on the spacecraft, the servo control mechanism of the accelerometer nullifies the relative motion between the proof mass and the cage. The acceleration corresponding to the required force to bring the proof mass back to the centre of the cage is representative of the external acceleration and can be expressed as (Siemes et al., 2019)

$$\boldsymbol{a} = -(\boldsymbol{V} - \boldsymbol{\Omega}^2 - \dot{\boldsymbol{\Omega}})\boldsymbol{r} + \boldsymbol{a}_{ng}, \tag{2.6}$$

where $\boldsymbol{V}$ is the gravity gradient tensor, $\boldsymbol{\Omega}^2\boldsymbol{r}$ is the centrifugal acceleration, $\dot{\boldsymbol{\Omega}}\boldsymbol{r}$ is the Euler acceleration, $\boldsymbol{r}$ is the vector from the satellite's COM to the accelerometer cage's centre, and $\boldsymbol{a}_{ng}$ the non-gravitational accelerations acting on the satellite. $\boldsymbol{\Omega}$ and $\dot{\boldsymbol{\Omega}}$ are the angular rate and angular acceleration matrix, respectively. Note that the acceleration due to the satellite's self-induced gravity is ignored as it is considered negligible. Moreover, since the cage is rigidly mounted to the satellite, linear and Coriolis acceleration w.r.t. COM are thus zero (Bouman et al., 2004).

2.3. Past missions

Three pioneering dedicated gravity field missions were launched in the past two decades. Sections 2.3.1 to 2.3.3 will provide a brief overview of each mission, showcasing how the scientific objectives evolved and with it the performance demand of the accelerometers.

2.3.1. CHAMP

The German CHAMP satellite was designed to study the Earth's global gravitational and magnetic field. The primary goal was to improve the resolution of long wave components (~$1000\,\mathrm{km}$) of the gravitational field and a secondary objective of studying radio occultation of received GPS signals for remote sensing of atmosphere and ionosphere (Reigber et al., 1996). The accelerometer was placed at the COM to avoid centrifugal and Euler accelerations acting on the accelerometer. The electrostatic accelerometer STAR was manufactured by the French company ONERA, providing a resolution of $3 \times 10^{-9}\,\mathrm{ms}^{-2}$ (Touboul et al., 2012).

The satellite was launched into a circular orbit with an altitude of $454\,\mathrm{km}$ and an inclination of $87.3\,°$ (Flechtner et al., 2021). CHAMP was the first mission designed specifically to collect continuous gravimetry data with a polar orbit providing global coverage. The onboard GPS receiver and STAR accelerometer enabled continuous determination of kinematic satellite positions and extraction of pure gravitational signal for the first time, as the inaccurate and insufficient models of atmosphere and radiation pressure can be replaced directly with in-situ measurements. CHAMP data improved the accuracy of gravity models by a factor of around four compared to pre-CHAMP models (Reigber et al., 2002). This mission proved to be an essential stepping stone for the NASA/DLR mission GRACE.

2.3.2. GRACE and GRACE-FO

In 2002, GRACE was launched as a collaboration of National Aeronautics and Space Administration (NASA) and Deutsches Zentrum für Luft- und Raumfahrt (DLR). It was based on the concept of inter-satellite ranging between a pair of twin satellites in LEO (Wolff, 1969). The primary scientific objective of GRACE was to improve temporal variations in Earth's gravitational field down to a spatial scale of $300\,\mathrm{km}$ averaged over 30 days and a long-term time-average model down to a spatial scale of less than $200\,\mathrm{km}$. This corresponds to a spherical harmonic degree and order of 70 or higher for temporal variations and 150 or higher for the time-averaged (static) model (Kornfeld et al., 2019), a huge improvement in the medium-to-long wavelengths of gravity field compared to CHAMP (Tapley et al., 2004). It provided monthly estimates of the global gravity field to determine changes in Earth's mass distribution.

The mission consisted of a pair of satellites with a near-circular orbit at an initial orbital altitude of $500\,\mathrm{km}$ and an inclination of $89\,°$, separated by a distance of $220\,\mathrm{km}$ linked with a high precision dual-frequency K/Ka-band Microwave Instrument (MWI) (Kornfeld et al., 2019). Figure 2.3 shows the GRACE measurement concept. For example, when the leading satellite approaches a positive mass anomaly such as a mountain range, it gets accelerated more strongly by the gravitational force than the trailing satellite, thus increasing the distance to the trailing satellite. Once the leading satellite has passed the range, the mass anomaly will impart the same pull on it and decelerate it, while the trailing satellite will accelerate as it just approached the range. Finally, when both satellites move away from the range, the trailing satellite is decelerated more strongly than the leading satellite, which is further away. This generates a detectable signature in the distance between the two satellites measured by the MWI.

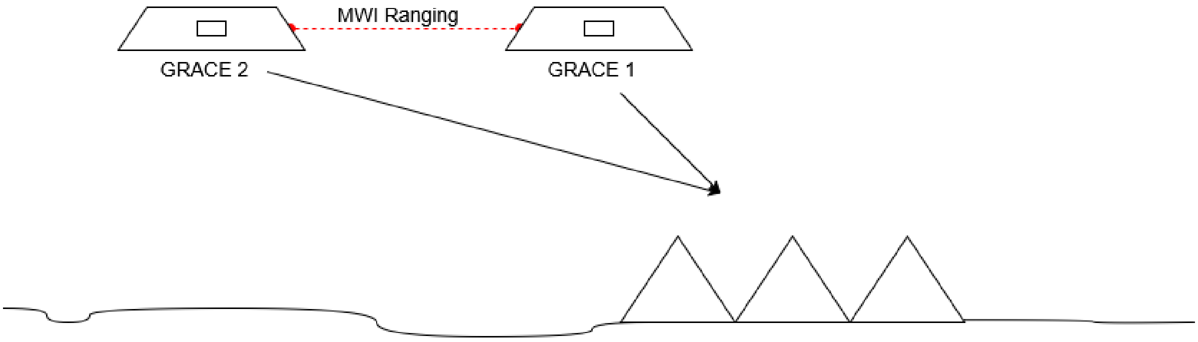

Figure 2.3: GRACE mission concept.

The range measurements are sensitive not only to the gravitational signal due to Earth's mass distribution but also to the non-gravitational accelerations. These were measured accurately again by a high-precision SuperSTAR accelerometer supplied by ONERA (Touboul, Willemenot, et al., 1999) mounted at the COM of each satellite to minimize the coupling of rotational accelerations on linear accelerations. The SuperSTAR accelerometer is based on the design of the STAR accelerometer flown on CHAMP with additional improvements to accommodate a resolution of $10^{-10}\,\mathrm{ms^{-2}Hz^{-1/2}}$ demanded by GRACE (Kornfeld et al., 2019).

GRACE was a revolutionary mission, with its 15+ years of data being instrumental in studying climate change and the overuse of water resources. It significantly contributed to monitoring groundwater levels, river basins worldwide, and glacial mass loss in Greenland, Antarctica and mountain ranges, which led to sea level rise (Tapley et al., 2019).

GRACE-FO was as a continuation of GRACE, having similar scientific objectives. Its objective is to provide continuity in gravity field observations and the collection of long-term data on the effects of climate change. The orbit design is similar to that of GRACE with a near-circular polar orbit of an altitude of $500\,\mathrm{km}$. GRACE-FO structurally has same outer dimensions as GRACE. A new addition to the payload was a new Laser Ranging Interferometer (LRI) as a technology demonstration for future gravity missions. It measures the inter-satellite distance like the MWI but with a much higher sensitivity and lower noise.

The range change measurements should be processed at the COM position; however, the COM is already occupied by the accelerometer. Therefore, an off-axis symmetric configuration using a Triple Mirror Assembly (TMA) is employed to correctly route the incoming and outgoing laser beams. The accelerometer is similar to the one on GRACE but with minor improvements.

However, GRACE and GRACE-FO have only one accelerometer, which is a single point of failure. In fact, the accelerometer on GRACE-FO-2 underperformed and degraded the quality of measurements, which forced to model non-gravitational forces acting on GRACE-FO-2 using accelerometer data of GRACE-FO-1 (Landerer et al., 2020).

2.3.3. GOCE

GOCE was the first Earth Explorer Mission of European Space Agency (ESA) launched in 2009 (Drinkwater et al., 2003). It employed a different technique to study gravity by measuring the gradients of the gravitational vector, the second derivative of the gravitational potential (Rummel & Colombo, 1985).

GOCE accomplishes this with a three-axis Electrostatic Gravity Gradiometer (EGG). It consists of six ultra-sensitive accelerometers developed by ONERA mounted on a stable carbon-carbon structure in a diamond configuration, with two accelerometers aligned on each axis with a noise level at $10^{-12}\,\mathrm{m/s^2/Hz^{-1/2}}$ (Drinkwater et al., 2003; Floberghagen et al., 2011; Touboul, Willemenot, et al., 1999; Willemenot et al., 1999).

The scientific objective of GOCE was to model the static gravity field and geoid with a high spatial resolution and accuracy. It was designed to resolve spatial features up to $100\,\mathrm{km}$ with an accuracy of 1 mGaL (=$10^{-5}\,\mathrm{m\,s^{-2}}$) corresponding to medium to short wavelengths (Drinkwater et al., 2003).

GOCE uses a combination of two systems to achieve its high performance. With a GPS receiver on board, its orbital trajectory can be measured with centimetre accuracy and be used to derive the lower order harmonics of the gravitational field (H. Bock et al., 2011), while the increased details of the gravitational field were then measured by the EGG in a Measurement Bandwidth (MBW) of 5-100 mHz (Drinkwater et al., 2003; Flechtner et al., 2021).

The satellite was launched into a sun-synchronous polar orbit with an altitude of around $280\,\mathrm{km}$ and an inclination of $96.7°$. The Drag-Free and Attitude Control System (DFACS) provided a quiet environment to the EGG by compensating the non-gravitational forces acting on the spacecraft as it descended to a lower altitude to reduce the effects of EGG imperfections on the acceleration and to sustain the mission duration of 3 years at such a low altitude. Although the along-track axis of DFACS consisted of ion thrusters, only cold-gas thrusters were available for controlling the attitude in the two remaining axes, which lacked thrust amplitude modulation (Floberghagen et al., 2011).

2.4. Calibration of Accelerometers

In section 2.2, we saw that the measured acceleration is riddled with error terms which need to be corrected before it can be used to derive gravity field solutions. As an example to show the importance of calibration, the performance of calibrated and uncalibrated accelerometer data, the GOCE case is presented. The gravitational field is conservative, such that the acceleration due to gravity can be represented as

$$\boldsymbol{g} = \nabla V \tag{2.7}$$

Assuming that the mass distribution is stationary at a given moment, and the effects of other sources such as the Sun, Moon, atmosphere, and oceans are corrected for, the acceleration may be regarded as source-free, giving rise to the Laplace condition (Rummel et al., 2011):

$$\nabla \cdot \boldsymbol{g} = V_{xx} + V_{yy} + V_{zz} = 0, \tag{2.8}$$

also called the trace of the gravity gradient tensor $\boldsymbol{V}$.

This condition formed the basis for assessing the performance of the gradiometer. In Figure 2.4a, the ASD of the uncalibrated data (black curve) is $100\,\mathrm{mE}\sqrt{\mathrm{Hz}}$ ($1\,\mathrm{mE}$ = $10^{-12}\ \mathrm{s}^{-2}$) at $0.1\,\mathrm{Hz}$ and increases strongly toward lower frequencies. In contrast, the trace of the calibrated data shown in Figure 2.4b is $20\,\mathrm{mE}\sqrt{\mathrm{Hz}}$ in the frequency range from $0.01\,\mathrm{Hz}$ to $0.1\,\mathrm{Hz}$, showcasing an improvement over the uncalibrated data by order of magnitude.

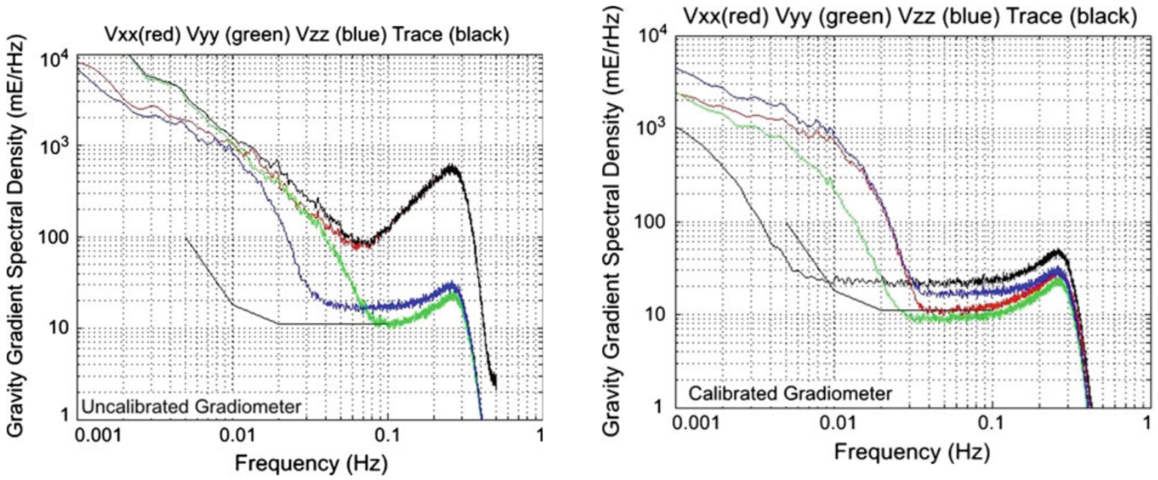

(a)

(b)

Figure 2.4: Trace (black) and individual diagonal gravity gradient V_{xx}, V_{yy}, and V_{zz} (red, green and blue) performance for the gradiometer (Frommknecht et al., 2011). a) Uncalibrated gradiometer. b) Calibrated gradiometer

Equation 2.6 depicts that the represented quantity differs depending on the position of the accelerometer in the satellite. In the case of CHAMP, GRACE, and GRACE-FO, the accelerometers were placed at the COM, resulting in $\boldsymbol{r}$ being zero and thus measuring only the non-gravitational accelerations. Also, GRACE missions had mass trim mechanisms to correct the offset of the accelerometer from the COM. Whereas for GOCE, due to the EGG structure, the individual measurements included gravity gradients and Euler and centrifugal accelerations.

Several data calibration techniques have been developed from these missions:

1. Calibration using GPS-based orbit determination: All the previous missions carried a GPS receiver on board for precise time tagging and orbit determination. The satellite's orbit can be estimated with high precision using a dynamical model whose parameters are iteratively adjusted by correcting their a priori values with GPS observations in the least squares solution (Montenbruck et al., 2005). In this calibration method, the non-gravitational force models used in the dynamical model are replaced directly by the calibrated accelerometer measurements

$$\boldsymbol{a}_{cal} = \boldsymbol{S}\boldsymbol{a}_{meas} + \boldsymbol{b} \tag{2.9}$$

   where $\boldsymbol{S}$ is a diagonal scale factor matrix. The scale and bias factors are then estimated in the least-squares adjustment procedure (Helleputte et al., 2009; Visser, 2007). This method showed a high correlation between the scale factors and bias due to low sensitivity in the acceleration signal. Scale factors from other calibration techniques (Bouman et al., 2011) were used. However, estimation of scale factors was possible during occasional orbit manoeuvres, generating a strong enough acceleration signal (Visser & van den IJssel, 2016).

2. Calibration using gravity field models and star sensor data: External global gravity field models and/or terrestrial gravity field data in conjunction with the star sensor data are used to correct the errors in gravity gradients and angular rates measured by the gradiometer to the ones from the model at low frequencies (Rispens & Bouman, 2009; Visser, 2008).

3. Calibration using Poynting energy flux observations: Calibration where the GOCE EGG disturbances were related to ionosphere dynamics using Poynting energy flux, which indicates the flow of electromagnetic energy driving the ionosphere winds. However, it is an indirect method and the observations were limited to North America (Ince & Pagiatakis, 2017).
4. Calibration via force modelling: This method involves modelling the non-gravitational forces acting on the satellite and comparing the simulated accelerometer data with the observations (Wöske et al., 2019). However, the downside of this method is that it requires very accurate knowledge of the spacecraft structure, material and aerodynamic properties. Furthermore, the non-gravitational models are notoriously inaccurate due to the uncertainty in solar activity prediction, the atmosphere's fast dynamics, and/or reliance on empirical data. Table 4 in ref. (Bruinsma et al., 2018) shows the density ratios of modern thermosphere models. All the models have a 10-20% difference in atmospheric density compared to in-situ observations. Also, the availability of accurate thermosphere models removes the need for accelerometers. Moreover, the method fixes the scale factors as it is not sensitive enough to estimate bias and scale factors together.
5. Calibration using shaking manoeuvres: This was an internal calibration method as it solely used the data measured by sensors on board GOCE. It generated significant pseudo-random linear and angular acceleration signals at high frequencies in the MBW. The benefit of this method was large, distinguishable non-gravitational signals, and the gravity gradient signal considered below the instrument's noise level made it easier to model the parameters in the calibration model (Frommknecht et al., 2011).

Regardless of the method, the GOCE gravity solutions suffered from significant perturbations in the scale factors, especially in the cross-track direction at geomagnetic poles (Bouman et al., 2011). Most methods used an accelerometer model with the quadratic factor $\boldsymbol{K}_i$ in Equation 2.5 neglected. This was possible as a correction was implemented at the accelerometer level by offsetting the proof mass such that the value of the 2nd-order term was below a given threshold (Frommknecht et al., 2011). Although the majority of the effect was removed, Siemes (2018) concluded that extending the model to include the quadratic factor removes the persistent perturbation to a large extent.

3

Next Generation Gravity Mission

From Chapter 2, there is a clear trend on how the scientific requirements evolved and became more demanding for each mission. This was further realisable due to an upgrade in available technology, especially the accelerometers and implementation of different concepts.

This chapter provides an overview of the proposed NGGM mission. Section 3.1 provides an overview on what new contributions NGGM provides compared to previous missions. In Section 3.2 follows the measurement principle NGGM relies upon. Lastly, Section 3.3 describes the preliminary design of NGGM and the main instruments on board.

3.1. Scientific Objective of NGGM

Although GOCE supplied a global static map of gravity with unprecedented details, it lacked in providing monthly snapshots like GRACE. NGGM therefore aims to measure the temporal variations of the gravity field over a long period to provide continuity in data sets as a part of the Mass change And Geosciences International Constellation (MAGIC), a joint venture between NASA and ESA. ESA will therefore supply NGGM, one of the two pairs of the constellation, with the scientific objective of measurement of the geoid with an accuracy of 1 mm at a spatial resolution of 500 km every 3 days and 150 km every 10 days for at least 7 years (Dionisio et al., 2018; ESA et al., 2023; Massotti et al., 2021).

GRACE and GRACE-FO monthly gravity solutions are limited due to five main error sources, namely the accelerometer measurement errors, inter-satellite range measurement errors, precise orbit determination errors, aliasing due to spatial and temporal under-sampling, and errors in background models used for de-aliasing. Furthermore, the gravity field solutions were more sensitive in the North-South direction due to the polar orbit of the formations (Flechtner et al., 2016)

The inter-satellite measurement errors can be improved for future missions by including Laser Tracking Instrument (LTI) and the accelerometer errors through better hardware and data calibration methods. Additionally, a lower inclination of the satellite pair is proposed to gain more sensitivity in the East-West direction. Elsaka et al. (2014) compares different orbit configurations and concludes that if the budget allows, a Bender configuration (see Figure 3.1) would provide the best gravity field solution. The Bender configuration consists of two satellite pairs, one in a polar orbit and another at a lower inclination of around 65° (Dionisio et al., 2018). A bender constellation thus improves the East-West sensitivity, and an additional pair also adds more space-time sampling points to better track the fast variations. Each pair was anticipated to fly in an in-line formation around $100\,\mathrm{km}$ apart at an altitude of around $360\,\mathrm{km}$

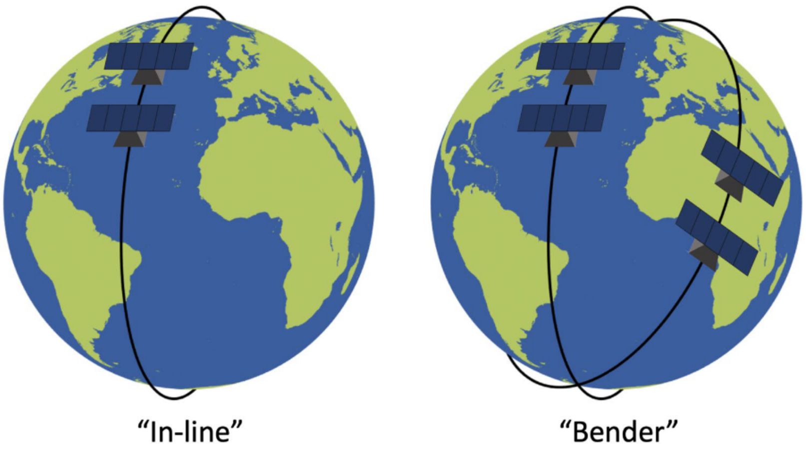

Figure 3.1: In-line formation (left) and Bender constellation (right) (Haagmans et al., 2020).

3.2. NGGM Measurement Principle

NGGM relies on the same measurement principle of ranging as of GRACE. Instead of a MWI, it uses a LTI system with much lower noise. The LL-SST exploits the satellites as ”proof masses” immersed in Earth’s gravity field. The fundamental observable is

$$\Delta d = \Delta d_G + \Delta d_D, \ \Delta \ddot{d}_D = \Delta a_{ng} = a_{ng1} - a_{ng2} \tag{3.1}$$

where Δd is the distance variation between the two satellite’s COM produced as shown in Figure 3.2. This range change observed by LTI is a sum of distance variation Δd_G due to gravitational accelerations g and distance variation Δd_D due to non-gravitational forces $\boldsymbol{a}_{ng}$ acting on the satellites’ COM (represented by *D* in the figure) (Cesare & Sechi, 2013).

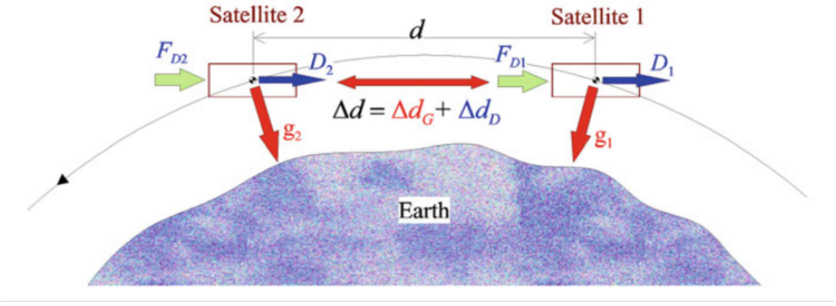

Figure 3.2: Principle of LL-SST technique for measuring Earth’s gravity field (Cesare & Sechi, 2013).

The relative distance change imparted by the non-gravitational forces along the line joining the COMs is observed by integrating the forces a_{ng1} and a_{ng2} measured by the electrostatic accelerometers on board satellites.

3.3. NGGM Spacecraft Design

Figure 3.3 shows the preliminary design of the satellite. It is similar in design to the GRACE satellite, with solar panels mounted on the main structure. Thus, the GRACE satellites will form the reference for the dimensions for the rest of the report. The upper limit of each satellite conforming to launcher requirements has been set to $1000\,\mathrm{kg}$ (Dionisio et al., 2018).

This section provides an overview of the main components on board NGGM satellites. These include the LTI (Section 3.3.1), the accelerometer (Section 3.3.2), the propulsion system (Section 3.3.3) and the attitude sensors (Section 3.3.4). For each, if relevant, an explanation for its selection is provided, along with its performance, requirements, and position in the satellite.

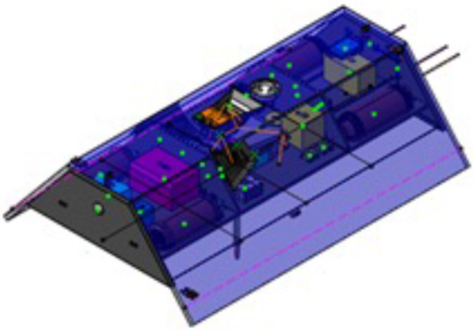

Figure 3.3: NGGM satellite envisioned structure (Massotti et al., 2022).

3.3.1. Laser Tracking Instrument (LTI)

Two concepts of laser tracking instruments were investigated (Nicklaus et al., 2019):

- Transponder scheme: Similar to the one used on GRACE-FO (Kornfeld et al., 2019). The laser beam from satellite 1 is amplified on satellite 2 and retransmitted to the first satellite.
- Retroreflector scheme: The laser beam transmitted from satellite 1 is passively reflected by satellite 2.

The inter-satellite distance measured by the LTI is between the COMs of the satellites. Only an off-axis configuration (also known as racetrack configuration) is considered as it was deemed superior over the on-axis due to less criticality w.r.t. to polarisation, straylight, complexity due to optical elements in the beam path and complexity of the operation.

Moreover, out of the two concepts, the transponder scheme is deemed to be a feasible concept for NGGM as only this scheme could cover the required separation from $100\,\mathrm{km}$ to $300\,\mathrm{km}$. The retroreflector was also feasible for $100\,\mathrm{km}$ with increased laser power, but it would demand too much power for higher distances. Also, the transponder scheme has heritage from GRACE-FO, thus bringing in knowledge and technology already available (Nicklaus et al., 2019; Nicklaus et al., 2022).

The laser beam from the distant spacecraft is superimposed with the local oscillator beam. A beam-splitter redirects a part of the light to a Differential Wavefront Sensor (DWS), which measures the misalignment between the incoming and locally generated beam. This data is then used to actuate the Fast Steering Mirror (FSM) to align the beams.

The goal performance requirement of the ASD of the inter-satellite relative distance variation is considered for LTI (Massotti et al., 2021), which is given in an analytical form as (Encarnação et al., 2024)

$$A(f)_{NGGM,\rho} = L_{ISR}10^{-13}\sqrt{1+\left(\frac{0.01}{f}\right)^2}\sqrt{1+\left(\frac{0.001}{f}\right)^2}\left[\frac{\mathrm{m}}{\sqrt{\mathrm{Hz}}}\right], \tag{3.2}$$

where L_{ISR} is the inter-satellite range and f is the frequency.

3.3.2. Accelerometer

It is stipulated that the non-gravitational accelerations experienced by NGGM shall be measured at least at the level of GOCE (ESA et al., 2023). As done with the previous missions, ONERA will supply a new generation of MicroSTAR-class electrostatic accelerometers. It will have identical performance on all three axes with a heavier cubic proof mass with six identical electrode plates (Figure 3.4a) in contrast to GOCE and GRACE, which only had two ultra-sensitive axes. The gap between the proof mass and the electrodes is increased compared to previous missions to attain higher precision with a measurement range of $\pm 6.4 \times 10^{-6}\,\mathrm{m\,s^{-2}}$ (Christophe et al., 2018). The MicroSTAR accelerometer onboard the GRACE-FO satellites have a weight of $1.5\,\mathrm{kg}$ with a size of $90\,\mathrm{mm} \times 90\,\mathrm{mm} \times 70\,\mathrm{mm}$ with a power consumption of $2\,\mathrm{W}$ (Christophe et al., 2015). The new prototype tested for NGGM has a smaller cubic proof mass (Christophe et al., 2018), but the size of the whole instrument is not reported. Thus, the old size will be used in this report.

Figure 3.4b presents an overview of the ASD of the performance of the MicroSTAR accelerometer compared to the goal of the NGGM mission for relative non-gravitational acceleration measurement error projected along the Line of Sight (LoS) of the satellites. The accelerometer can resolve a maximum of $0.5\,\mathrm{Hz}$ according to the Nyquist-Shannon sampling theorem, as the data readout available to the user is assumed to have a sampling frequency f_s of $1\,\mathrm{Hz}$.

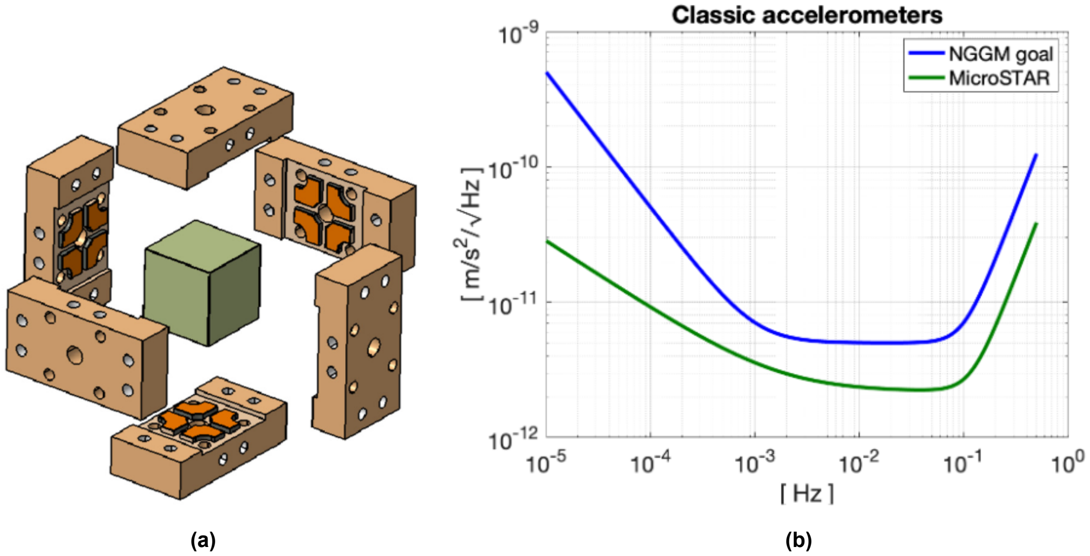

(a) (b)

Figure 3.4: a) The core of MicroSTAR with the cubic PM is surrounded by six identical electrode plates (Cesare et al., 2022). b) Overview of the noise ASD of MicroSTAR (Encarnação et al., 2024).

The goal scenario (Massotti et al., 2021) and the noise performance (Christophe et al., 2018) of the accelerometer are written in the analytical form as (Encarnação et al., 2024)

$$A(f)_{\text{NGGM,ng}} = 5 \times 10^{-12}\sqrt{1 + (0.001/f)^2 + (100f^2)^2}\left[\frac{\mathrm{m\,s^{-2}}}{\sqrt{\mathrm{Hz}}}\right], \tag{3.3}$$

$$A(f)_{\text{MircroSTAR,ng}} = 2 \times 10^{-12}\sqrt{1.2 + 0.002f^{-1} + 6000f^4}\left[\frac{\mathrm{m\,s^{-2}}}{\sqrt{\mathrm{Hz}}}\right]. \tag{3.4}$$

This requirement is defined for the satellite's science mode operation, where it is drag compensated in the along-track direction.

As discussed earlier in Section 2.3.2, the accelerometer was a single point of failure for GRACE-FO. The degradation of the accelerometer on the second satellite affected the mission's performance. Therefore, at least two accelerometers are considered for NGGM for redundancy. The possible configurations are (see Figure 3.5):

- Two accelerometers symmetrically placed around the COM on any of the three axes (Haagmans et al., 2020; Massotti et al., 2020).
- Three accelerometers, one at the COM and two symmetrically placed around the COM on any of the three axes.
- Four accelerometers, with two forming a pair placed symmetrically around the COM. A total of three orientations are possible.

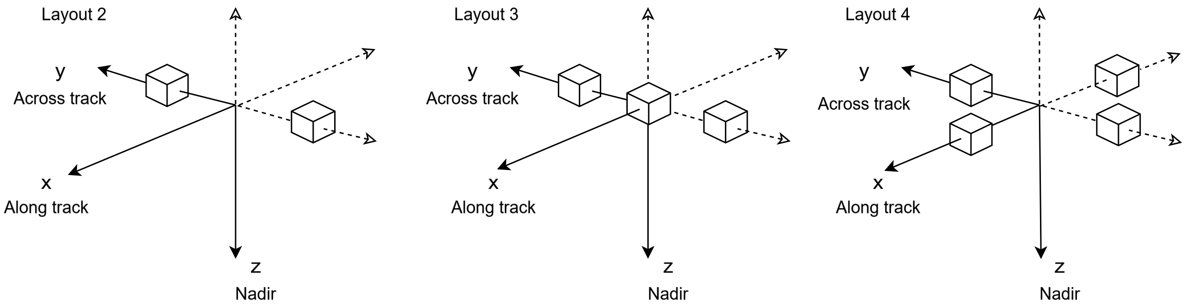

Figure 3.5: Possible accelerometer configurations. The accelerometers in each layout are free to be placed on any axis. For Layout 4, the placement can be in planes parallel to the xy, yz, or xz planes.

All configurations can have a varying inter-accelerometer arm length for the pairs. GOCE shaking calibration method is considered since the off-centre placement of the accelerometers gives sensitivity to angular accelerations. Furthermore, it relies only on the data produced by sensors on board the spacecraft. Gravity models will be used for calibration as the primary purpose of NGGM is to measure gravity using LL-SST, unlike GOCE, which measured the gravity via a EGG.

Combining the ASD requirements of the LTI and the accelerometer, one can derive the ASD requirement of the complete system in acceleration units by using Equations (3.2) and (3.3) (Massotti et al., 2021) as

$$A(f)_{NGGM,sys} = \sqrt{[A(f)_{NGGM,\rho}(2\pi f)^2]^2 + A(f)_{NGGM,ng}}. \tag{3.5}$$

Choosing an inter-satellite distance of $220\,\mathrm{km}$ (Cesare et al., 2022), the combined requirement (red line) is shown in Figure 3.6. Below $1\,\mathrm{mHz}$, the combined requirement is dictated by the accelerometer (dashed black line) and above by the LTI system (dotted blue line).

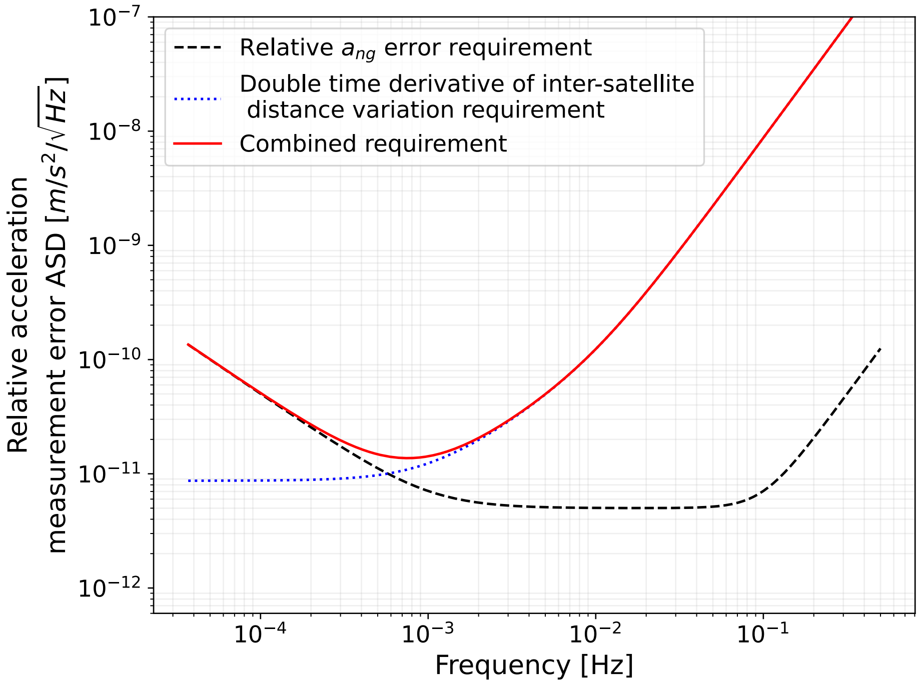

Figure 3.6: Combined requirement on relative non-gravitational measurement error

3.3.3. Propulsion

Each spacecraft is anticipated to be equipped with two identical types of ion thrusters, Drag Control Thruster (DCT) and Fine Control Thruster (FCT) (Massotti et al., 2020, 2021). Two 15 mN-class DCT thrusters in cold redundancy provide the along-track force for drag compensation, formation control, and orbit maintenance. Two operating regimes are specified for it:

A cluster of the mN-class FCT micro thrusters compensates the cross-track and radial drag forces and provides attitude and pointing control. The operating range requirement of the FCT is between $1\,\mu\mathrm{N}$ and $2\,\mathrm{mN}$. With a satellite mass of $1000\,\mathrm{kg}$, the maximum acceleration requirement of the FCT thruster is $2 \times 10^{-6}\,\mathrm{m\,s^{-2}}$. Moreover, it is stipulated that the propellant mass for DCT+FCT shall not exceed $100\,\mathrm{kg}$.

The noise requirement of the thruster is defined as (Massotti et al., 2021)

$$A(f)_{thruster} = \begin{cases} \leq 100\,\mu\mathrm{N}/\sqrt{\mathrm{Hz}}, & \text{if } f < 0.3\,\mathrm{mHz} \\ \text{Linear} & \text{if } 0.3\,\mathrm{mHz} < f \leq 0.03\,\mathrm{Hz} \\ \leq 1\,\mu\mathrm{N}/\sqrt{\mathrm{Hz}} & \text{if } f > 0.03\,\mathrm{Hz} \end{cases} \tag{3.6}$$

However, due to budget constraints, a full three axes DFACS system may not be utilized but is drag-free only on the along-track axis with proportional cold gas thrusters on the cross-track and radial directions (Massotti et al., 2022). This study will assume the cold gas thrusters have a similar thrust noise requirement and use it as the actual noise as a conservative estimate.

3.3.4. Attitude Determination Sensors

A star tracker camera is one of the satellite's most important attitude-determination sensors. It is essentially a digital camera with a focal plane laid out by Charged-Coupled Device (CCD) or Complementary Metal-Oxide Semiconductor (CMOS) at a distance *f* (focal length) behind the vertex, the origin of the optical system. A *x, y* and *z* right-hand coordinate system with the vertex is depicted in Figure 3.7. The z-axis is also known as the tracker's boresight (Markley & Crassidis, 2014).

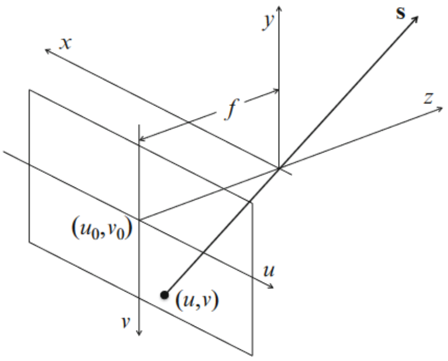

Figure 3.7: Star tracker geometry (Markley & Crassidis, 2014).

The NGGM satellites are expected to have four star-tracker camera heads. Generally, the primary three-star trackers' boresights are arranged perpendicular to each other to ensure complete occultation of the sky by the Earth, Sun, and Moon for more than one star tracker is avoided. The fourth is added for redundancy purposes. Like GOCE, at least two-star trackers will be active at any given time (Massotti et al., 2020). Thus, the study will assume uninterrupted attitude observations available during the calibration.

It is assumed that NGGM would be equipped with a state-of-the-art Micro Advanced Stellar Compass (μASC) star tracker sensor developed by Danmarks Tekniske Universitet (DTU), which has already flown on GRACE and the Swarm mission (Herceg et al., 2017). The noise ASD of the (μASC) star sensor for attitude is characterized as (Goswami et al., 2021)

$$A(f)_{\mu\mathrm{ASC},\theta} = 8.5 \times 10^{-6}\sqrt{f^{-1}}\left[\frac{\mathrm{rad}}{\sqrt{\mathrm{Hz}}}\right]. \tag{3.7}$$

In addition to the star trackers, there would be six coarse Earth and Sun sensors (Haagmans et al., 2020). However, they are not relevant for calibration studies as they are not as accurate as the star trackers and are generally used during the detumbling phase to stabilise the satellite after launch vehicle separation. The DWS is not considered for calibration as the laser link during the shaking manoeuvre is expected to be broken.

Finally, the accelerometer can also provide attitude information by measuring the angular accelerations as it contains multiple electrodes on each face of the cage. The noise ASD of the MicroSTAR accelerometer for angular acceleration is characterized (Christophe et al., 2018) and written in analytical form (Encarnação et al., 2024) as

$$A(f)_{\text{MircroSTAR},\dot{\omega}} = 1 \times 10^{-10}\sqrt{0.4 + 0.001f^{-1} + 2500f^{4}}\left[\frac{\mathrm{rad\,s^{-2}}}{\sqrt{\mathrm{Hz}}}\right]. \tag{3.8}$$

4

Research Proposal

Section 4.1 aims to consolidate the research gap and formulate the research questions to guide the research activities. Section 4.2 then provides an initial outline to guide the methodology development with requirements to limit the scope of the thesis. Finally, refer to Appendix C for thesis planning.

4.1. Research Questions

The satellite pairs will carry at least two accelerometers on board based on recent research on NGGM mentioned in chapter 3. However, recent studies have focused mainly on the LTI (Nicklaus et al., 2019) and optimizing the orbit design (Massotti et al., 2021). For the accelerometer, only mentions of its structure and achievable noise performance are present. As highlighted in Section 2.4, a large performance difference exists between calibrated and uncalibrated accelerometers. There is a lack of detailed analysis of optimal configurations and performance. Further, ground testing is no longer possible as lifting the proof mass under 1g of acceleration is impossible due to the increased sensitivity on all three axes by increasing the gap between the electrodes and proof mass. Based on the findings in section 2.4, the focus shall be on calibration, especially with shaking manoeuvres due to a partial GOCE-like setup, an extensive accelerometer model and the success of its calibration method which relied solely on the data from the sensors on board the spacecraft. However, the calibration method used a single type of shaking manoeuvre at a high-frequency range of 50 to $100\,\mathrm{mHz}$ with six accelerometers on board.

Considering the above, this thesis aims to support calibrating the accelerometer data for NGGM incorporating the lessons learnt from the previous gravity missions. An analysis of different accelerometer configurations and shaking manoeuvres can help provide a foundational insight into the number of accelerometers required, their favourable placement and the shaking signal, given the noise characteristics of the current state-of-the-art sensors. The research objective is then defined as follows:

To what extent can the shaking manoeuvres help calibrate the accelerometers by incorporating accurately the noise and error characteristics of the accelerometers and star trackers?

A list of sub-questions based on the main research question follows to further structure and aid this work:

1. What is a favourable configuration of accelerometer placement to retrieve non-gravitational acceleration along the laser's LoS?

    (a) What is the error in the non-gravitational acceleration along the laser's LoS?
2. What shaking manoeuvre is optimal for data calibration?
    (a) What is the error in non-gravitational acceleration along the laser's LoS?
3. What is the effect of the shaking manoeuvre on mission performance?
    (a) How long does the shaking have to last?
    (b) How much of the resources would be used?

4.2. Model development

This study will explore the possibilities of having multiple accelerometers placed on different axes and different shaking manoeuvres that can be employed for calibrating the accelerometer data for NGGM. Therefore, a flexible and comprehensive methodology is required to answer the research questions. The methodology development will be split into two main components:

1. Calibration tool: This tool calibrates the accelerometer data based on the input data it receives. It should be able to handle different numbers of accelerometers at different axis placements. The model should output the estimated and true parameters (only possible in a simulation environment) resulting from calibration. This tool operates on any input data as long as it is provided in its desired format. It is independent of the data supplied to it.
2. Data generation tool: This tool shall handle all the tasks related to data generation that will be supplied as input to the Calibration tool. The tool shall be able to create a user-defined orbit with flexibility to incorporate different physical models. The data generation tool will be built around TudatPy (Dirkx et al., 2023) as it is ideal for this purpose. The tool shall also be able to generate a user-defined shaking manoeuvre signal about all axes of the body-fixed frame by defining its characteristics in the frequency domain.

The following set of requirements and constraints is derived to aid the tools' development and limit the scope of the study:

1. The satellite shall have at least two and at most four accelerometers on board. One accelerometer is a single point of failure, and more than four accelerometers are too expensive from the perspective of cost and accommodation.
2. The calibration method shall optimally use the star sensors and accelerometer data for attitude determination. Since the attitude information is available from two sensors, the attitude information can be combined to limit the effect of noise on the observations.
3. The MicroSTAR accelerometer developed by ONERA is used as a reference for the noise characteristics of the accelerometer. It is the state-of-the-art accelerometer available on the market, and it has improvements based on the lessons and heritage of previous gravity missions.
4. The satellite shall have modulation-capable cold-gas thrusters. This allows for generating a desired shaking signal in the frequency domain and does not limit it to a single frequency.
5. Laser link tracking is not considered in the calibration model. It is assumed that the attitude control system can achieve it after calibration.
6. The satellite is already detumbled and pointing along the LoS before the shaking manoeuvre is performed, allowing us to focus our efforts on the calibration.
7. The shaking manoeuvre can be applied for a variable duration.
8. It is assumed that the satellite's attitude control system will remove any bias accumulated in angular rates during shaking to keep the attitude under control.

9. The NGGM satellite pair will fly at an inclination of $65°$.
10. The satellite pair will fly in a circular orbit.
11. The satellite pair will fly at an altitude of $396\,\mathrm{km}$.
12. An inter-satellite distance of $220\,\mathrm{km}$ is maintained between the pair.
13. The satellite is drag-compensated in its body-fixed x-direction during calibration to reduce the effect of accelerometer hardware imperfections along the LoS, which predominantly lies in the body-fixed x-direction (along track).

Requirements 9-12 stem from the optimal orbital parameters of the inclined pair in the Bender configuration. The calibration tool works as a post-processing tool accepting accelerometer measurements; therefore, the data generation tool is also set up such that the data outputted resembles accelerometer data that a user will receive. No control system with closed loop feedback is implemented for the shaking manoeuvre with the assumption that the thrusters can achieve the user-defined signal, as the aim is to study calibration, not the satellite's attitude control.

5

Methodology

This chapter describes the toolbox implemented for this thesis. Figure 5.1 provides an overview of the toolbox. The first part of the toolbox is for ”Data generation”, described in Section 5.1. It involves two steps

1. Reference orbit generation (blue box): This part generates a reference NGGM orbit, which outputs the gravity gradients based on satellite position w.r.t. the Earth, quaternions for attitude and non-gravitational acceleration to generate a true acceleration signal Section 5.1.1.
2. Accelerometer imperfections (green box): The accelerometer model is presented here, where hardware imperfections are introduced to generate a realistic accelerometer signal (Section 5.1.2).

The output of the blue and green boxes is combined to generate a measured signal representative of an acceleration signal with noise sensed by an accelerometer on board a satellite.

The second part of the toolbox is dedicated to accelerometer data calibration by performing the least squares operation described by Section 5.2. The least squares problem is initialised by an initial guess of the parameters to be estimated, through which observations and the design matrix are initialised. The least squares problem is solved iteratively until the error between the measured and reconstructed observations reaches the noise level in the accelerometer.

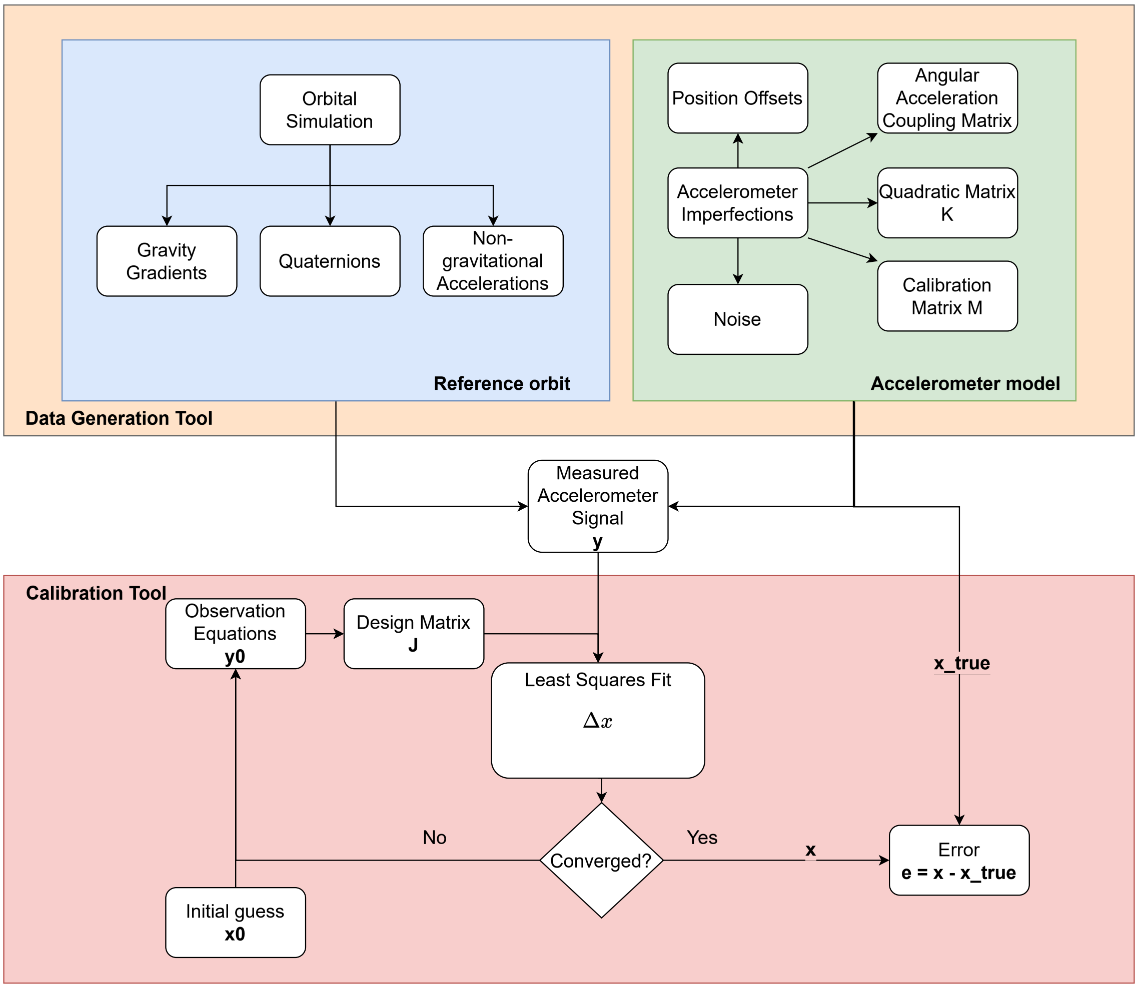

Figure 5.1: Overview of the two main tools implemented.

5.1. Data Generation

This section explains the steps to generate a realistic signal outputted by an accelerometer on board a satellite. Section 5.1.1 explains how a reference NGGM orbit is created with Section 5.1.2 defining the accelerometer model. Data from these two sections is combined to generate a (simulated) measured acceleration signal typically resembling data available to end users in a real mission.

5.1.1. Reference Orbit

The NGGM pair orbit is simulated using TudatPy to generate an accelerometer signal. The following assumptions are made for the orbit setup:

1. Only the trailing satellite is considered for calibration. The shaking manoeuvre is specific to a satellite and independent of the other satellite in the pair. The relative non-gravitational acceleration measurement error along the LoS is then calculated using the RMS. It is assumed that the same measurement error is experienced by the leading satellite but is independent for simplification.
2. The leading satellite is used in the simulation only to guide the attitude of the trailing satellite. TudatPy allows defining a rotation model on the satellite where the body-fixed x-axis is imposed to lie in a user-defined inertial direction. This inertial direction for the

trailing satellite to point to is the LoS vector connecting the pair. The outputted quaternions are used to obtain the attitude information of the satellite. It is assumed that the attitude information output has no interruptions.

3. The x-axis of the trailing satellite points along the LoS vector connecting the pair, which is roughly along the orbit, the z-axis roughly in the nadir direction, and the y-axis completing the right-hand coordinate system.

Table 5.1 lists the initial conditions used for orbit simulation. The orbital altitude $396\,\mathrm{km}$, inclination of $65°$, and a separation of $220\,\mathrm{km}$ between the satellites for the inclined pair is considered (Cesare et al., 2022). The eccentricity is zero for a circular orbit. The argument of periapsis does not mean much for a circular orbit. The true anomaly, the longitude of the ascending node, with the argument of periapsis, is arbitrarily chosen, at least ensuring that the pair experiences the eclipse phase.

Table 5.1: Initial conditions for the orbit

Kepler elements			
Semi-major axis a	6774 km	Longitude of ascending node Ω	23.4 °
Eccentricity e	0	True anomaly of NGGM 1 θ	30 °
Inclination i	65 °	Distance b/w NGGM 1 & 2	220 km
Argument of periapsis ω	20 °		

The GRACE-FO satellite (Wen et al., 2019) is used as a reference to define the aerodynamic and radiation pressure model of the NGGM pair. The aerodynamic acceleration is modelled by

$$\ddot{\boldsymbol{r}}_{aero} = -\frac{1}{m}\boldsymbol{R}^{I/AF}\left(\frac{1}{2}\rho v_{air}^{2} S_{ref}\begin{bmatrix} C_D \\ 0 \\ 0 \end{bmatrix}\right) \tag{5.1}$$

where m is the mass of the satellite, $\boldsymbol{R}^{I/AF}$ is the rotation matrix from the satellite's aerodynamic frame to the inertial frame, ρ is the atmospheric density at the current satellite position, v_{air} is the satellite's airspeed w.r.t. Earth's atmosphere, S_{ref} is the reference area of the satellite, and C_D is the drag coefficient in satellite's aerodynamic frame. The lift and side force coefficients are not considered because the incident velocity is mainly in the along-track direction. A $C_D = 2.5$ (Wöske et al., 2019), $S_{ref} = 0.955\,\mathrm{m}^2$ (Wen et al., 2019), and the NRLMSIS00 atmosphere model for density is chosen for the aerodynamic interface. NRLMSIS00 is widely used as it provides a global representation of the atmosphere and is readily available in TudatPy.

For the radiation pressure acceleration, a box model of the satellite is constructed using the inbuilt functionalities of TudatPy. The Sun is defined as an isotropic point source with an irradiance of $1361\,\mathrm{W\,m^{-2}}$ at $1\,\mathrm{AU}$ for direct solar radiation. The Earth is modelled as an extended source discredited into panels (Knocke et al., 1988; Stiller, 2023) for albedo and thermal radiation. The satellite is defined as a rectangular box with identical reflection law settings for all the panels. As mentioned, GRACE-FO is used as a reference with the parameters defined in Table 5.2.

Table 5.2: Box model parameters (Wen et al., 2019)

Parameter	Value
Length [m]	3.1225
Width [m]	1.944
Height [m]	0.775
Specular reflection coefficient [-]	0.4
Diffuse reflection coefficient [-]	0.26

To integrate the orbit, an RK4 integrator with a fixed step size of $1\,\mathrm{s}$ is selected since the accelerometer output data frequency for calibration will be $1\,\mathrm{Hz}$. Figure 5.2a shows the norm of the position error for the Euler and RK4 integrators w.r.t. a benchmark orbit calculated with the RK4 integrator with a fixed time step of $0.25\,\mathrm{s}$. The Euler integrator yields a high position error from the start of the orbit, with the error reaching up to $1000\,\mathrm{km}$. The RK4 integrator is stable and has an error less than $1\,\mathrm{mm}$.

A simple point-mass gravity field of Earth is utilized for the gravitational models in orbit generation. Figure 5.2b shows the effect of adding different gravity field models on the position difference w.r.t. to the point mass model of Earth. The effect of Jupiter is negligible, with the Sun and Moon affecting the position by a few tens of metres. However, the position is greatly affected by using a point mass model compared to a high fidelity (e.g. D/O 120) gravity field model of Earth. The position is only of concern in the acceleration signal generation because the gravity gradients effect on the accelerometer signal is a function of the satellite's position w.r.t. Earth. However, the RMS difference in the gravity gradients is approximately 10% (analysis not shown). The majority of the position error is in the along- (blue line) and cross-track (orange line) direction of the orbit, and only a few kilometres in the altitude (green line) as highlighted in Figure 5.3. The gravity gradients calculation is decoupled from orbit generation using a gravity gradients calculator (Personal Communication: C. Siemes). During the early stages of development, multiple orbits generation was envisioned, which would lead to long integration times for orbit if a detailed Earth model is used. Therefore, a point mass model of Earth is picked for quick orbit generation, and subsequently, a detailed model is chosen in the gravity gradients calculator to generate a realistic accelerometer signal.

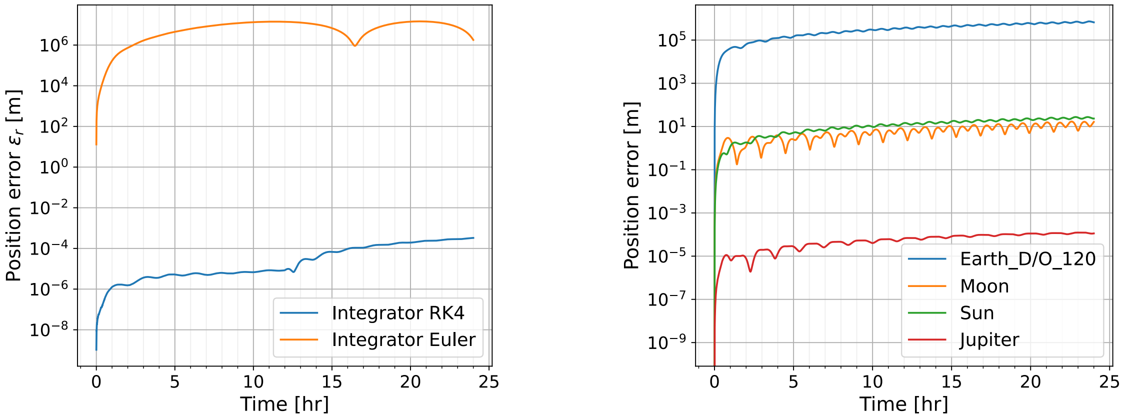

(a) **(b)**

Figure 5.2: a) Norm of position error of Euler and RK4 integrator over the course of the day with a time step of $1\,\mathrm{s}$ when compared to a benchmark RK4 with a time step of $0.25\,\mathrm{s}$. b) Norm of position difference due to the addition of an acceleration model to the point mass model of Earth w.r.t. to just a point mass model of Earth.

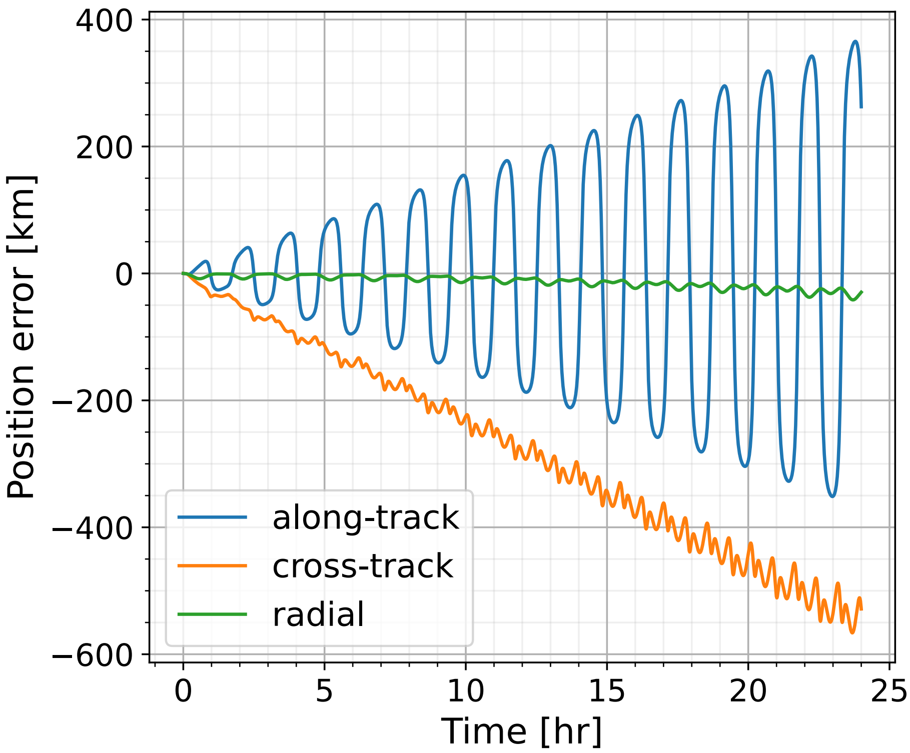

Figure 5.3: Position error between Earth's D/O = 120 and point mass model in the Local-Vertical, Local-Horizontal frame of reference

The acceleration acting on the satellites in the pseudo-inertial J2000 frame, with the origin at the centre of Earth can then be represented as

$$\ddot{\boldsymbol{r}}_{tot} = -\frac{\mu}{|\boldsymbol{r}_{Es}|^3}\boldsymbol{r}_{Es} + \ddot{\boldsymbol{r}}_{ng}, \tag{5.2}$$

where $\ddot{\boldsymbol{r}}_{tot}$ is the total acceleration acting on the satellite's COM, $\boldsymbol{r}_{Es}$ is the position of a satellite relative to Earth in the J2000 frame, $\ddot{\boldsymbol{r}}_{ng}$ is the non-gravitational acceleration consisting of the aerodynamic and radiation pressure accelerations, and μ is Earth's gravitational parameter with a value of $398\,600\,\mathrm{km^3/s^2}$ [1].

The spacecraft position obtained after integrating the orbit is inputted in a gravity gradients calculator to get the gravity gradients in the satellite's body-fixed frame to generate a realistic signal. Figure 5.4 compares the ASD sensitivity of the acceleration signal generated V_{zz} gravity gradient for an off-centre accelerometer placement for different D/O gravity field against the accelerometer noise in the frequency domain (refer to Section 5.1.2 for accelerometer noise generation). The vertical drop represents the upper limit contribution to the acceleration signal in the frequency domain for the given D/O gravity field. The higher D/O inclusion adds signal to the high frequencies, but eventually, at D/O = 130, the signal strength from V_{zz} falls below the defined accelerometer noise level, making it indistinguishable from noise. V_{zz} was the limiting gravity gradient for selecting the D/O out of the six gravity gradients (not shown), thus selecting a D/O for V_{zz} will be applicable for other gravity gradients as well.

---

[1] https://nssdc.gsfc.nasa.gov/planetary/factsheet/earthfact.html

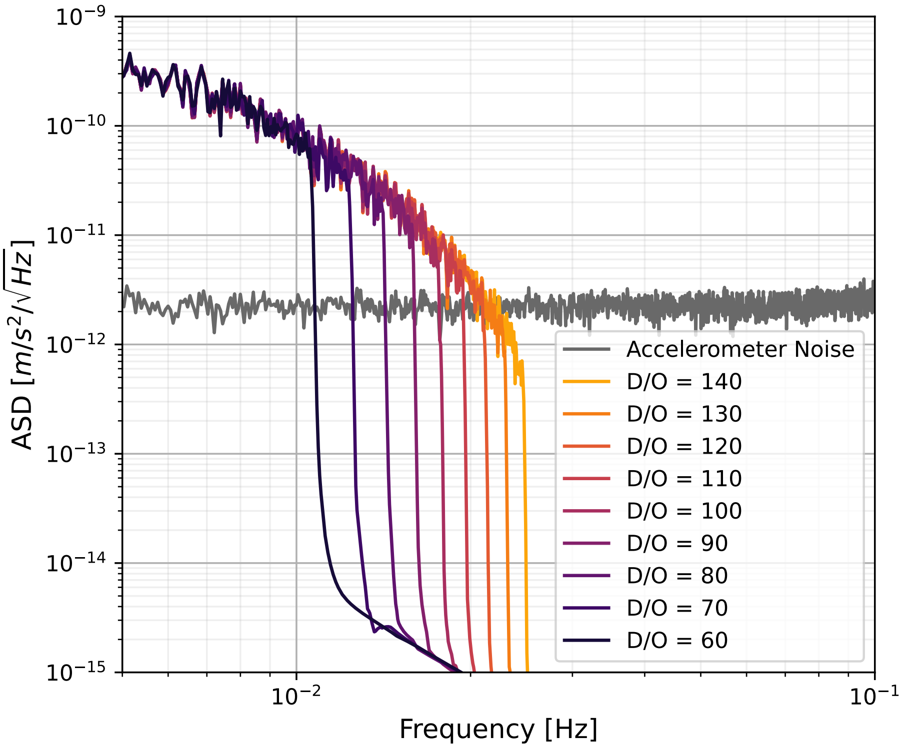

Figure 5.4: Sensitivity of V_{zz} gravity gradient for an off-centre accelerometer for various D/O of gravity field compared against the accelerometer noise.

Thus, the non-gravitational acceleration $\boldsymbol{a}_{ng}$, the quaternions $\boldsymbol{q}$ describing the attitude and the gravity gradients based on D/O 130 outputted by the orbital simulation are used as an input to build the acceleration signal in Section 5.1.2.

5.1.2. Accelerometer Model

A perfect accelerometer that is rigidly mounted on board the satellite away from the COM measures the true acceleration at the nominal position $\boldsymbol{r}_i^{np}$ in a body-fixed frame of the satellite as

$$\boldsymbol{a}_i^{np} = -(\boldsymbol{V} - \boldsymbol{\Omega}^2 - \dot{\boldsymbol{\Omega}})\boldsymbol{r}_i^{np} + \boldsymbol{a}_{ng}, \tag{5.3}$$

where $\boldsymbol{V}$ is the gravity gradient tensor, $\dot{\boldsymbol{\Omega}}$ is the angular acceleration matrix and $\boldsymbol{\Omega}$ is the angular rate matrix (referred collectively as rotational acceleration terms), and $\boldsymbol{a}_{ng}$ is the non-gravitational acceleration. The matrices definition is as follows:

$$\boldsymbol{V} = \begin{bmatrix} V_{xx} & V_{xy} & V_{xz} \\ V_{xy} & V_{yy} & V_{yz} \\ V_{xz} & V_{yz} & V_{zz} \end{bmatrix}, \qquad \boldsymbol{\Omega} = \begin{bmatrix} 0 & -\omega_z & \omega_y \\ \omega_z & 0 & -\omega_x \\ -\omega_y & \omega_x & 0 \end{bmatrix},$$

$$\dot{\boldsymbol{\Omega}} = \begin{bmatrix} 0 & -\dot{\omega}_z & \dot{\omega}_y \\ \dot{\omega}_z & 0 & -\dot{\omega}_x \\ -\dot{\omega}_y & \dot{\omega}_x & 0 \end{bmatrix}, \qquad \boldsymbol{\Omega}^2 = \begin{bmatrix} -\omega_y^2 - \omega_z^2 & \omega_x\omega_y & \omega_x\omega_z \\ \omega_x\omega_y & -\omega_x^2 - \omega_z^2 & \omega_y\omega_z \\ \omega_x\omega_z & \omega_y\omega_z & -\omega_x^2 - \omega_y^2 \end{bmatrix}$$

Taking the experience from GOCE, a comprehensive model of the measured acceleration by an accelerometer is represented as (Siemes et al., 2019)

$$\boldsymbol{a}_i^{meas} = \boldsymbol{b}_i + \boldsymbol{M}_i\boldsymbol{a}_i + \boldsymbol{K}_i\boldsymbol{a}_i^2 + \boldsymbol{W}_i\dot{\boldsymbol{w}}_i + \boldsymbol{n}_i, \tag{5.4}$$

where $\boldsymbol{a}_i^{meas}$ is the measured acceleration, $\boldsymbol{b}_i$ is the acceleration bias, $\boldsymbol{a}_i$ is the true acceleration at the real accelerometer position (potentially deviating from the nominal position), $\boldsymbol{M}_i$ is the calibration matrix accounting for scale factors, misalignments and non-orthogonality of the accelerometer sensitive axes, $\boldsymbol{K}_i$ is the diagonal quadratic factor matrix, $\boldsymbol{W}_i$ is the angular acceleration coupling matrix consisting three non-zero elements depending on the electrode layout and proof mass control, $\dot{\boldsymbol{\omega}}_i$ is the true angular acceleration, and $\boldsymbol{n}_i$ is the measurement noise.

The true acceleration $\boldsymbol{a}_i$ for an accelerometer at a real location $\boldsymbol{r}_i$ is

$$\boldsymbol{a}_i = -(\boldsymbol{V} - \boldsymbol{\Omega}^2 - \dot{\boldsymbol{\Omega}})\boldsymbol{r}_i + \boldsymbol{a}_{ng}. \tag{5.5}$$

For further mathematical derivations, two types of acceleration modes are defined: differential and common mode accelerations as

$$\boldsymbol{a}_{dij} = \frac{1}{2}(\boldsymbol{a}_i - \boldsymbol{a}_j) \tag{5.6}$$

$$\boldsymbol{a}_{cij} = \frac{1}{2}(\boldsymbol{a}_i + \boldsymbol{a}_j). \tag{5.7}$$

This facilitates rewriting the model as follows:

$$\begin{bmatrix}\boldsymbol{a}_{dij}^{meas}\\ \boldsymbol{a}_{cij}^{meas}\end{bmatrix} = \begin{bmatrix}\boldsymbol{b}_{dij}\\ \boldsymbol{b}_{cij}\end{bmatrix} + \begin{bmatrix}\boldsymbol{M}_{cij} & \boldsymbol{M}_{dij}\\ \boldsymbol{M}_{dij} & \boldsymbol{M}_{cij}\end{bmatrix}\begin{bmatrix}\boldsymbol{a}_{dij}\\ \boldsymbol{a}_{cij}\end{bmatrix} + \frac{1}{2}\begin{bmatrix}\boldsymbol{K}_i & -\boldsymbol{K}_j\\ \boldsymbol{K}_i & \boldsymbol{K}_j\end{bmatrix}\begin{bmatrix}\boldsymbol{a}_j^2\\ \boldsymbol{a}_j^2\end{bmatrix} + \begin{bmatrix}\boldsymbol{W}_{dij}\\ \boldsymbol{W}_{cij}\end{bmatrix}\dot{\boldsymbol{\omega}} + \begin{bmatrix}\boldsymbol{n}_{dij}\\ \boldsymbol{n}_{cij}\end{bmatrix}, \tag{5.8}$$

where all the variables in differential and common mode are defined analogously. The calibration requires the accelerometer at the nominal intended positions as this defines the signal it senses. Thus, the differential and common mode signal sensed by the accelerometers at the nominal positions is

$$\boldsymbol{a}_{dij}^{np} = -(\boldsymbol{V} - \boldsymbol{\Omega}^2 - \dot{\boldsymbol{\Omega}})\boldsymbol{r}_{dij}^{np}, \tag{5.9}$$

$$\boldsymbol{a}_{cij}^{np} = -(\boldsymbol{V} - \boldsymbol{\Omega}^2 - \dot{\boldsymbol{\Omega}})\boldsymbol{r}_{cij}^{np} + \boldsymbol{a}_{ng}. \tag{5.10}$$

But the real accelerometer positions $\boldsymbol{r}_i$ will have a slight deviation from the nominal position $\boldsymbol{r}_i^{np}$ modelled by

$$\boldsymbol{r}_i = \boldsymbol{r}_i^{np} + \delta\boldsymbol{r}_i, \tag{5.11}$$

where $\delta\boldsymbol{r}_i$ is the position deviation. Thus, the acceleration at the real position can be written in terms of the nominal position:

$$\boldsymbol{a}_i = -(\boldsymbol{V} - \boldsymbol{\Omega}^2 - \dot{\boldsymbol{\Omega}})(\boldsymbol{r}_i^{np} + \delta\boldsymbol{r}_i) + \boldsymbol{a}_{ng} = \boldsymbol{a}_i^{np} - (\boldsymbol{V} - \boldsymbol{\Omega}^2 - \dot{\boldsymbol{\Omega}})\delta\boldsymbol{r}_i, \tag{5.12}$$

$$\boldsymbol{a}_{dij} = -(\boldsymbol{V} - \boldsymbol{\Omega}^2 - \dot{\boldsymbol{\Omega}})(\boldsymbol{r}_{dij}^{np} + \delta\boldsymbol{r}_{dij}) = \boldsymbol{a}_{dij}^{np} - (\boldsymbol{V} - \boldsymbol{\Omega}^2 - \dot{\boldsymbol{\Omega}})\delta\boldsymbol{r}_{dij}, \tag{5.13}$$

$$\boldsymbol{a}_{cij} = -(\boldsymbol{V} - \boldsymbol{\Omega}^2 - \dot{\boldsymbol{\Omega}})(\boldsymbol{r}_{cij}^{np} + \delta\boldsymbol{r}_{cij}) + \boldsymbol{a}_{ng} = \boldsymbol{a}_{cij}^{np} - (\boldsymbol{V} - \boldsymbol{\Omega}^2 - \dot{\boldsymbol{\Omega}})\delta\boldsymbol{r}_{cij}. \tag{5.14}$$

By substituting the above relations in Equation 5.4, the measured acceleration can be expressed in terms of acceleration sensed at nominal positions plus all the relevant parameters required for calibration as

$$\boldsymbol{a}_i^{meas} = \boldsymbol{b}_i + \boldsymbol{M}_i(\boldsymbol{a}_i^{np} - (\boldsymbol{V} - \boldsymbol{\Omega}^2 - \dot{\boldsymbol{\Omega}})\delta\boldsymbol{r}_i) + \boldsymbol{K}_i(\boldsymbol{a}_i^{np} - (\boldsymbol{V} - \boldsymbol{\Omega}^2 - \dot{\boldsymbol{\Omega}})\delta\boldsymbol{r}_i)^2 + \boldsymbol{W}_i\dot{\boldsymbol{w}}_i + \boldsymbol{n}_i. \quad (5.15)$$

Adding Accelerometer Hardware Imperfections

Once a true acceleration signal at nominal position is constructed using Equation 5.3, hardware imperfections defined in Equation 5.15 are introduced to generate a measured accelerometer signal that a real accelerometer may observe.

The matrix structure of the $\boldsymbol{W}_i$ is assumed to be

$$\boldsymbol{W}_i = \begin{bmatrix} 0 & 0 & 0 \\ W_{i,21} & 0 & W_{i,23} \\ 0 & W_{i,32} & 0 \end{bmatrix}. \quad (5.16)$$

The matrix structure depends on the electrode layout and the accelerometer's proof mass control. Here, it is assumed that the x-axis electrodes control only linear accelerations, the y-axis controls roll and yaw, and the z-axis controls the pitch of the proof mass, where x-, y-, and z-axis are defined in the satellite's body-fixed frame of reference. The matrix structure is assumed to be the same for all layouts.

The imperfections are drawn from a standard normal distribution with the definitions provided in Table 5.3. The values are judged based on the values reported by Siemes et al. (2019) as the accelerometers on board NGGM will be supplied by ONERA, similar to the ones on GOCE if not better (Christophe et al., 2018).

Table 5.3: Generation of accelerometer imperfections

$\boldsymbol{M}_i = \boldsymbol{I}_{3x3} + 10^{-3} \times N(0,1)_{3x3}$
$\boldsymbol{K}_i \sim 10 \times N(0,1)_{3x3}$
$W_{i,21}, W_{i,23}, W_{i,32} \sim 10^{-4} \times N(0,1)$
$\delta\boldsymbol{r}_{d13} \sim 10^{-3} \times N(0,1)_{3x1}$
$\delta\boldsymbol{r}_{c13} \sim 10^{-3} \times N(0,1)_{3x1}$

The individual accelerometer position offsets can be derived from the differential and common mode offsets:

$$\delta\boldsymbol{r}_1 = \delta\boldsymbol{r}_{c13} + \delta\boldsymbol{r}_{d13} \qquad \delta\boldsymbol{r}_3 = \delta\boldsymbol{r}_{cij} - \delta\boldsymbol{r}_{dij} \quad (5.17)$$

The final hardware imperfection to generate a measured signal is adding the noise $\boldsymbol{n}_i$. It is assumed that ASDs are given as one-sided spectral density plots, and all subsequent methods involving Fast Fourier Transform (FFT) are based on the one-sided spectral density definition. For a real signal, the amplitude spectrum is symmetric across the positive and negative frequencies (S. W. Smith, 1999). In a noise signal, the signal's phase is randomized and does not matter. Thus, to generate a noise signal with a given ASD, one simply has to convolve its impulse response with the white noise $w(t)$, which is equivalent to multiplying these signals in the frequency domain. The steps are summarized in Algorithm 1. The bias is not generated as the method anyways filters out the bias in the measured signal (refer to Section 5.2.2)

Algorithm 1 Generation of a noise signal from a desired ASD

```
1: Create a one-sided amplitude spectrum of the desired ASD $A(f)$ for $f_k = \frac{k-1}{2K}$ for $k \in [0, K]$ where K is an odd integer
2: Take the inverse FFT to get the impulse response in time domain $\rightarrow$ IFFT$(A(f)) = v(t)$
3: Create a white noise signal $\rightarrow w(t)$
4: Convolve the impulse response with white noise signal $\rightarrow v(t) * w(t)$    ▷ Equivalent to multiplication in frequency domain
```

A few considerations when applying algorithm 1.

1. The number of frequency points of the ASD has to be odd so that it generates a symmetric impulse response in the time domain. This is important because a FFT operation assumes any input to be a periodic signal, with each period repeating every K point selected (lag of length K). With an odd integer of points, the signal can be shifted in the selected time domain and maintain symmetry.
2. A convolution of a signal of length N with a filter of length M generates an output of (N+M-1) length. But in a convolution operation, the first and last M points are affected by edge effects (S. W. Smith, 1999). Therefore, the white noise generated must be of length (N+M-1), where N is the length of the acceleration signal, such that after convolution with the filter, the truncated output signal equals the length of the input signal.

The linear acceleration noise ASD of the accelerometer defined by Equation 3.4 and generated using Algorithm 1 is given in Figure 5.5a. The black line is the desired ASD defined by the Equation 3.4, and the ASD of the noise in the x,y and z direction after applying Algorithm 1 is given by the coloured lines. The ASD is obtained by taking the square root of Power Spectral Density (PSD) estimated by a modified method described by Welch (1967), where the mean is replaced by the median for robustness to outliers and selection of Hann window for windowing (Harris, 1978). The ASD shape of the generated noise follows the defined analytical ASD description of the instrument.

The angular acceleration noise is similarly generated. However, since the attitude information is available from the star trackers and the accelerometer, as explained in subsection 3.3.4, the noise ASDs defined by Equations (3.7) and (3.8) can be combined optimally as (Stummer et al., 2011)

$$A(f)_{\dot{\omega},comb} = \left(\frac{1}{[A(f)_\theta (2\pi f)^2]^2} + \frac{1}{A(f)^2_{\dot{\omega}}} \right)^{-1}. \tag{5.18}$$

The noise spectra after data fusion are shown in Figure 5.5b. The angular acceleration noise (black line) and star sensor noise (purple line) are defined analytically by Equations (3.7) and (3.8), respectively. The red line is the reconstructed analytical ASD obtained from Equation 5.18. The blue, orange and green lines show the final angular acceleration noise in x, y and z. The reconstruction shows that above $0.1\,\mathrm{mHz}$, the accelerometer provides a less noisy reading of the angular accelerations than the star trackers.

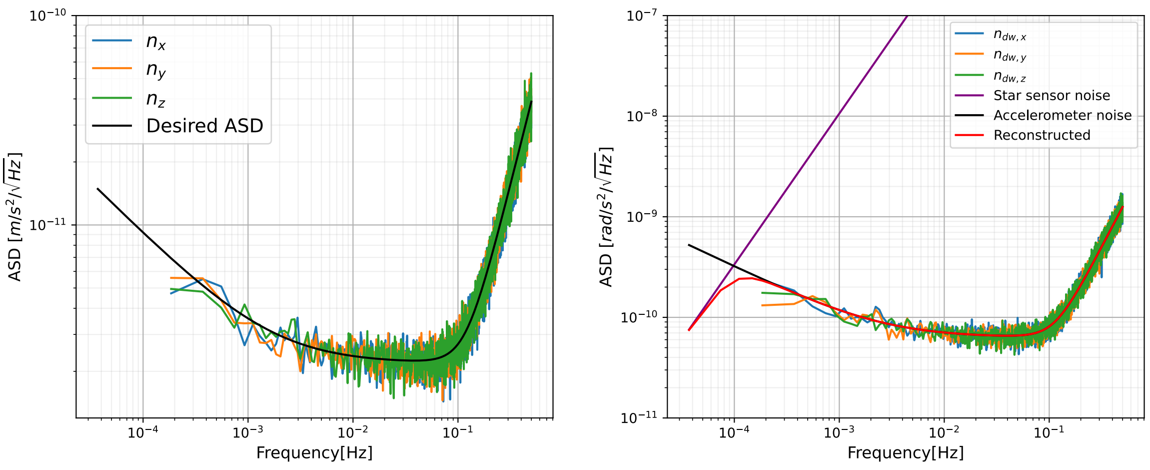

(a) **(b)**

Figure 5.5: a) ASD of accelerometer's linear acceleration noise. b) ASD of the reconstructed angular acceleration noise.

Finally, the thruster noise defined by Equation 3.6 is similarly generated. The thruster noise and linear acceleration noise are added to $\boldsymbol{a}_{ng}$, the angular acceleration noise to $\dot{\boldsymbol{\omega}}_i$, and the angular rate noise to $\boldsymbol{\omega}_i$, which is found by simply integrating the angular acceleration noise using a trapezoidal integration scheme.

5.1.3. Shaking Manoeuvre

The shaking manoeuvre signals will be generated similarly to the noise generation described in subsection 5.1.2. Figure 5.6 shows an example ASD of a shaking signal. It follows the same steps as noise generation, with the analytical ASD being defined first, followed by convolution with white noise. Four parameters define the shaking signal, with the first three defining the analytical ASD of the shaking signal in the frequency domain:

1. Thrust acceleration magnitude of ASD T_{acc}: The thrust acceleration magnitude defines the ceiling of the rectangular pulse shown in Figure 5.6.
2. Upper bound frequency f_{UB}: The frequency at which the pulse drops to a lower level.
3. Lower bound frequency f_{LB}: The frequency at which the pulse rises to the ceiling.
4. Shaking duration t_{sh}: Parameter to set the duration of the shaking of the satellite. In this chapter, the shaking duration is fixed to 24 hrs. In Chapter 7, different shaking durations are analysed.

The lower bound frequency f_{LB} is fixed to be 4 units $(0.4 f_{UB})$ lower than the upper bound frequency f_{UB}, throughout the thesis. The bandwidth BW of the pulse was found to be not an influential factor; thus, it was fixed to a similar width used for the GOCE mission. The lower level of the signal in the frequencies below f_{LB} is an order of magnitude lower than that inside the bandwidth of the pulse. Since the accelerometer has a sampling frequency of $1\,\mathrm{Hz}$, after f_{UB}, the ASD is defined to linearly decrease until $0.5\,\mathrm{Hz}$ to resemble the shaking signal signature used for GOCE. Equation 5.19 encapsulates the steps listed above.

$$A(f)_{shaking} = \begin{cases} T_{acc}/10, & f < f_{LB} \\ T_{acc}, & f_{LB} < f < f_{UB} \\ -\frac{T_{acc}}{10}\left(\frac{f - f_{UB}}{0.5 - f_{UB}} - 1\right), & f > f_{UB} \end{cases} \tag{5.19}$$

$$f_{LB} = f_{UB} - (0.4 \cdot f_{UB}) \tag{5.20}$$

The shaking signal is defined to be identical for all three axes for both linear and angular accelerations.

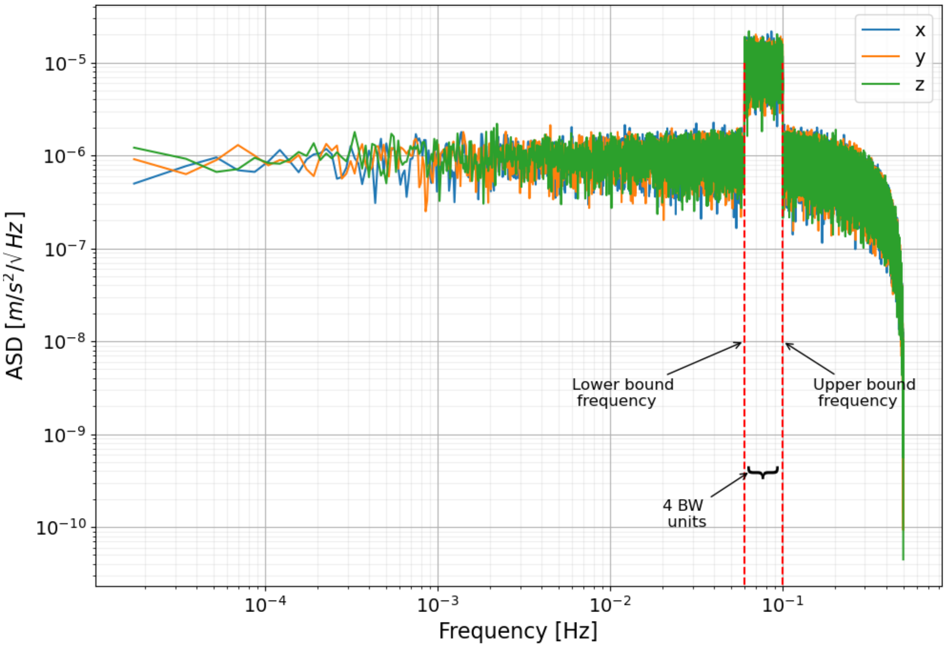

Figure 5.6: ASD of the shaking signal.

5.2. Accelerometer Calibration

With the data generation tool implemented (Section 5.1), the data generated can be used as input for the calibration tool to estimate the imperfections. Section 5.2.1 outlines the observation equations to set up the non-linear least squares problem. Section 5.2.2 then explains the least squares fit and the need to linearize the observation equations, which is subsequently done in Section 5.2.3. Next,Section 5.2.4 highlights the setup of the equations in the code, and finally, a summary of the whole process is presented in Section 5.2.5.

5.2.1. Derivation of Observation Equations

As discussed in Section 3.3.2, three configurations will be implemented, named Layouts 2, 3 and 4, for two, three and four accelerometers on board, respectively. Below, the equations for Layout 3 placed on the y-axis will be outlined in detail as it has both the differential and the common mode equations. Layouts 2 and 4 with different axis placements can be analogously derived (not shown).

Assume the origin is at the satellite's COM in the satellite's frame of reference. The nominal positions of the accelerometers are then defined as

$$\boldsymbol{r}_1^{np} = \begin{bmatrix} 0 \\ \frac{L_y}{2} \\ 0 \end{bmatrix}, \qquad \boldsymbol{r}_2^{np} = \begin{bmatrix} 0 \\ 0 \\ 0 \end{bmatrix}, \qquad \boldsymbol{r}_3^{np} = \begin{bmatrix} 0 \\ -\frac{L_y}{2} \\ 0 \end{bmatrix}, \tag{5.21}$$

where is the L_y is the gradiometer arm length (line connecting accelerometers 1 and 3). Thus, accelerometers 1 and 3 are placed symmetrically around the COM, and accelerometer 2 is at the COM. The accelerations can be simplified to

$$\boldsymbol{a}_2^{np} = \boldsymbol{a}_{c13}^{np} = \boldsymbol{a}_{ng}, \tag{5.22}$$

$$\boldsymbol{a}_{d13}^{np} = -(\boldsymbol{V} - \boldsymbol{\Omega}^2 - \dot{\boldsymbol{\Omega}})\boldsymbol{r}_{d13}^{np}. \tag{5.23}$$

With a constellation of three accelerometers, there are a total of nine observations available ($\boldsymbol{a}_1^{meas}$, $\boldsymbol{a}_2^{meas}$, $\boldsymbol{a}_3^{meas}$). The gravity gradients $\boldsymbol{V}$ and the rotational terms $\boldsymbol{\Omega}$ and $\dot{\boldsymbol{\Omega}}$ are known from the satellite position and quaternions, leaving the three components of $\boldsymbol{a}_{ng}$ as unknowns. Thus, we have six equations that can be used to solve for the calibration parameters. The first set of three equations is based on the differential mode derived from Equation 5.8:

$$\boldsymbol{a}_{d13}^{meas} = \boldsymbol{b}_{d13} + \boldsymbol{M}_{c13}\boldsymbol{a}_{d13} + \boldsymbol{M}_{d13}\boldsymbol{a}_{c13} + \frac{1}{2}\boldsymbol{K}_1\boldsymbol{a}_1^2 - \frac{1}{2}\boldsymbol{K}_3\boldsymbol{a}_3^2 + \boldsymbol{W}_{d13}\dot{\boldsymbol{\omega}} + \boldsymbol{n}_{d13}. \tag{5.24}$$

Inserting the acceleration at nominal positions yields

$$\begin{aligned} \boldsymbol{a}_{d13}^{meas} = \boldsymbol{b}_{d13} &+ \boldsymbol{M}_{c13}(\boldsymbol{a}_{d13}^{np} - (\boldsymbol{V} - \boldsymbol{\Omega}^2 - \dot{\boldsymbol{\Omega}})\delta\boldsymbol{r}_{d13}) \\ &+ \boldsymbol{M}_{d13}(\boldsymbol{a}_{c13}^{np} - (\boldsymbol{V} - \boldsymbol{\Omega}^2 - \dot{\boldsymbol{\Omega}})\delta\boldsymbol{r}_{c13}) \\ &+ \frac{1}{2}\boldsymbol{K}_1(\boldsymbol{a}_1^{np} - (\boldsymbol{V} - \boldsymbol{\Omega}^2 - \dot{\boldsymbol{\Omega}})\delta\boldsymbol{r}_1)^2 \\ &- \frac{1}{2}\boldsymbol{K}_3(\boldsymbol{a}_3^{np} - (\boldsymbol{V} - \boldsymbol{\Omega}^2 - \dot{\boldsymbol{\Omega}})\delta\boldsymbol{r}_3)^2 \\ &+ \boldsymbol{W}_{d13}\dot{\boldsymbol{\omega}} + \boldsymbol{n}_{d13}. \end{aligned} \tag{5.25}$$

Based on Equation (5.25), the scalar parameter δr_{d13y} cannot be estimated as it has the same effect as scaling $\boldsymbol{a}_{d13}^{np}$ which is accounted by the matrix $\boldsymbol{M}_{c13}$. Furthermore, Equation 5.25 is a non-linear function requiring linearization for performing a least squares fit. Let $\boldsymbol{M}_{c13} = \boldsymbol{H}_{c13} + \delta\delta\boldsymbol{M}_{c13}$, where $\boldsymbol{H}_{c13} = \boldsymbol{I} + \delta\boldsymbol{M}_{c13}$ is an approximation, with a deviation of $\delta\boldsymbol{M}_{c13}$ from the identity matrix, of $\boldsymbol{M}_{c13}$ with $\delta\delta\boldsymbol{M}_{c13}$ an update to the approximation. $\boldsymbol{M}_{d13}$ is defined analogously.

Substituting the definitions to Equation 5.26 leads to acceleration as a function of acceleration at nominal positions and the calibration parameters:

$$\begin{aligned} \boldsymbol{a}_{d13}^{meas} = \boldsymbol{f}_d(\delta\delta\boldsymbol{M}_{c13}, ...) = \boldsymbol{b}_{d13} &+ (\boldsymbol{H}_{c13} + \delta\delta\boldsymbol{M}_{c13})(\boldsymbol{a}_{d13}^{np} - (\boldsymbol{V} - \boldsymbol{\Omega}^2 - \dot{\boldsymbol{\Omega}})\delta\boldsymbol{r}_{d13}) \\ &+ (\boldsymbol{H}_{d13} + \delta\delta\boldsymbol{M}_{d13})(\boldsymbol{a}_{c13}^{np} - (\boldsymbol{V} - \boldsymbol{\Omega}^2 - \dot{\boldsymbol{\Omega}})\delta\boldsymbol{r}_{c13}) \\ &+ \frac{1}{2}\boldsymbol{K}_1(\boldsymbol{a}_1^{np} - (\boldsymbol{V} - \boldsymbol{\Omega}^2 - \dot{\boldsymbol{\Omega}})\delta\boldsymbol{r}_1)^2 \\ &- \frac{1}{2}\boldsymbol{K}_3(\boldsymbol{a}_3^{np} - (\boldsymbol{V} - \boldsymbol{\Omega}^2 - \dot{\boldsymbol{\Omega}})\delta\boldsymbol{r}_3)^2 \\ &+ \boldsymbol{W}_{d13}\dot{\boldsymbol{\omega}} + \boldsymbol{n}_{d13}. \end{aligned} \tag{5.26}$$

The second set of three equations is based on common mode acceleration from Equation 5.22:

$$\boldsymbol{0} = \boldsymbol{a}_{c13}^{np} - \boldsymbol{a}_{2}^{np} = \boldsymbol{a}_{c13} - \boldsymbol{a}_2 + (\boldsymbol{V} - \boldsymbol{\Omega}^2 - \dot{\boldsymbol{\Omega}})(\delta\boldsymbol{r}_{c13} - \delta\boldsymbol{r}_2). \tag{5.27}$$

Using Equations (5.4) and (5.8) to write the true acceleration at real position as a function of measured acceleration, Equation 5.27 can be expanded to

$$\begin{aligned} \boldsymbol{0} = \boldsymbol{M}_{c13}^{-1}&[\boldsymbol{a}_{c13}^{meas} - \boldsymbol{b}_{c13} - \boldsymbol{M}_{d13}\boldsymbol{a}_{d13} - \frac{1}{2}\boldsymbol{K}_1\boldsymbol{a}_1^2 - \frac{1}{2}\boldsymbol{K}_3\boldsymbol{a}_3^2 - \boldsymbol{W}_{c13}\dot{\boldsymbol{\omega}} - \boldsymbol{n}_{c13}] \\ -\boldsymbol{M}_2^{-1}&[\boldsymbol{a}_2^{meas} - \boldsymbol{b}_2 - \frac{1}{2}\boldsymbol{K}_2\boldsymbol{a}_2^2 - \boldsymbol{W}_2\dot{\boldsymbol{\omega}} - \boldsymbol{n}_2] + (\boldsymbol{V} - \boldsymbol{\Omega}^2 - \dot{\boldsymbol{\Omega}})(\delta\boldsymbol{r}_{c13} - \delta\boldsymbol{r}_2). \end{aligned} \tag{5.28}$$

Using the definitions $\boldsymbol{H}_2 = \boldsymbol{I} + \delta\boldsymbol{M}_2$ and $\boldsymbol{H}_{c13} = \boldsymbol{I} + \delta\boldsymbol{M}_{c13}$ and the acceleration at nominal positions, the final form of the observation equation is

$$\begin{aligned} \boldsymbol{0} = \boldsymbol{f}_c(\delta\delta\boldsymbol{M}_2, ...) =&[\boldsymbol{H}_{c13}^{-1} - \boldsymbol{H}_{c13}^{-1}\delta\delta\boldsymbol{M}_{c13}\delta\delta\boldsymbol{H}_{c13}^{-1}]\cdot \\ &[\boldsymbol{a}_{c13}^{meas} - \boldsymbol{b}_{c13} - \boldsymbol{M}_{d13}(\boldsymbol{a}_{d13}^{np} - (\boldsymbol{V} - \boldsymbol{\Omega}^2 - \dot{\boldsymbol{\Omega}})\delta\boldsymbol{r}_{d13}) \\ &- \frac{1}{2}\boldsymbol{K}_1(\boldsymbol{a}_1^{np} - (\boldsymbol{V} - \boldsymbol{\Omega}^2 - \dot{\boldsymbol{\Omega}})\delta\boldsymbol{r}_1)^2 - \frac{1}{2}\boldsymbol{K}_3(\boldsymbol{a}_3^{np} - (\boldsymbol{V} - \boldsymbol{\Omega}^2 - \dot{\boldsymbol{\Omega}})\delta\boldsymbol{r}_3)^2 \\ &- \boldsymbol{W}_{c13}\dot{\boldsymbol{\omega}} - \boldsymbol{n}_{c13}] \\ &-[\boldsymbol{H}_2^{-1} - \boldsymbol{H}_2^{-1}\delta\delta\boldsymbol{M}_2\boldsymbol{H}_2^{-1}]\cdot[\boldsymbol{a}_2^{meas} - \boldsymbol{b}_2 - \frac{1}{2}\boldsymbol{K}_2(\boldsymbol{a}_2^{np} - (\boldsymbol{V} - \boldsymbol{\Omega}^2 - \dot{\boldsymbol{\Omega}})\delta\boldsymbol{r}_2)^2) \\ &- \boldsymbol{W}_2\dot{\boldsymbol{\omega}} - \boldsymbol{n}_2] + (\boldsymbol{V} - \boldsymbol{\Omega}^2 - \dot{\boldsymbol{\Omega}})(\delta\boldsymbol{r}_{c13} - \delta\boldsymbol{r}_2). \end{aligned} \tag{5.29}$$

Note that the parameter $\delta\boldsymbol{r}_2$ is assumed to be zero by adjusting the satellite's COM with trim masses. Refer to Appendix A.1 for derivation of $\boldsymbol{M}_2^{-1}$ and $\boldsymbol{M}_{c13}^{-1}$. Equations (5.26) and (5.29) establish the functions that will be linearized and used in a least-squares fit to estimate the calibration parameters.

5.2.2. Nonlinear Least Squares

The observation equations derived in Section 5.2.1 are nonlinear functions $\boldsymbol{f}(\boldsymbol{x})$ of the calibration parameters $\boldsymbol{x}$, i.e.

$$\boldsymbol{y} = \boldsymbol{f}(\boldsymbol{x}), \tag{5.30}$$

where $\boldsymbol{y}$ is the observation vector. For a least-squares fit, the nonlinear equations have to be linearized via Taylor series expansion by truncating the higher order terms:

$$\boldsymbol{y} = \boldsymbol{f}(\boldsymbol{x}_0) + \left.\frac{\partial\boldsymbol{f}(\boldsymbol{x})}{\partial\boldsymbol{x}}\right|_{\boldsymbol{x}=\boldsymbol{x}_0}\Delta\boldsymbol{x} + O(\Delta\boldsymbol{x}^2), \tag{5.31}$$

where $\boldsymbol{x}_0$ is an approximation for the parameters and $\Delta\boldsymbol{x} = \boldsymbol{x} - \boldsymbol{x}_0$. By introducing the Jacobian/Design matrix as

$$J = \left.\frac{\partial\boldsymbol{f}(\boldsymbol{x})}{\partial\boldsymbol{x}}\right|_{\boldsymbol{x}=\boldsymbol{x}_0} \tag{5.32}$$

and the reduced observation vector

$$\Delta\boldsymbol{y} = \boldsymbol{y} - \boldsymbol{f}(\boldsymbol{x}_0), \tag{5.33}$$

The least-squares solution gives the parameter update

$$\Delta\hat{\boldsymbol{x}} = (\boldsymbol{J}^T\Sigma_{\boldsymbol{y}}^{-1}\boldsymbol{J}^T)\boldsymbol{J}^T\Sigma_{\boldsymbol{y}}^{-1}\Delta\boldsymbol{y}, \tag{5.34}$$

where $\Sigma_{\boldsymbol{y}}$ is the noise covariance matrix of the observation vector. The parameters are obtained by adding the parameter update to the approximate parameters:

$$\hat{\boldsymbol{x}} = \boldsymbol{x}_0 + \Delta\hat{\boldsymbol{x}}. \tag{5.35}$$

The approximation can be improved by setting $\boldsymbol{x}_0$ = $\hat{\boldsymbol{x}}_0$ and reiterating the linearization.

Decorrelating Observation Noise

The noise in the observation vector holding accelerometer data is frequency-dependent (coloured noise). Since the accelerometer samples at a uniform rate, the noise covariance matrix $\Sigma_{\boldsymbol{y}}$ holds the auto-covariance function of the noise having a Toeplitz matrix structure. This means the noise at different samples is related, and the relation only depends on the time difference between the samples. This holds only under the assumption that the noise analysed is stationary (Siemes, 2012).

With such a structure, decorrelation filters can be set up to account for the coloured noise. Suppose $A(f)$ is a one-sided amplitude spectral density of the noise. The decorrelation filter is set up sampling the spectral density at normalized frequencies $f_k = \frac{k-1}{2K}$ for $k \in [0, K-1]$ where K is an odd integer, and taking the reciprocals, except for the first element corresponding to $A(f_0)$, which is set to zero:

$$\boldsymbol{u} = \begin{bmatrix} 0 \\ A(f_1)^{-1} \\ . \\ . \\ A(f_{K/2+1})^{-1} \end{bmatrix}. \tag{5.36}$$

An odd sampling will help to make the filter symmetric about the middle sample in the time domain. Setting the first element to zero ensures that the output of the correlation filter has zero mean, avoiding any negative impact on the accelerometer bias. The impulse response of the correlation filter is obtained by taking the inverse FFT transform

$$\boldsymbol{v} = IFFT(\boldsymbol{u}). \tag{5.37}$$

Rearranging $\boldsymbol{v}$ as

$$\boldsymbol{v} = \begin{bmatrix} v_{ceil(K/2)} \\ . \\ . \\ v_{K-1} \\ v_0 \\ . \\ . \\ v_{ceil(K/2)-1} \end{bmatrix} \tag{5.38}$$

makes the impulse response a symmetric filter. Now the filter can be convolved (*) with the observation vector $\boldsymbol{y}$ and the columns of design matrix $\boldsymbol{J}$, i.e.

$$\Delta\bar{\boldsymbol{y}} = \boldsymbol{w(t)} * \Delta\boldsymbol{y}, \qquad \bar{\boldsymbol{J}} = \boldsymbol{w(t)} * \boldsymbol{J}, \tag{5.39}$$

resulting in the following decorrelated, linear system of equations

$$\Delta\bar{\boldsymbol{y}} = \bar{\boldsymbol{J}}\Delta\boldsymbol{x}. \tag{5.40}$$

For decorrelated observation equations, ordinary least squares fit can be applied to obtain the parameter update

$$\Delta\hat{\boldsymbol{x}} = (\bar{\boldsymbol{J}}^T\bar{\boldsymbol{J}})\bar{\boldsymbol{J}}^T\Delta\bar{\boldsymbol{y}}. \tag{5.41}$$

Since the convolution's first and last K elements are affected by edge effects, they are trimmed away, equivalent to ignoring those observations when calculating the parameter update. However, the decorrelation filter must be initialised for the first least squares operation. Since random noise dominates at high frequencies and systematic and model errors are at low frequencies, a bandpass filter with a passband of $0.1\,\mathrm{mHz}$ to $100\,\mathrm{mHz}$ is implemented. After the first operation, the correlation filters are constructed as detailed in Algorithm 2.

Algorithm 2 Realization of the decorrelation filter

```
1: Define a one-sided amplitude spectral density $A(f)$ for $f_k = \frac{k-1}{2K}$ for $k \in [0, K]$ where K is an odd integer
2: Take the reciprocal except the first element $\boldsymbol{u} = \begin{bmatrix} 0 \\ A(f_1)^{-1} \\ . \\ . \\ A(f_{K/2+1})^{-1} \end{bmatrix}$
3: Perform Inverse Discrete Fourier Transform (IDFT) on $\boldsymbol{u}$ to get the time domain impulse response $\boldsymbol{v} = IFFT(\boldsymbol{u})$
4: Rearrange to make it a symmetric decorrelation filter $\boldsymbol{w} = \begin{bmatrix} v_{ceil(K/2)} \\ . \\ . \\ v_{K-1} \\ v_0 \\ . \\ . \\ v_{ceil(K/2)-1} \end{bmatrix}$
```

5.2.3. Linearizing the Observation Equations

To linearize the nonlinear Equations (5.26) and (5.29), the partials w.r.t. all input parameters must be derived to construct the design matrix.

Differential Mode

For convenience, arrange $\boldsymbol{f}_d$ in Equation 5.26 such that each row of observation equations contain x,y and z-components of $\boldsymbol{f}_d$ for a given epoch and define $\boldsymbol{G}_n = -(\boldsymbol{V}_n - \boldsymbol{\Omega}_n^2 - \dot{\boldsymbol{\Omega}}_n)$:

$$\boldsymbol{F}_d = \begin{bmatrix} \boldsymbol{f}_{d,1}^T \\ . \\ . \\ . \\ \boldsymbol{f}_{d,N}^T \end{bmatrix} = \begin{bmatrix} \boldsymbol{b}_{d13}^T \\ . \\ . \\ . \\ \boldsymbol{b}_{d13}^T \end{bmatrix} + \begin{bmatrix} (\boldsymbol{a}_{d13,1}^{np} + \boldsymbol{G}_1\delta\boldsymbol{r}_{d13})^T(\boldsymbol{H}_{c13} + \delta\delta\boldsymbol{M}_{c13})^T \\ . \\ . \\ . \\ (\boldsymbol{a}_{d13,N}^{np} + \boldsymbol{G}_N\delta\boldsymbol{r}_{d13})^T(\boldsymbol{H}_{c13} + \delta\delta\boldsymbol{M}_{c13})^T \end{bmatrix} + ... \tag{5.42}$$

Refer to Appendix A.2 to construct and isolate the parameter vector from a product of matrices and Appendix B.1 to construct the partials of the differential mode observations w.r.t. $\delta \boldsymbol{r}_{d13}$ and $\delta \boldsymbol{r}_{c13}$.

The partials for the design matrix $\boldsymbol{J}$ are obtained by vectorising the matrices with operator *vec* and applying the Kronecker product ($\otimes$) as explained in Appendix A.2. The operator col($\boldsymbol{A}$, n) and row($\boldsymbol{A}$) return the *n*-th column and row of a matrix $\boldsymbol{A}$, respectively. The final form of the partials is as follows:

$$\frac{\partial \text{vec}(\boldsymbol{F}_d)}{\partial \text{vec}(\delta\delta \boldsymbol{M}_{c13}^T)} = \boldsymbol{I}_{3x3} \otimes \begin{bmatrix} \cdot \\ \cdot \\ (\boldsymbol{a}_{d13,n}^{np} + \boldsymbol{G}_n \delta \boldsymbol{r}_{d13})^T \\ \cdot \\ \cdot \end{bmatrix}, \tag{5.43}$$

$$\frac{\partial \text{vec}(\boldsymbol{F}_d)}{\partial \text{vec}(\delta\delta \boldsymbol{M}_{d13}^T)} = \boldsymbol{I}_{3x3} \otimes \begin{bmatrix} \cdot \\ \cdot \\ (\boldsymbol{a}_{c13,n}^{np} + \boldsymbol{G}_n \delta \boldsymbol{r}_{c13})^T \\ \cdot \\ \cdot \end{bmatrix}, \tag{5.44}$$

$$\frac{\partial \text{vec}(\boldsymbol{F}_d)}{\partial \text{vec}(\boldsymbol{K}_1^T)} = \frac{1}{2} \boldsymbol{I}_{3x3} \otimes \begin{bmatrix} \cdot \\ \cdot \\ ((\boldsymbol{a}_{1,n}^{np} + \boldsymbol{G}_n \delta \boldsymbol{r}_1)^2)^T \\ \cdot \\ \cdot \end{bmatrix}, \tag{5.45}$$

$$\frac{\partial \text{vec}(\boldsymbol{F}_d)}{\partial \text{vec}(\boldsymbol{K}_3^T)} = -\frac{1}{2} \boldsymbol{I}_{3x3} \otimes \begin{bmatrix} \cdot \\ \cdot \\ ((\boldsymbol{a}_{3,n}^{np} + \boldsymbol{G}_n \delta \boldsymbol{r}_3)^2)^T \\ \cdot \\ \cdot \end{bmatrix}, \tag{5.46}$$

$$\frac{\partial \text{vec}(\boldsymbol{F}_d)}{\partial \text{vec}(\boldsymbol{W}_{d13}^T)} = \boldsymbol{I}_{3x3} \otimes \begin{bmatrix} \cdot \\ \cdot \\ \dot{\boldsymbol{\omega}}_n^T \\ \cdot \\ \cdot \end{bmatrix}, \tag{5.47}$$

$$
\begin{aligned}
\frac{\partial \mathrm{vec}(\boldsymbol{F}_d)}{\partial(\delta \boldsymbol{r}_{d13})} = &\begin{bmatrix} \vdots \\ \mathrm{row}(\boldsymbol{H}_{c13},1)\boldsymbol{G}_n \\ \vdots \\ \mathrm{row}(\boldsymbol{H}_{c13},2)\boldsymbol{G}_n \\ \vdots \\ \mathrm{row}(\boldsymbol{H}_{c13},3)\boldsymbol{G}_n \\ \vdots \end{bmatrix} + \begin{bmatrix} \vdots \\ (\boldsymbol{a}^{np}_{1x,n} + \mathrm{row}(\boldsymbol{G}_n,1)\delta\boldsymbol{r}_1)^2 K_{1x}\mathrm{row}(\boldsymbol{G}_n,1) \\ \vdots \\ (\boldsymbol{a}^{np}_{1y,n} + \mathrm{row}(\boldsymbol{G}_n,2)\delta\boldsymbol{r}_1)^2 K_{1y}\mathrm{row}(\boldsymbol{G}_n,2) \\ \vdots \\ (\boldsymbol{a}^{np}_{1z,n} + \mathrm{row}(\boldsymbol{G}_n,3)\delta\boldsymbol{r}_1)^2 K_{1z}\mathrm{row}(\boldsymbol{G}_n,3) \\ \vdots \end{bmatrix} \\
&+ \begin{bmatrix} \vdots \\ (\boldsymbol{a}^{np}_{3x,n} + \mathrm{row}(\boldsymbol{G}_n,1)\delta\boldsymbol{r}_3)^2 K_{3x}\mathrm{row}(\boldsymbol{G}_n,1) \\ \vdots \\ (\boldsymbol{a}^{np}_{3y,n} + \mathrm{row}(\boldsymbol{G}_n,2)\delta\boldsymbol{r}_3)^2 K_{3y}\mathrm{row}(\boldsymbol{G}_n,2) \\ \vdots \\ (\boldsymbol{a}^{np}_{3z,n} + \mathrm{row}(\boldsymbol{G}_n,3)\delta\boldsymbol{r}_3)^2 K_{3z}\mathrm{row}(\boldsymbol{G}_n,3) \\ \vdots \end{bmatrix},
\end{aligned} \tag{5.48}
$$

$$
\begin{aligned}
\frac{\partial \mathrm{vec}(\boldsymbol{F}_d)}{\partial(\delta \boldsymbol{r}_{c13})} = &\begin{bmatrix} \vdots \\ \mathrm{row}(\boldsymbol{H}_{d13},1)\boldsymbol{G}_n \\ \vdots \\ \mathrm{row}(\boldsymbol{H}_{d13},2)\boldsymbol{G}_n \\ \vdots \\ \mathrm{row}(\boldsymbol{H}_{d13},3)\boldsymbol{G}_n \\ \vdots \end{bmatrix} + \begin{bmatrix} \vdots \\ (\boldsymbol{a}^{np}_{1x,n} + \mathrm{row}(\boldsymbol{G}_n,1)\delta\boldsymbol{r}_1)^2 K_{1x}\mathrm{row}(\boldsymbol{G}_n,1) \\ \vdots \\ (\boldsymbol{a}^{np}_{1y,n} + \mathrm{row}(\boldsymbol{G}_n,2)\delta\boldsymbol{r}_1)^2 K_{1y}\mathrm{row}(\boldsymbol{G}_n,2) \\ \vdots \\ (\boldsymbol{a}^{np}_{1z,n} + \mathrm{row}(\boldsymbol{G}_n,3)\delta\boldsymbol{r}_1)^2 K_{1z}\mathrm{row}(\boldsymbol{G}_n,3) \\ \vdots \end{bmatrix} \\
&- \begin{bmatrix} \vdots \\ (\boldsymbol{a}^{np}_{3x,n} + \mathrm{row}(\boldsymbol{G}_n,1)\delta\boldsymbol{r}_3)^2 K_{3x}\mathrm{row}(\boldsymbol{G}_n,1) \\ \vdots \\ (\boldsymbol{a}^{np}_{3y,n} + \mathrm{row}(\boldsymbol{G}_n,2)\delta\boldsymbol{r}_3)^2 K_{3y}\mathrm{row}(\boldsymbol{G}_n,2) \\ \vdots \\ (\boldsymbol{a}^{np}_{3z,n} + \mathrm{row}(\boldsymbol{G}_n,3)\delta\boldsymbol{r}_3)^2 K_{3z}\mathrm{row}(\boldsymbol{G}_n,3) \\ \vdots \end{bmatrix}.
\end{aligned} \tag{5.49}
$$

Common Mode

Again arrange $\boldsymbol{f}_c$ such that each row of observation equations contain x,y and z-components of $\boldsymbol{f}_c$ for a given epoch and define $\boldsymbol{G}_n = -(\boldsymbol{V}_n - \boldsymbol{\Omega}_n^2 - \dot{\boldsymbol{\Omega}}_n)$. First, the partials related to $\boldsymbol{a}_2$ are analysed:

$$\boldsymbol{F}_c = \begin{bmatrix} \boldsymbol{f}_{c,1}^T \\ \cdot \\ \cdot \\ \boldsymbol{f}_{c,N}^T \end{bmatrix} = ... - \begin{bmatrix} \cdot \\ \cdot \\ (\boldsymbol{a}_{2,n}^{meas} - \boldsymbol{K}_2(\boldsymbol{a}_{2,n}^{np} + \boldsymbol{G}_n \delta \boldsymbol{r}_2)^2 - \boldsymbol{W}_2 \dot{\boldsymbol{\omega}})^T \\ \cdot \\ \cdot \end{bmatrix} (\boldsymbol{H}_2^{-1} - \boldsymbol{H}_2^{-1} \delta\delta \boldsymbol{M}_2 \boldsymbol{H}_2^{-1}) + ... \tag{5.50}$$

The following partials are

$$\frac{\partial \text{vec}(\boldsymbol{F}_c)}{\partial \text{vec}(\delta\delta \boldsymbol{M}_2^T)} = \boldsymbol{H}_2^{-1} \otimes \begin{bmatrix} \cdot \\ \cdot \\ \left((\boldsymbol{a}_{2,n}^{meas} - \boldsymbol{K}_2(\boldsymbol{a}_{2,n}^{np} + \boldsymbol{G}_n \delta \boldsymbol{r}_2)^2 - \boldsymbol{W}_2 \dot{\boldsymbol{\omega}})^T\right) \boldsymbol{H}_2^{-T} \\ \cdot \\ \cdot \end{bmatrix}, \tag{5.51}$$

$$\frac{\partial \text{vec}(\boldsymbol{F}_c)}{\partial \text{vec}(\boldsymbol{K}_2^T)} = \boldsymbol{H}_2^{-1} \otimes \begin{bmatrix} \cdot \\ \cdot \\ \left((\boldsymbol{a}_{2,n}^{np} + \boldsymbol{G}_n \delta \boldsymbol{r}_2)^2\right)^T \\ \cdot \\ \cdot \end{bmatrix}, \tag{5.52}$$

$$\frac{\partial \text{vec}(\boldsymbol{F}_c)}{\partial \text{vec}(\boldsymbol{W}_2^T)} = \boldsymbol{H}_2^{-1} \otimes \begin{bmatrix} \cdot \\ \cdot \\ \dot{\boldsymbol{\omega}}_n^T \\ \cdot \\ \cdot \end{bmatrix}. \tag{5.53}$$

Next, the terms related to $\boldsymbol{a}_{c13}$ are analysed:

$$\begin{aligned} \boldsymbol{F}_c = & \begin{bmatrix} \cdot \\ \cdot \\ (\boldsymbol{a}_{c13,n}^{meas} - \boldsymbol{M}_{d13}(\boldsymbol{a}_{d13,n}^{np} + \boldsymbol{G}_n \delta \boldsymbol{r}_{d13}) - \boldsymbol{W}_{c13} \dot{\boldsymbol{\omega}}_n)^T \\ \cdot \\ \cdot \end{bmatrix} (\boldsymbol{H}_{c13}^{-T} - \boldsymbol{H}_{c13}^{-T} \delta\delta \boldsymbol{M}_{c13}^T \delta\delta \boldsymbol{H}_{c13}^{-T}) \\ & - \frac{1}{2} \begin{bmatrix} \cdot \\ \cdot \\ (\boldsymbol{K}_1(\boldsymbol{a}_{1,n}^{np} + \boldsymbol{G}_n \delta \boldsymbol{r}_1)^2 + \boldsymbol{K}_3(\boldsymbol{a}_{3,n}^{np} + \boldsymbol{G}_n \delta \boldsymbol{r}_3)^2)^T \\ \cdot \\ \cdot \end{bmatrix} (\boldsymbol{H}_{c13}^{-T} - \boldsymbol{H}_{c13}^{-T} \delta\delta \boldsymbol{M}_{c13}^T \delta\delta \boldsymbol{H}_{c13}^{-T}). \end{aligned} \tag{5.54}$$

The partials are

$$\begin{aligned}\frac{\partial \text{vec}(\boldsymbol{F}_c)}{\partial \text{vec}(\delta\delta \boldsymbol{M}_{c13}^T)} &= -\boldsymbol{H}_{c13}^{-1} \otimes \left(\begin{bmatrix} \vdots \\ (\boldsymbol{a}_{c13,n}^{meas} - \boldsymbol{M}_{d13}(\boldsymbol{a}_{d13,n}^{np} + \boldsymbol{G}_n \delta \boldsymbol{r}_{d13}) - \boldsymbol{W}_{c13}\dot{\boldsymbol{\omega}}_n)^T \\ \vdots \end{bmatrix} \boldsymbol{H}_{c13}^{-T} \right) \\ &+ \frac{1}{2}\boldsymbol{H}_{c13}^{-1} \otimes \left(\begin{bmatrix} \vdots \\ (\boldsymbol{K}_1(\boldsymbol{a}_{1,n}^{np} + \boldsymbol{G}_n \delta \boldsymbol{r}_1)^2 + \boldsymbol{K}_3(\boldsymbol{a}_{3,n}^{np} + \boldsymbol{G}_n \delta \boldsymbol{r}_3)^2)^T \\ \vdots \end{bmatrix} \boldsymbol{H}_{c13}^{-T} \right),\end{aligned} \tag{5.55}$$

$$\frac{\partial \text{vec}(\boldsymbol{F}_c)}{\partial \text{vec}(\delta\delta \boldsymbol{M}_{d13}^T)} = -\boldsymbol{H}_{c13}^{-1} \otimes \left(\begin{bmatrix} \vdots \\ (\boldsymbol{a}_{d13,n}^{np} + \boldsymbol{G}_n \delta \boldsymbol{r}_{d13})^T \\ \vdots \end{bmatrix} \right), \tag{5.56}$$

$$\frac{\partial \text{vec}(\boldsymbol{F}_c)}{\partial \text{vec}(\boldsymbol{K}_1^T)} = -\frac{1}{2}\boldsymbol{H}_{c13}^{-1} \otimes \left(\begin{bmatrix} \vdots \\ ((\boldsymbol{a}_{1,n}^{np} + \boldsymbol{G}_n \delta \boldsymbol{r}_1)^2)^T \\ \vdots \end{bmatrix} \right), \tag{5.57}$$

$$\frac{\partial \text{vec}(\boldsymbol{F}_c)}{\partial \text{vec}(\boldsymbol{K}_3^T)} = -\frac{1}{2}\boldsymbol{H}_{c13}^{-1} \otimes \left(\begin{bmatrix} \vdots \\ ((\boldsymbol{a}_{3,n}^{np} + \boldsymbol{G}_n \delta \boldsymbol{r}_3)^2)^T \\ \vdots \end{bmatrix} \right), \tag{5.58}$$

$$\frac{\partial \text{vec}(\boldsymbol{F}_c)}{\partial \text{vec}(\boldsymbol{W}_{c13}^T)} = -\boldsymbol{H}_{c13}^{-1} \otimes \left(\begin{bmatrix} \vdots \\ \dot{\boldsymbol{\omega}}^T \\ \vdots \end{bmatrix} \right). \tag{5.59}$$

Refer to Appendix B.2 for a detailed derivation of common mode observation partials w.r.t. $\delta \boldsymbol{r}_{d13}$ and $\delta \boldsymbol{r}_{c13}$.

$$
\begin{aligned}
&\frac{\partial \text{vec}(\boldsymbol{F}_c)}{\partial(\delta \boldsymbol{r}_{d13})} = \\
&-\begin{bmatrix}
\vdots & & \vdots \\
(\boldsymbol{a}_{1,n}^{np} + \boldsymbol{G}_n \delta \boldsymbol{r}_1)^T \text{col}(\boldsymbol{G}_n, 1) \circ \text{col}(\boldsymbol{K}_1 \boldsymbol{H}_{c13}^{-T}, 1) & \dots & (\boldsymbol{a}_{1,n}^{np} + \boldsymbol{G}_n \delta \boldsymbol{r}_1)^T \text{col}(\boldsymbol{G}_n, 3) \circ \text{col}(\boldsymbol{K}_1 \boldsymbol{H}_{c13}^{-T}, 1) \\
\vdots & & \vdots \\
(\boldsymbol{a}_{1,n}^{np} + \boldsymbol{G}_n \delta \boldsymbol{r}_1)^T \text{col}(\boldsymbol{G}_n, 1) \circ \text{col}(\boldsymbol{K}_1 \boldsymbol{H}_{c13}^{-T}, 2) & \dots & (\boldsymbol{a}_{1,n}^{np} + \boldsymbol{G}_n \delta \boldsymbol{r}_1)^T \text{col}(\boldsymbol{G}_n, 3) \circ \text{col}(\boldsymbol{K}_1 \boldsymbol{H}_{c13}^{-T}, 2) \\
\vdots & & \vdots \\
(\boldsymbol{a}_{1,n}^{np} + \boldsymbol{G}_n \delta \boldsymbol{r}_1)^T \text{col}(\boldsymbol{G}_n, 1) \circ \text{col}(\boldsymbol{K}_1 \boldsymbol{H}_{c13}^{-T}, 3) & \dots & (\boldsymbol{a}_{1,n}^{np} + \boldsymbol{G}_n \delta \boldsymbol{r}_1)^T \text{col}(\boldsymbol{G}_n, 3) \circ \text{col}(\boldsymbol{K}_1 \boldsymbol{H}_{c13}^{-T}, 3) \\
\vdots & & \vdots
\end{bmatrix} \\
&+\begin{bmatrix}
\vdots & & \vdots \\
(\boldsymbol{a}_{3,n}^{np} + \boldsymbol{G}_n \delta \boldsymbol{r}_3)^T \text{col}(\boldsymbol{G}_n, 1) \circ \text{col}(\boldsymbol{K}_3 \boldsymbol{H}_{c13}^{-T}, 1) & \dots & (\boldsymbol{a}_{3,n}^{np} + \boldsymbol{G}_n \delta \boldsymbol{r}_3)^T \text{col}(\boldsymbol{G}_n, 3) \circ \text{col}(\boldsymbol{K}_3 \boldsymbol{H}_{c13}^{-T}, 1) \\
\vdots & & \vdots \\
(\boldsymbol{a}_{3,n}^{np} + \boldsymbol{G}_n \delta \boldsymbol{r}_3)^T \text{col}(\boldsymbol{G}_n, 1) \circ \text{col}(\boldsymbol{K}_3 \boldsymbol{H}_{c13}^{-T}, 2) & \dots & (\boldsymbol{a}_{3,n}^{np} + \boldsymbol{G}_n \delta \boldsymbol{r}_3)^T \text{col}(\boldsymbol{G}_n, 3) \circ \text{col}(\boldsymbol{K}_3 \boldsymbol{H}_{c13}^{-T}, 2) \\
\vdots & & \vdots \\
(\boldsymbol{a}_{3,n}^{np} + \boldsymbol{G}_n \delta \boldsymbol{r}_3)^T \text{col}(\boldsymbol{G}_n, 1) \circ \text{col}(\boldsymbol{K}_3 \boldsymbol{H}_{c13}^{-T}, 3) & \dots & (\boldsymbol{a}_{3,n}^{np} + \boldsymbol{G}_n \delta \boldsymbol{r}_3)^T \text{col}(\boldsymbol{G}_n, 3) \circ \text{col}(\boldsymbol{K}_3 \boldsymbol{H}_{c13}^{-T}, 3) \\
\vdots & & \vdots
\end{bmatrix} \\
&-\begin{bmatrix}
\vdots \\
\text{row}(\boldsymbol{H}_{c13}^{-1} \boldsymbol{M}_{d13} \boldsymbol{G}_n, 1) \\
\vdots \\
\text{row}(\boldsymbol{H}_{c13}^{-1} \boldsymbol{M}_{d13} \boldsymbol{G}_n, 2) \\
\vdots \\
\text{row}(\boldsymbol{H}_{c13}^{-1} \boldsymbol{M}_{d13} \boldsymbol{G}_n, 1) \\
\vdots
\end{bmatrix},
\end{aligned}
\tag{5.60}
$$

$$\frac{\partial \text{vec}(\boldsymbol{F}_c)}{\partial(\delta \boldsymbol{r}_{c13})} =$$

$$- \begin{bmatrix} \vdots & & \vdots \\ (\boldsymbol{a}^{np}_{1,n} + \boldsymbol{G}_n \delta \boldsymbol{r}_1)^T \text{col}(\boldsymbol{G}_n,1) \circ \text{col}(\boldsymbol{K}_1 \boldsymbol{H}_{c13}^{-T},1) & \dots & (\boldsymbol{a}^{np}_{1,n} + \boldsymbol{G}_n \delta \boldsymbol{r}_1)^T \text{col}(\boldsymbol{G}_n,3) \circ \text{col}(\boldsymbol{K}_1 \boldsymbol{H}_{c13}^{-T},1) \\ \vdots & & \vdots \\ (\boldsymbol{a}^{np}_{1,n} + \boldsymbol{G}_n \delta \boldsymbol{r}_1)^T \text{col}(\boldsymbol{G}_n,1) \circ \text{col}(\boldsymbol{K}_1 \boldsymbol{H}_{c13}^{-T},2) & \dots & (\boldsymbol{a}^{np}_{1,n} + \boldsymbol{G}_n \delta \boldsymbol{r}_1)^T \text{col}(\boldsymbol{G}_n,3) \circ \text{col}(\boldsymbol{K}_1 \boldsymbol{H}_{c13}^{-T},2) \\ \vdots & & \vdots \\ (\boldsymbol{a}^{np}_{1,n} + \boldsymbol{G}_n \delta \boldsymbol{r}_1)^T \text{col}(\boldsymbol{G}_n,1) \circ \text{col}(\boldsymbol{K}_1 \boldsymbol{H}_{c13}^{-T},3) & \dots & (\boldsymbol{a}^{np}_{1,n} + \boldsymbol{G}_n \delta \boldsymbol{r}_1)^T \text{col}(\boldsymbol{G}_n,3) \circ \text{col}(\boldsymbol{K}_1 \boldsymbol{H}_{c13}^{-T},3) \\ \vdots & & \vdots \end{bmatrix}$$

$$- \begin{bmatrix} \vdots & & \vdots \\ (\boldsymbol{a}^{np}_{3,n} + \boldsymbol{G}_n \delta \boldsymbol{r}_3)^T \text{col}(\boldsymbol{G}_n,1) \circ \text{col}(\boldsymbol{K}_3 \boldsymbol{H}_{c13}^{-T},1) & \dots & (\boldsymbol{a}^{np}_{3,n} + \boldsymbol{G}_n \delta \boldsymbol{r}_3)^T \text{col}(\boldsymbol{G}_n,3) \circ \text{col}(\boldsymbol{K}_3 \boldsymbol{H}_{c13}^{-T},1) \\ \vdots & & \vdots \\ (\boldsymbol{a}^{np}_{3,n} + \boldsymbol{G}_n \delta \boldsymbol{r}_3)^T \text{col}(\boldsymbol{G}_n,1) \circ \text{col}(\boldsymbol{K}_3 \boldsymbol{H}_{c13}^{-T},2) & \dots & (\boldsymbol{a}^{np}_{3,n} + \boldsymbol{G}_n \delta \boldsymbol{r}_3)^T \text{col}(\boldsymbol{G}_n,3) \circ \text{col}(\boldsymbol{K}_3 \boldsymbol{H}_{c13}^{-T},2) \\ \vdots & & \vdots \\ (\boldsymbol{a}^{np}_{3,n} + \boldsymbol{G}_n \delta \boldsymbol{r}_3)^T \text{col}(\boldsymbol{G}_n,1) \circ \text{col}(\boldsymbol{K}_3 \boldsymbol{H}_{c13}^{-T},3) & \dots & (\boldsymbol{a}^{np}_{3,n} + \boldsymbol{G}_n \delta \boldsymbol{r}_3)^T \text{col}(\boldsymbol{G}_n,3) \circ \text{col}(\boldsymbol{K}_3 \boldsymbol{H}_{c13}^{-T},3) \\ \vdots & & \vdots \end{bmatrix} \tag{5.61}$$

$$- \begin{bmatrix} \vdots \\ \text{row}(\boldsymbol{G}_n,1) \\ \vdots \\ \text{row}(\boldsymbol{G}_n,2) \\ \vdots \\ \text{row}(\boldsymbol{G}_n,3) \\ \vdots \end{bmatrix} .$$

5.2.4. Arrangement of Observations and Parameters

With the partials derived w.r.t. each parameter, the observations and parameters can now be arranged to perform the least squares fit. The following arrangement is performed for the observations $\boldsymbol{y}$, approximation of the observations $\boldsymbol{y}_0$ using $\boldsymbol{f}(\boldsymbol{x}_0)$ and the parameters $\boldsymbol{x}$:

$$\boldsymbol{y} = \begin{bmatrix} \boldsymbol{y}_d \\ \boldsymbol{y}_c \end{bmatrix}, \qquad \boldsymbol{y}_0 = \boldsymbol{f} = \begin{bmatrix} \text{vec}(\boldsymbol{F}_d) \\ \text{vec}(\boldsymbol{F}_c) \end{bmatrix}, \tag{5.62}$$

where

$$\boldsymbol{y}_d = \text{vec}\left(\begin{bmatrix} (\boldsymbol{a}^{meas}_{d13,1})^T \\ \vdots \\ (\boldsymbol{a}^{meas}_{d13,N})^T \end{bmatrix} \right), \qquad \boldsymbol{y}_c = \boldsymbol{0}_{3N \times 1} \tag{5.63}$$

and

$$\boldsymbol{x}^{(ext)} = \begin{bmatrix} \text{vec}(\delta\delta\boldsymbol{M}_2^T) \\ \text{vec}(\delta\delta\boldsymbol{M}_{c13}^T) \\ \text{vec}(\delta\delta\boldsymbol{M}_{d13}^T) \\ \text{vec}(\boldsymbol{K}_1) \\ \text{vec}(\boldsymbol{K}_2) \\ \text{vec}(\boldsymbol{K}_3) \\ \text{vec}(\boldsymbol{W}_{d13}) \\ \text{vec}(\boldsymbol{W}_2 - \boldsymbol{W}_{c13}) \\ \boldsymbol{r}_{c13} \\ \boldsymbol{r}_{d13} \end{bmatrix}. \tag{5.64}$$

The parameter vector $\boldsymbol{x}^{(ext)}$ contains all the elements of every matrix, but several elements are zero by definition and thus can be removed. The six off-diagonal elements of the quadratic factor matrices $\boldsymbol{K}_1$, $\boldsymbol{K}_2$, and $\boldsymbol{K}_3$, and the six elements of the matrices $\boldsymbol{W}_{d13}$ and $(\boldsymbol{W}_2 - \boldsymbol{W}_{c13})$ are zero. $\boldsymbol{W}_2$ and $\boldsymbol{W}_{c13}$ cannot be estimated independently, but only their combined effect. Therefore, $\boldsymbol{W}_2$ is, by definition, set to zero. Finally, the parameter r_{d13y} is removed since it cannot be estimated due to the same effect as the scaling accounted by $\boldsymbol{M}_{c13}$. The trimmed parameter vector $\boldsymbol{x}$ can be written as

$$\boldsymbol{x} = \text{select}(\boldsymbol{x}^{(ext)}), \tag{5.65}$$

and apply the same operator to the design matrix $\boldsymbol{J}^{ext}$ acting on its columns:

$$\boldsymbol{J} = \text{select}(\boldsymbol{J}^{(ext)}). \tag{5.66}$$

5.2.5. Estimation Algorithm

Building the system requires the true acceleration at nominal positions $\boldsymbol{a}_i^{np}$ for which the non-gravitational acceleration $\boldsymbol{a}_{ng}$ is required. Since this data is not available when processing real data, it is estimated iteratively.

From Equation 5.4, the calibrated acceleration can be inferred as

$$\boldsymbol{a}_i^{cal} = \boldsymbol{M}_i^{-1}(\boldsymbol{a}_i^{meas} - \boldsymbol{K}_i\boldsymbol{a}_i^2 - \boldsymbol{W}_i\dot{\boldsymbol{\omega}}) \tag{5.67}$$

The above equation requires the knowledge of true acceleration for the quadratic term $\boldsymbol{a}_i^2$. It is estimated by intialising $\boldsymbol{a}_i^2 = (\boldsymbol{a}_i^{meas})^2$ to calculate $\boldsymbol{a}_i^{cal}$ and then iterated to by setting $\boldsymbol{a}_i^2 = (\boldsymbol{a}_i^{cal})^2$. Then, the calibrated acceleration at nominal position $\boldsymbol{a}_i^{cal,np}$ is found by

$$\boldsymbol{a}_i^{cal,np} = \boldsymbol{a}_i^{cal} - \boldsymbol{G}_i\delta\boldsymbol{r}_i \tag{5.68}$$

The lowest-noise estimate for the non-gravitational accelerations is

$$\boldsymbol{a}_{ng}^{rcst} = \frac{1}{3}(\boldsymbol{a}_1^{cal,np} + \boldsymbol{a}_2^{cal,np} + \boldsymbol{a}_3^{cal,np}) \tag{5.69}$$

The final estimation algorithm for the calibration parameters is presented in Algorithm 3.

Algorithm 3 Accelerometer parameters estimation

```
Input Data:
    • Accelerations $\boldsymbol{a}_1^{meas}$, $\boldsymbol{a}_2^{meas}$, and $\boldsymbol{a}_3^{meas}$
    • Angular velocity $\boldsymbol{\omega}$ from the star sensors and/or accelerometer
    • Gravity gradients $\boldsymbol{V}$
    • Iterations P for the stochastic model
    • Iterations Q for calculating the quadratic term of the acceleration
    • Iterations R for linearization
Calculate $\dot{\boldsymbol{\omega}}$ from $\boldsymbol{\omega}$
Initialise the parameter vector $\boldsymbol{x}_0 = \boldsymbol{0}$
for p=0,...,P-1 do                                          ▷ Loop over stochastic model
    Convert $\boldsymbol{x}_0$ to $\boldsymbol{M}_i$, $\boldsymbol{K}_i$, $\boldsymbol{W}_i$, and $\delta\boldsymbol{r}_i$
    Initialise decorrelation filters $w(t)$ as 0.1-100 mHz bandpass filters
    Initialise $\boldsymbol{a}_i^{cal} = \boldsymbol{a}_i^{meas}$
    for q=0,...,Q-1 do                                      ▷ Loop over quadratic term estimation
        Calculate $\boldsymbol{a}_i^{cal} = \boldsymbol{M}_i^{-1}(\boldsymbol{a}_i^{meas} - \boldsymbol{K}_i(\boldsymbol{a}_i^{cal})^2 - \boldsymbol{W}_i\dot{\boldsymbol{\omega}})$
    end for                                                 ▷ End quadratic model loop
    Calculate $\boldsymbol{a}_i^{cal,np} = \boldsymbol{a}_i^{cal} - \boldsymbol{G}_i\delta\boldsymbol{r}_i$
    Calculate $\boldsymbol{a}_{ng}^{rcst} = \frac{1}{3}(\boldsymbol{a}_1^{cal,np} + \boldsymbol{a}_2^{cal,np} + \boldsymbol{a}_3^{cal,np})$
    for r=0,...,R-1 do                                      ▷ Loop over linearization
        Construct $\boldsymbol{y}$ and $\boldsymbol{y}_0$ using Equation 5.62
        Construct $\boldsymbol{J}$ using Equation 5.66
        $\bar{\boldsymbol{y}} = \boldsymbol{w} * \boldsymbol{y}$                                       ▷ Decorrelate
        $\bar{\boldsymbol{y}}_0 = \boldsymbol{w} * \boldsymbol{y}_0$
        $\bar{\boldsymbol{J}} = \boldsymbol{w} * \boldsymbol{J}$
        Trim $\bar{\boldsymbol{y}}$, $\bar{\boldsymbol{y}}_0$, and $\bar{\boldsymbol{J}}$                    ▷ To remove edge effects of convolution
        $\Delta\hat{\boldsymbol{x}} = (\bar{\boldsymbol{J}}^T\bar{\boldsymbol{J}})^{-1}\bar{\boldsymbol{J}}^T(\bar{\boldsymbol{y}} - \bar{\boldsymbol{y}}_0)$
        $\boldsymbol{x}_0 = \boldsymbol{x}_0 + \Delta\hat{\boldsymbol{x}}$
    end for                                                 ▷ End linearization loop
    Reconstruct $\boldsymbol{y}_0$ using Equation 5.62
    Calculate the residuals $\boldsymbol{e} = \boldsymbol{y} - \boldsymbol{y}_0$
    Estimate ASD $A(f)$ from $\boldsymbol{e}$                ▷ Using Welch's method. Generates 6 ASDs
    Update the decorrelation filter $\boldsymbol{w}$ from $A(f)$ using Algorithm 2.
end for                                                     ▷ End stochastic model loop
Convert $\boldsymbol{x}_0$ to $\boldsymbol{M}_i$, $\boldsymbol{K}_i$, $\boldsymbol{W}_i$, and $\delta\boldsymbol{r}_i$
```

6

Verification & Validation

This chapter outlines the steps to verify and validate the tools developed for this thesis. Section 6.1 verifies the reference orbit generation, followed by Section 6.2, where the design matrix and least squares implementation are verified. Finally, the toolbox is validated by estimating parameters from the GOCE satellite.

6.1. Orbit Verification

With a simple point mass orbit, a few simple checks can be performed to verify if the orbit is computed as expected. The x-axis of the trailing satellite labelled NGGM2 in Figure 6.1 points along the LoS vector. Since the LoS is roughly in the along-track direction, the z-axis of the spacecraft roughly points in the nadir direction. Given a separation distance of $220\,\mathrm{km}$, the angle between the $\boldsymbol{r}_2$ and $\boldsymbol{z}_B$ is

$$\theta = \frac{|\boldsymbol{r}_{21}|}{2|\boldsymbol{r}_2|} = \frac{220}{2 \times 6774} = 0.93^\circ \tag{6.1}$$

The estimated angle for vectors pointing in opposite directions would be 179.07°. Figure 6.2a shows the evolution of θ between $\boldsymbol{r}_2$ and $\boldsymbol{x}_B$. The angle stays constant throughout the orbit with a value of 179.07° as calculated, thus verifying that the rotation model imposed on the trailing satellite to point its body-fixed x-axis along the LoS is working as intended.

Another simple check is to verify the angular velocity about the y-axis. Since it is a point mass circular orbit, the expected angular velocity about the y-axis of the body frame can be written as

$$\omega_y = \sqrt{\frac{\mu}{(R_E + h)^3}} = \sqrt{\frac{398600}{(6378 + 396)^3}} = 1.13\ \mathrm{mrad\,s^{-1}} \tag{6.2}$$

where R_E is the radius of the Earth and h the altitude of the satellite pair. The sign of the ω_y should be negative for NGGM2 as it rotates clockwise about the y-axis to follow the LoS vector. The average angular rate about the y-axis of the body frame from the simulation is $\omega_y = -1.134\ \mathrm{mrad\,s^{-1}}$ as shown by the orange line in Figure 6.2b. The angular velocities about the x- and z-axis are zero as the attitude is fixed. Thus, the magnitude and direction of angular velocities are as expected.

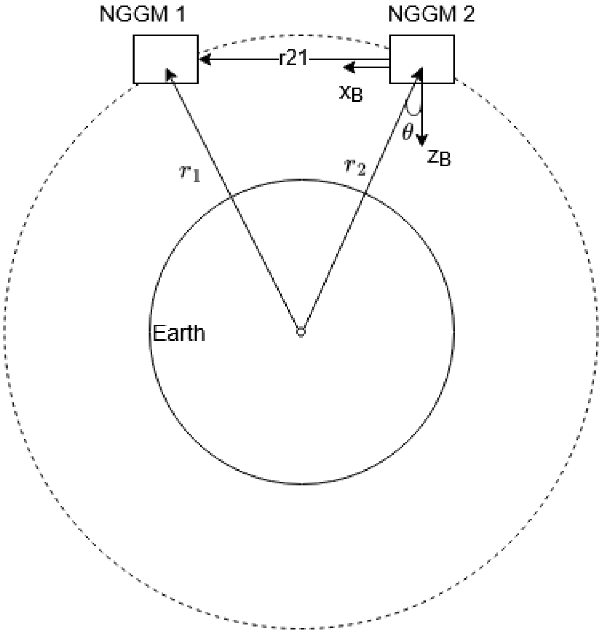

Figure 6.1: Orientation of body axes of NGGM 2

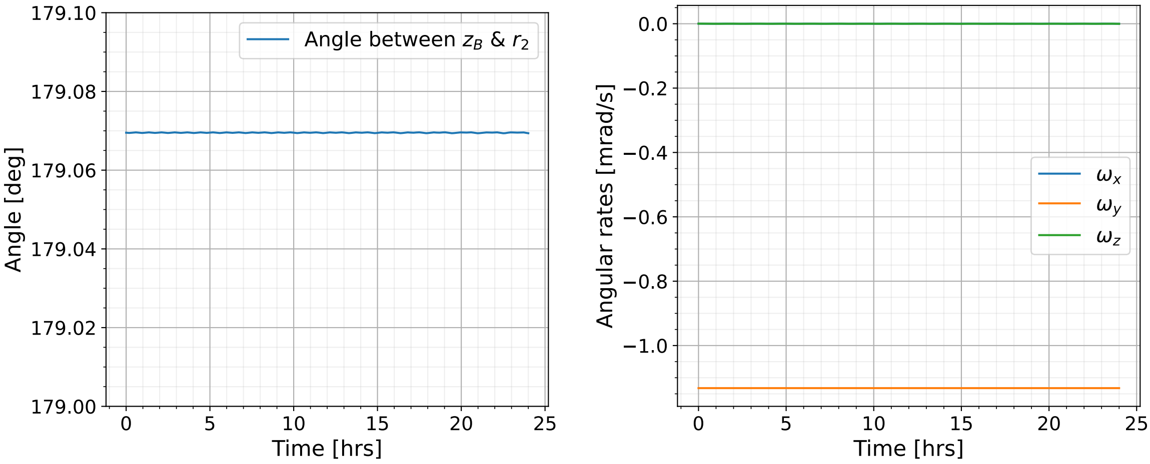

(a) **(b)**

Figure 6.2: a) The angle between the z-axis and the vector connecting NGGM2 with the Earth's centre. b) Angular rates about x-, y- and z-axis of satellite's body-fixed frame.

Finally, the altitude of the pair and the inter-satellite distance between the pair are given Figures 6.3a and 6.3b, respectively. The altitude stays constant at $396\,\mathrm{km}$ and the separation at $220\,\mathrm{km}$ throughout the simulation as it was defined, confirming that the orbit simulation is setup and works as expected.

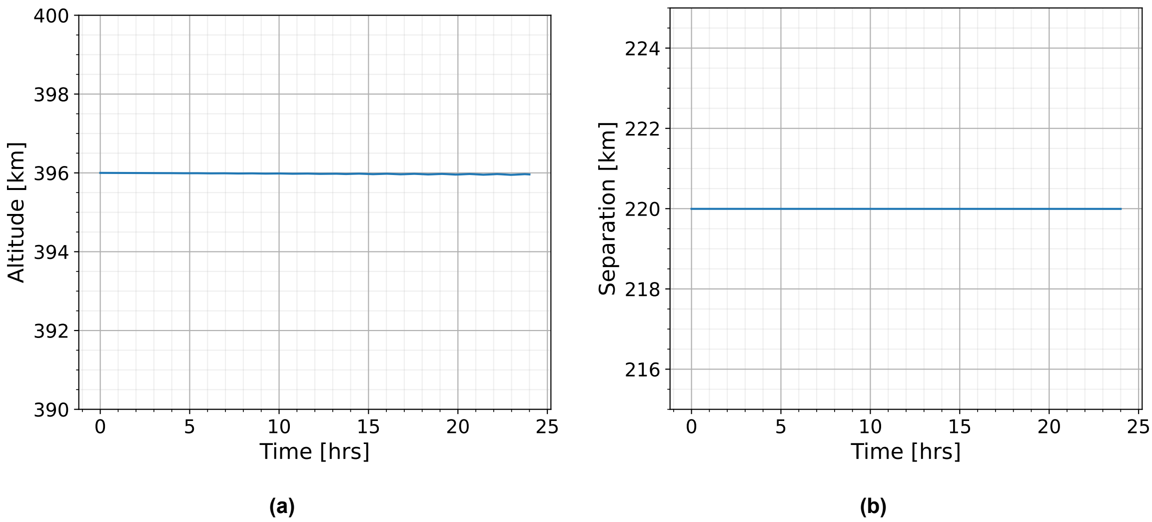

Figure 6.3: a) Altitude as a function of time. b) Inter-satellite separation as a function of time

6.2. Calibration Verification & Validation

The calibration procedure involves two main steps: building the design matrix from observation equations for linearization and performing the least squares adjustment.

To verify if these are implemented correctly, three checks will be performed:

1. Check if the design matrix is correctly constructed by comparing it to the numerical derivative
2. Analyse the error in estimated parameters without noise in observations. This verifies if the least squares algorithm is correctly set up.
3. Analyse the error in estimated parameters with noise in observations. This checks if the decorrelation filters are working.

Here, the verification and validation of Layout 3 on the y-axis are presented. The same procedure follows for Layouts 2 and 4 and/or x- and z-axis placement (not shown).

6.2.1. Design Matrix

Consider a non-linear observation equations system stated as

$$\boldsymbol{y} = \boldsymbol{f}(\boldsymbol{x}) \tag{6.3}$$

Using the Taylor series expansion up to the first order, the function can be estimated for each parameter in $\boldsymbol{x}$ as

$$\boldsymbol{f}(x_i) = \boldsymbol{f}(x_{i,0}) + \text{col}(\boldsymbol{J}, i)|_{x_i=x_{i,0}}\Delta x_i + O(\Delta x_i^2). \tag{6.4}$$

By rearranging the equation, the error between the numerical derivative and the analytical derivative estimated by the design matrix column for each parameter in $\boldsymbol{x}$ is expressed as

$$\boldsymbol{e}_i = \frac{\boldsymbol{f}(x_i) - \boldsymbol{f}(x_{i,0})}{\Delta x_i} - \text{col}(\boldsymbol{J}, i)|_{x_i=x_{i,0}} \approx O(\Delta x_i). \tag{6.5}$$

The error is of order Δx_i if Equation (6.3) is not linear in relationship, where $\Delta x_i = x_i - x_{i,0}$.

For Layout 2, there are 47 parameters in $\boldsymbol{x}$. By computing a ratio between the error obtained by selecting a random vector $\boldsymbol{x}_0$ and varying each parameter by a small value dx and $dx/10$, the ratio should be of a value of 10. Since the error vector is a function of time, the RMS is calculated to obtain a single value for ratio calculation. This allows us to verify if each design matrix column is implemented correctly.

Figures 6.4 and 6.5 showcases the ratio between the RMS error for each parameter with a variation of dx and $dx/10$ for differential and common mode, respectively. From Equation 5.25, the relationship between the observations and parameters for differential mode is linear except the $\delta\boldsymbol{r}$ parameters. In Figure 6.4, the $\delta\boldsymbol{r}$ seen from index 42 onwards all have a ratio of 10. $\boldsymbol{M}_2$ has no points as the differential mode is not a function of it. For other parameters, the points seen arise due to numerical errors in computation.

Whereas for common mode acceleration, Equation 5.28 tells us that the observation vector has a non-linear relationship with the parameters of matrices $\boldsymbol{M}_2$, $\boldsymbol{M}_{c13}$, and $\delta\boldsymbol{r}$. In Figure 6.5, for all, the error ratio has an expected value of around 10. Interestingly, the parameters of $\delta\boldsymbol{r}$ are stable and are exactly 10, whereas parameters of $\boldsymbol{M}_2$ and $\boldsymbol{M}_{c13}$, fluctuate close to the value of 10. $\delta\boldsymbol{r}$ has a square relationship; therefore the error is exactly predicted by $\Delta\boldsymbol{x}$ when Taylor expanded. However, matrices $\boldsymbol{M}_2$ and $\boldsymbol{M}_{c13}$ have an inverse relationship with the observation vector such that the higher order terms of $\Delta\boldsymbol{x}$ will have an effect, too, leading to minor fluctuations. Parameters of $\boldsymbol{M}_{d13}$, $\boldsymbol{K}$, and $\boldsymbol{W}$ are linearly related, and as discussed, the error seen in the figure are purely numerical errors.

Thus, the design matrix for both differential and common mode is implemented correctly.

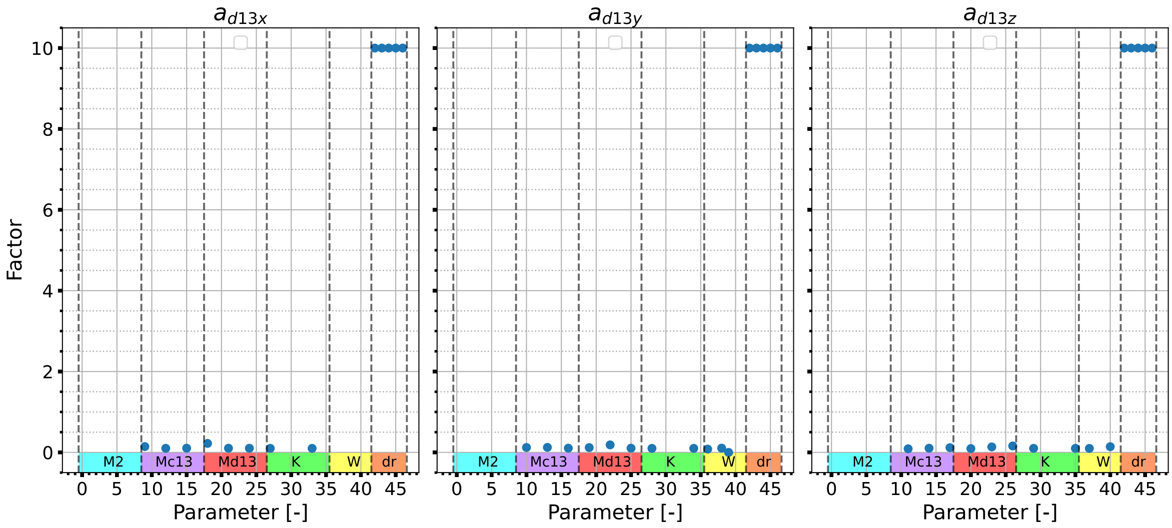

Figure 6.4: Ratio of RMS of the error between the numerical derivative and the design matrix when for variation with dx and $dx/10$ for each parameter in differential mode.

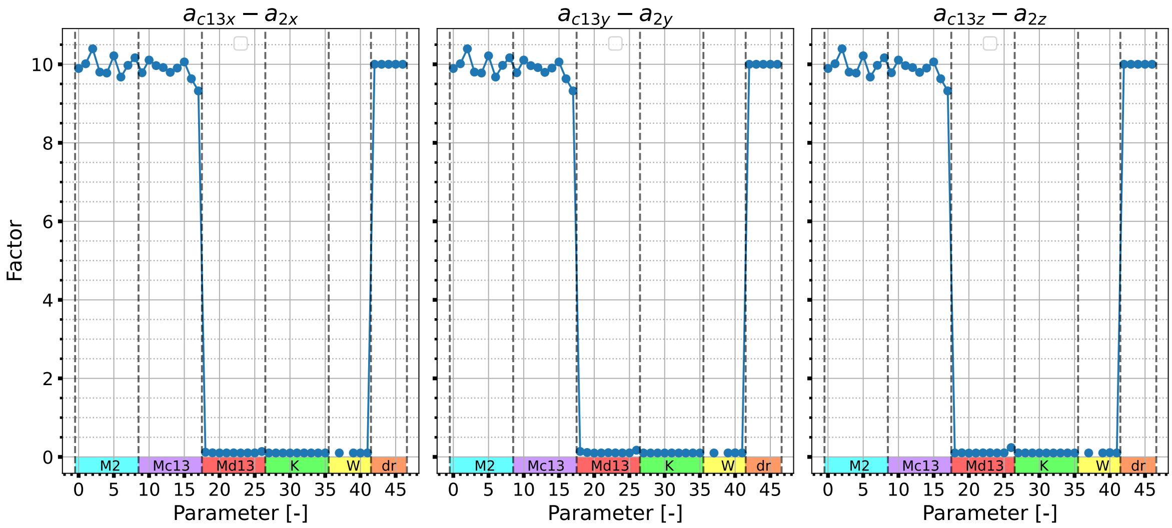

Figure 6.5: Ratio of RMS of the error between the numerical derivative and the design matrix when for variation with dx and $dx/10$ for each parameter in common mode.

6.2.2. Least Squares

Noiseless Model

The least squares verification will first be done without noise to check the correct implementation of the least squares algorithm. Starting from the parameters that are offset w.r.t. the simulated truth, the estimated parameters converge to the true values if the algorithm is implemented correctly. The least squares is initialised with the initial guess $\boldsymbol{x}_0 = \mathbf{0}$. The shaking signal parameters used in verification are given in Table 6.1 with an inter-accelerometer arm length $L_y = 0.6\,\mathrm{m}$.

Table 6.1: Shaking signal parameters for verification

Parameter	Value
T	$3 \times 10^{-6}\ \mathrm{m/s^2/\sqrt{Hz}}$
f_{UB}	$0.1\,\mathrm{Hz}$

Figure 6.6 shows the error between the true and estimated parameters with noiseless observations, with the initial guess and the final estimated solution. The error between the estimated and true parameters at the end of estimation algorithm has reduced by a factor of 10^9 for the $\boldsymbol{K}$ parameters and 10^{14} for the other parameters when compared to the error made due to the initial guess giving a clear evidence of convergence. The K parameters have a higher error as they are multiplied by the square of the acceleration signal, which is already in the order of $\mathrm{\mu m\,s^{-2}}$, leading to a weak observation signal for the estimation. Figures 6.7 and 6.8 further confirm that the ASD of the measurement error (dashed red line) is well below the noise characteristics of the accelerometer (blue line) for noiseless observations.

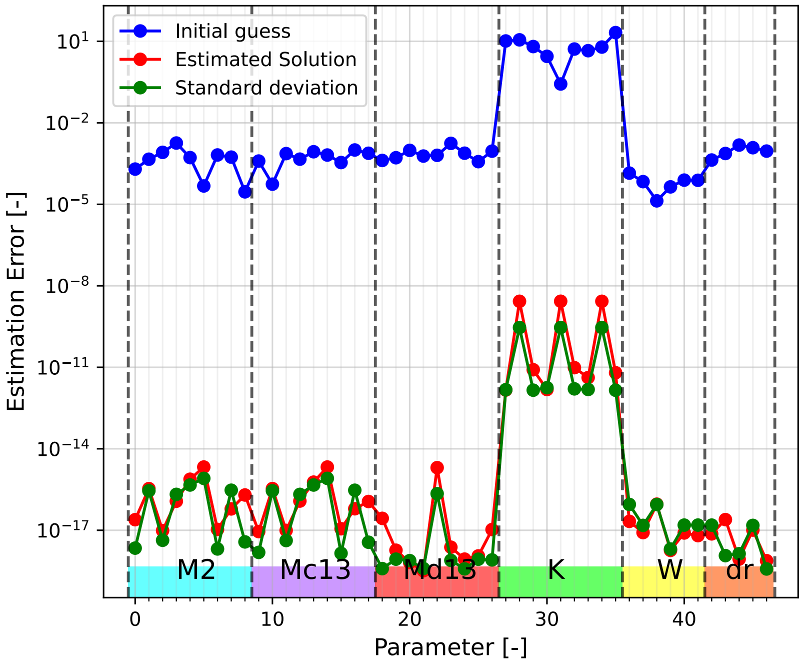

Figure 6.6: Estimation error in parameters $\boldsymbol{x}$ for noiseless observations. All the parameters are unitless except $\boldsymbol{K}$ and $\boldsymbol{dr}$ having units $[\mathrm{s}^2/\mathrm{m}]$ and $[\mathrm{m}]$, respectively.

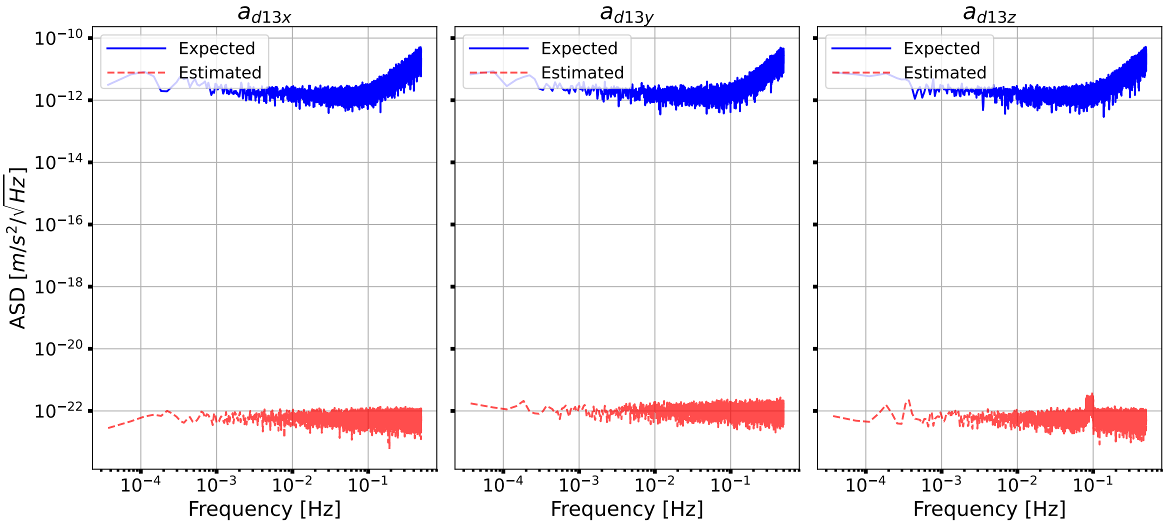

Figure 6.7: Amplitude spectral density of the retrieved measurement error for the differential acceleration mode for the noiseless model.

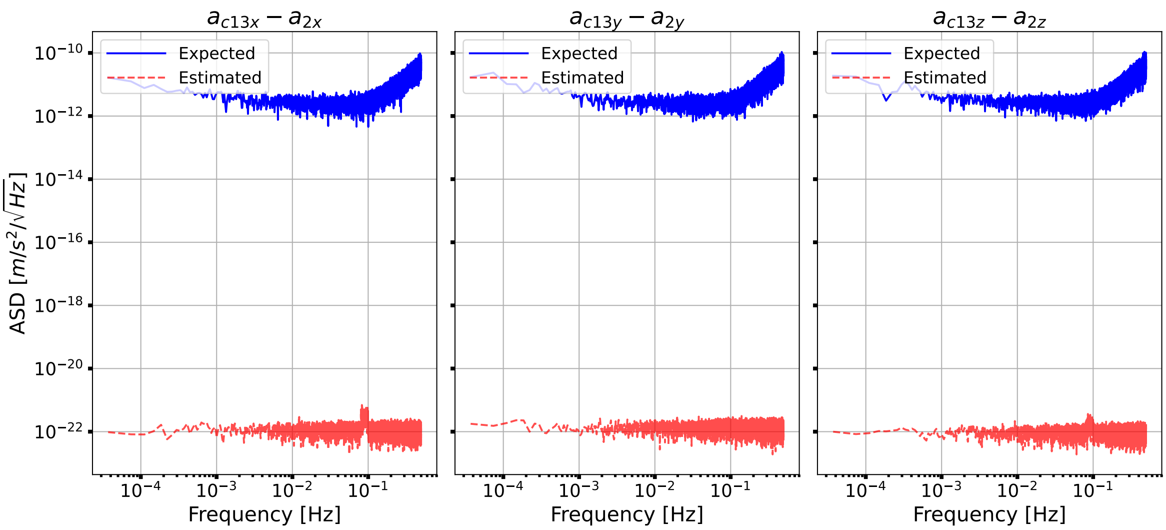

Figure 6.8: Amplitude spectral density of the retrieved measurement error for the common acceleration mode for the noiseless model.

Noise model

Finally, decorrelation filters are incorporated into the algorithm to account for the noise in the least squares fit. To ensure its proper functioning, the least squares fit for noisy observations should converge to the noise level of the observations. The expected pure noise level for the differential mode and common mode, excluding instrument imperfections except for the position offset, can be written as

$$\begin{aligned}\boldsymbol{n}_{diff} = {} & \frac{(\boldsymbol{n}_1 - \boldsymbol{n}_3)}{2} + (\boldsymbol{G}^{meas} - \boldsymbol{G}^{true})\boldsymbol{r}_{d13} + \frac{1}{2}((\boldsymbol{G}^{meas} - \boldsymbol{G}^{true})\boldsymbol{r}_1 + \boldsymbol{n}_1)^2 \\ & + \frac{1}{2}((\boldsymbol{G}^{meas} - \boldsymbol{G}^{true})\boldsymbol{r}_3 + \boldsymbol{n}_3)^2 + \boldsymbol{W}_{d13}^{true}\dot{\boldsymbol{\omega}}_{noise}\end{aligned} \tag{6.6}$$

$$\begin{aligned}\boldsymbol{n}_{comm} = {} & \boldsymbol{n}_2 + \boldsymbol{W}_2^{true}\dot{\boldsymbol{\omega}} - \frac{(\boldsymbol{n}_1 + \boldsymbol{n}_3)}{2} - (\boldsymbol{G}^{meas} - \boldsymbol{G}^{true})\delta\boldsymbol{r}_{c13} - \frac{1}{2}((\boldsymbol{G}^{meas} - \boldsymbol{G}^{true})\boldsymbol{r}_1 + \boldsymbol{n}_1)^2 \\ & - \frac{1}{2}((\boldsymbol{G}^{meas} - \boldsymbol{G}^{true})\boldsymbol{r}_3 + \boldsymbol{n}_3)^2 - \boldsymbol{W}_{c13}^{true}\dot{\boldsymbol{\omega}}\end{aligned} \tag{6.7}$$

This information is derived only for analyzing the tool. It is unavailable in a real mission, as one does not know the true values.

An inspection in the frequency domain (Figures 6.9 and 6.10) is performed by estimating the ASD of the final residual of the least squares fit (orange) and the expected noise (blue) calculated by Equations (6.6) and (6.7). Both for differential and common mode, the ASD agrees in shape and magnitude with the expected noise residual. Furthermore, looking at Figure 6.11, the error of the final estimated solution is smaller than the solution estimated initially with the bandpass filter in the first least-squares step (corresponds to the p=0, r=0 of for loops in steps 4 and 13 of Algorithm 3), except for a few parameters of $\boldsymbol{K}$ and $\boldsymbol{W}$ which is attributed to the random chance due to noise in the observations. Globally, the final solution (corresponds to p=P-1 and r=R-1 of for loops in steps 4 and 14 of Algorithm 3) has an error roughly an order of magnitude lower than the first step error. In conclusion, the least squares algorithm with the decorrelation filter is set up correctly.

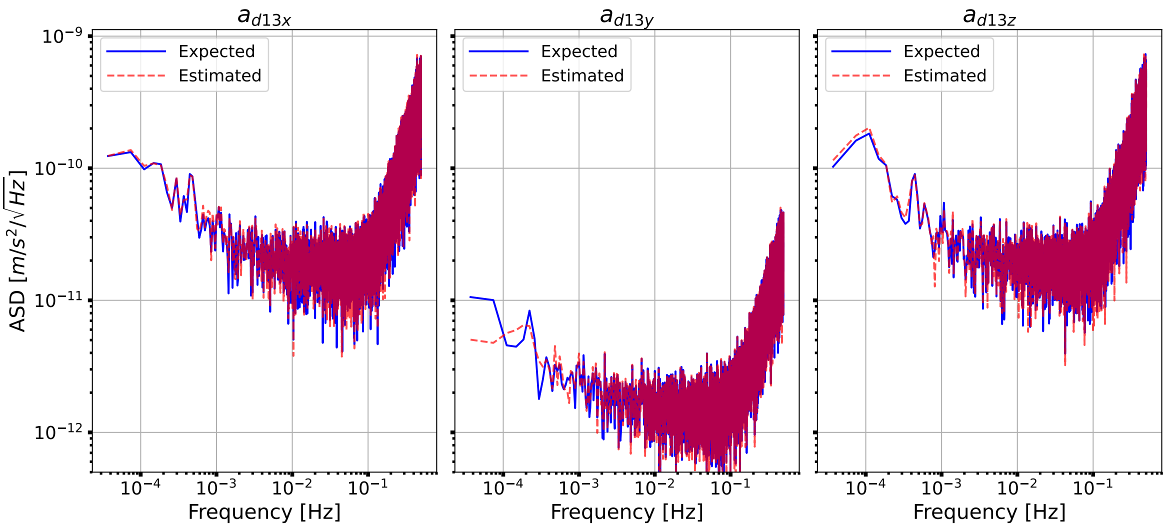

Figure 6.9: Amplitude spectral density of the expected and retrieved noise for the differential acceleration mode.

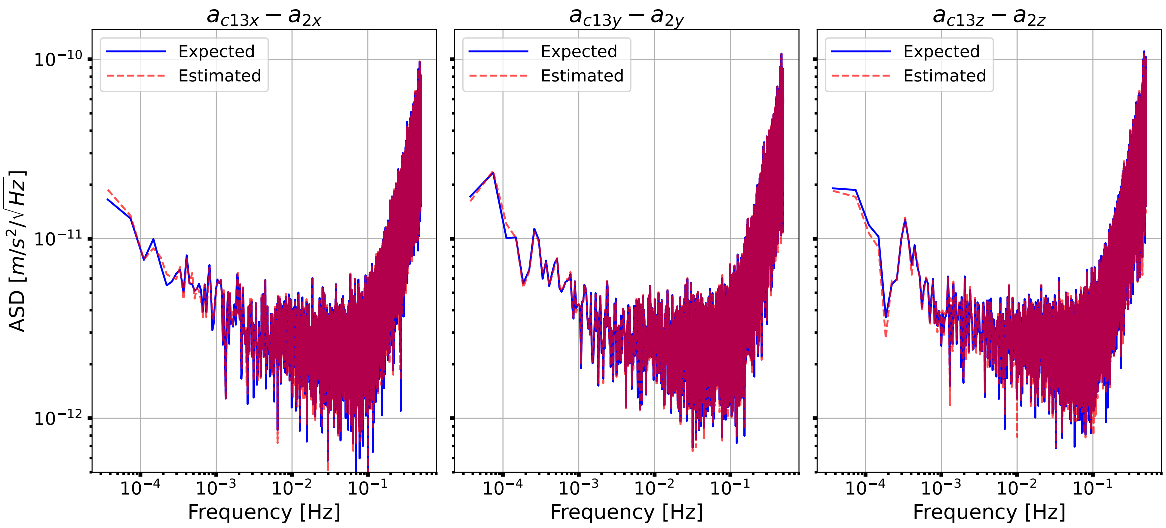

Figure 6.10: Amplitude spectral density of the expected and retrieved noise for the common acceleration mode.

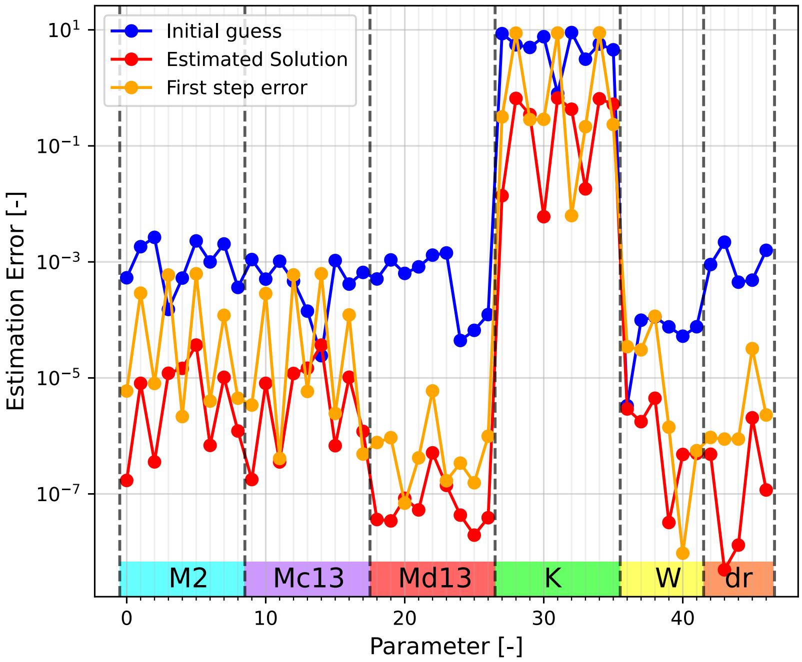

Figure 6.11: Estimation error in parameters $\boldsymbol{x}$ for noisy observations. All the parameters are unitless except $\boldsymbol{K}$ and $\boldsymbol{dr}$ having units $[\mathrm{s}^2/\mathrm{m}]$ and $[\mathrm{m}]$, respectively.

Validation

For validation, parameters from GOCE mission (Personal Communication: C. Siemes) are used as the true parameters and estimated by Algorithm 3. In Figure 6.12a, the initial guess for $\boldsymbol{M}_{c13}$ parameters is already good, having an error of $\approx 10^{-5}$, so the estimated solution does not improve unless a higher thrust acceleration is simulated. The $\delta\boldsymbol{r}$ parameters are not provided; thus, they cannot be compared. The indices 42-46 in the figure are spurious. The estimated parameters are normalized (Figure 6.12b) to show the deviation of each parameter from the true parameter as

$$z = \frac{x_i - x_i^{true}}{\sigma_i}, \tag{6.8}$$

where σ_i is the standard deviation of each estimated parameter, plotted in a 3σ confidence region which accounts for 99.7% of cases. All parameters fall within the confidence region except index 39, which corresponds to the W_{23} element (Equation (5.16)) of the common mode $\boldsymbol{W}$ matrix. Note that the GOCE had six accelerometers, whereas the validation has only three accelerometers, making it more susceptible to noise if the simulated thrust is not high enough, or it could be by random chance. Nevertheless, the parameters are statistically within 3σ deviation from true values,

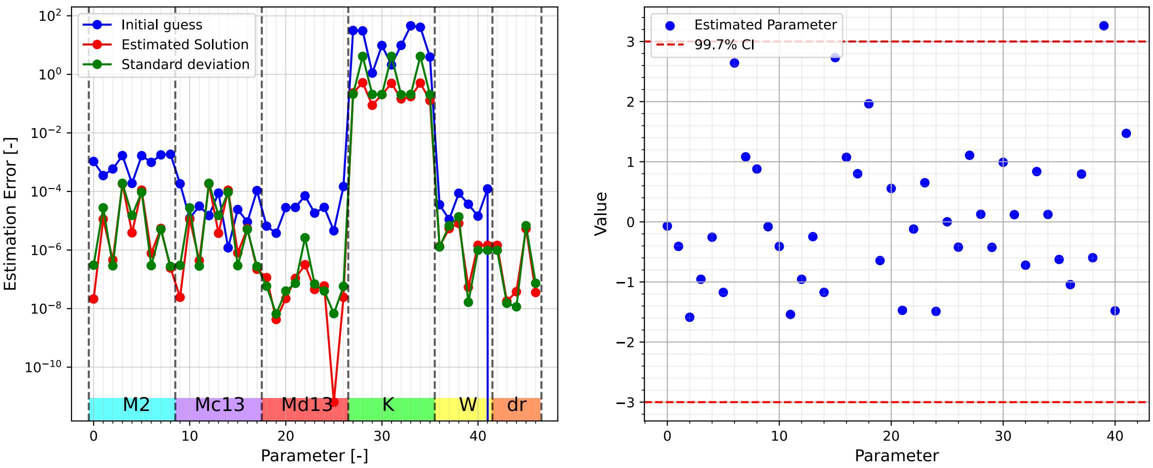

(a) **(b)**

Figure 6.12: a) Estimation error in parameters $\boldsymbol{x}$ for noisy observations. All the parameters are unitless except $\boldsymbol{K}$ having a unit[s^2/m]. b) Deviation of each parameter w.r.t. the true parameters normalized by the standard deviation (Z-score) with the 3σ confidence region.

7

Results

This chapter explores the calibration results of different accelerometer configurations and shaking signal settings. Section 7.1 outlines the design space explored for this study. Next, in Section 7.2, the response variables to assess the calibration quality are described. Section 7.3 then systematically identifies the favourable configuration and shaking manoeuvres for NGGM. The sensitivity and result analysis are combined in this report. Finally, Section 7.4 looks at a special case of a modified response variable in light of accelerometer configuration restrictions.

7.1. Design space

To arrive at an optimal configuration of the accelerometers and optimal region of parameters for the shaking signal, the following settings are explored:

- Thrust acceleration magnitude T_{acc}: [2, 4, 6] $\times 10^{-6}\ \mathrm{m/s^2/\sqrt{Hz}}$
- Shaking duration t_{sh}: [6, 12, 18, 24] hrs
- Upper bound frequency f_{UB}: [0.01, 0.1] Hz. The text will frequently refer to them as low- and high-frequency shaking.
- Inter-accelerometer arm length *L*: [0.4, 0.6, 0.8] m
- Layout: [2, 3, 4]
- Axis: [x, y, z]. For Layout 4, x-, y- and z-axis placement correspond to the accelerometer pairs in xy-, yz- and xz-plane of the body-fixed axis, respectively.

The thrust acceleration range and shaking frequency $f_{UB} = 0.1\,\mathrm{Hz}$ take inspiration from the GOCE where the thrust accelerations of at least $10^{-6}\mathrm{m/s^2/\sqrt{Hz}}$ and up to $10^{-5}\mathrm{m/s^2/\sqrt{Hz}}$ are applied in the range of $0.05\,\mathrm{Hz}$ to $0.1\,\mathrm{Hz}$. Thrust acceleration lower than $2 \times 10^{-6}\ \mathrm{m/s^2/\sqrt{Hz}}$ is insufficient as the observations are too noisy for calibration. The GOCE satellite was shaken for 24 hrs; however, in this study, different shaking times are analysed, as lower shaking times will help conserve fuel. A low shaking frequency $f_{UB} = 0.01\,\mathrm{Hz}$ is also analysed. The GOCE satellite was shaken only at high frequency because the gravity gradient signal was lower than accelerometer noise (Frommknecht et al., 2011). This shaking manoeuvre was specific to GOCE, as the mission measured Earth's gravity gradient tensor. NGGM's objective is to measure the gravity field via LL-SST. Three inter-accelerometer lengths are explored to determine their effect. The lower limit of $0.4\,\mathrm{m}$ stems from the size of the accelerometer with a side of $90\,\mathrm{mm}$. An arm length of $0.4\,\mathrm{m}$ gives $0.2\,\mathrm{m}$ on either side of COM. A margin of at least $0.1\,\mathrm{m}$ between the COM and the accelerometer is reserved space for other components if required. The upper limit of $0.8\,\mathrm{m}$ is arrived by rounding up the height of $0.72\,\mathrm{mm}$ GRACE-FO satellite (Wen et al., 2019). Longer arm lengths will boost the gravity gradients and rotational acceleration signals for calibration, but it will also amplify the noise from those terms if the calibration quality is bad. A bandwidth BW of $0.4f_{UB}$ units is fixed for the pulse of the shaking signal in the frequency domain (refer to Section 5.1.3). Finally, three layouts with three different axis placements are considered, giving rise to nine possible configurations.

The signal generation process (pseudo) randomly generates noise, where the random number generator's seed can affect the calibration results. Thus, multiple seeds for a given configuration and shaking signal settings are considered to examine the distribution effect of the variables on the results and not draw false conclusions from a single outcome due to a random chance.

Given the many possible shaking signal settings for each configuration, running each possible combination for multiple seed realisations is impractical, given the long calibration times due to the size of the linear system of equations to be solved. Therefore, the configurations and settings with a significant effect will be narrowed down step by step using 30 seeds. Once the favourable setting is chosen, realisations from 200 seeds are run to ensure a result with more statistical confidence.

7.2. Response variables

Two response variables assess the different shaking manoeuvres. Section 7.2.1 describes the power ratio metric to assess the calibration performance. Section 7.2.2 gives steps for a rough estimation of the fuel consumption for a given shaking manoeuvre.

7.2.1. Power ratio

To quantify the quality of the calibration, we look at the relative non-gravitational acceleration measurement error, which has to satisfy the requirement defined by Equation (3.3) and shown in Figure 3.6. Since it is a simulation environment, the estimation error can be compared to the true observations.

Using Equations (5.67) to (5.69), the non-gravitational acceleration is reconstructed from the estimated parameters after calibration. The reconstruction is done in science mode for two days to reduce the impact of high-frequency noise, where the satellite is drag-compensated in the along-track direction and no shaking signal is present. The error w.r.t. the true non-gravitational force is given by

$$\boldsymbol{\epsilon}_{ng} = \boldsymbol{a}_{ng}^{true} - \boldsymbol{a}_{ng}^{rcst}. \tag{7.1}$$

A maximum satellite-to-satellite pointing error of $1 \times 10^{-5}\,\mathrm{rad}$ is allowed (Massotti et al., 2021). Figure 7.1 outlines the projection of error vector $\boldsymbol{\epsilon}_{ng}$ on to the maximum allowed LoS vector. The direction in the y- and z-direction is taken as the angle deviation due to small angles. Therefore, the projection of the error vector onto $\textbf{LoS}_{max}$ is the dot product between them.

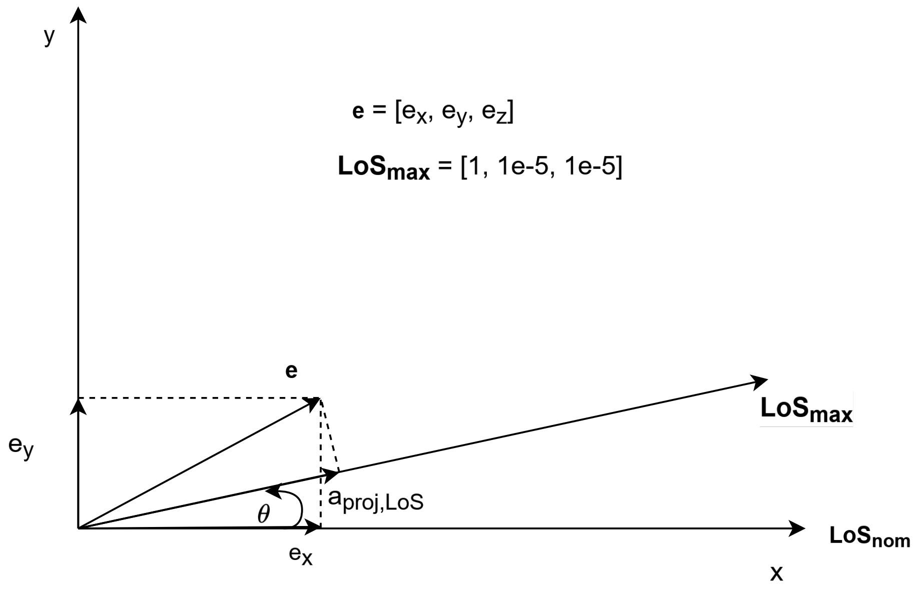

Figure 7.1: Projection of error vector onto the LoS vector in xy-plane body fixed plane.

Thus, the non-gravitational acceleration measurement error along the LoS vector is

$$\epsilon_{ng,LoS} = \boldsymbol{\epsilon}_{ng} \cdot \mathbf{LoS}_{max}. \tag{7.2}$$

The error along the LoS vector is mainly in the along-track direction because if the deviation is larger than $1 \times 10^{-5}\,\mathrm{rad}$, the tracking link is broken anyways. The error in the cross-track and radial direction has a negligible effect (confirmed via analysis, not shown in the report); however, for completeness, it is included in the error calculation.

For a pair of satellites, assuming that they and the calibration are identical and independent, the relative non-gravitational acceleration measurement error is the RMS of the two errors written as

$$\epsilon_{ng,LoS,rel} = \sqrt{\epsilon^2_{ng,LoS,1} + \epsilon^2_{ng,LoS,2}} = \sqrt{2\epsilon^2_{ng,LoS,1}} = \sqrt{2}\epsilon_{ng,LoS,1}. \tag{7.3}$$

The aim of the calibration is that $\epsilon_{ng,LoS,rel}$ satisfies the imposed requirement by Equation 3.3. For example, in Figure 7.2, the ASD of $\epsilon_{ng,LoS,rel}$ for a sample calibration against the requirement is given. In all shaking signal cases, it is at low frequencies where the requirement is violated (shown by the region between green vertical lines). The random instrument noise dominates at high frequencies above $10\,\mathrm{mHz}$. However, at low frequencies, errors in parameter estimation would lead to errors being amplified by the gravity gradients and rotational acceleration terms as they have a higher magnitude at lower frequencies, with peaks occurring at the orbital frequency $0.2\,\mathrm{mHz}$ and its harmonic frequencies. Therefore, the efforts will be focused on satisfying the requirement in the range of $1 \times 10^{-4}\,\mathrm{Hz}$ to $1 \times 10^{-3}\,\mathrm{Hz}$. Satisfying the requirement in this range will also inherently follow at higher frequencies, as the noise floor of the accelerometer is already below the requirement. Furthermore, the accelerometer dictates the requirement in the chosen frequency range, whereas at higher frequencies, LTI is the limiting hardware on the requirement (refer to Section 3.3.2).

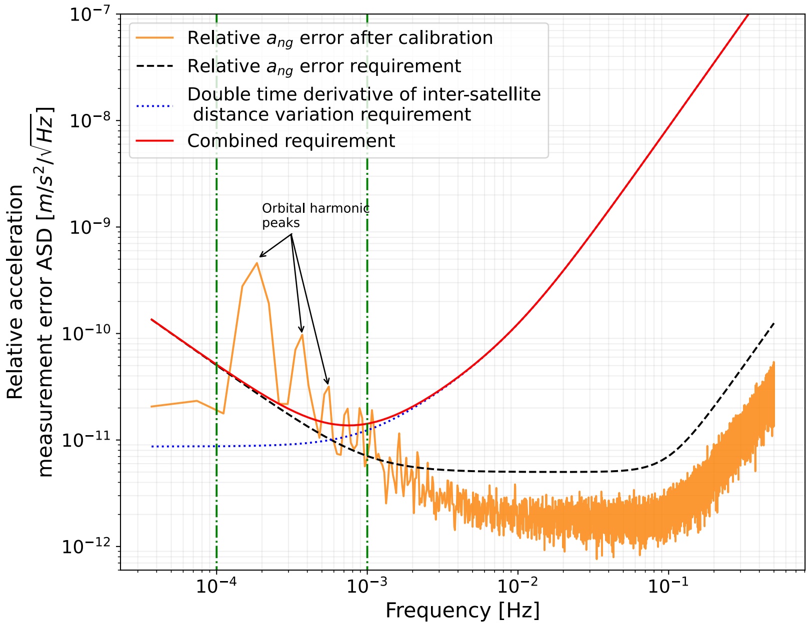

Figure 7.2: Example ASD of $\epsilon_{ng,LoS,rel}$ in science mode after calibration against the requirements.

A single metric will be convenient for comparing the multiple settings posed. The area under the graph in PSD domain gives the power in the frequency band of $1 \times 10^{-4}\,\mathrm{Hz}$ to $1 \times 10^{-3}\,\mathrm{Hz}$.

$$P_{BW} = \Sigma_{f=10^{-4}}^{f=10^{-3}} (A(f))^2 df \tag{7.4}$$

Where df is the bin width based on the window length N chosen for estimating the ASD using Welch's method and the sampling frequency f_s of the accelerometer, calculated as

$$df = \frac{f_s}{N} = \frac{1}{27001} = 3.703 \times 10^{-5}\,\mathrm{Hz}. \tag{7.5}$$

The window length is five times the duration of a single orbit, such that the ASD can resolve down to $3.703 \times 10^{-5}\,\mathrm{Hz}$. In most studies, the length is chosen as a rule of thumb with a margin, as they aim to capture at least the orbital frequency. Note that a longer or shorter window length leads to sharp peaks or merging of peaks, respectively. A longer window length can resolve smaller frequencies compared to a shorter window length (Equation 7.5). With a shorter window, the frequencies within a relatively larger bin will merge into a single peak. Therefore, the derivation of the metric is specific to the choices made here but consistent with other studies.

Finally, a ratio between the power from the $\epsilon_{ng,LoS,rel}$ and the power from the requirement (black dashed line in Figure 7.2) in the frequency range of $1 \times 10^{-4}\,\mathrm{Hz}$ to $1 \times 10^{-3}\,\mathrm{Hz}$ provides a quantifiable metric to assess the performance of calibration for a given shaking signal setting:

$$\text{ratio} = \frac{P_{\epsilon_{ng,LoS,rel}}}{P_{req}} \tag{7.6}$$

If the ratio is below 1, the requirement is satisfied. The ratio is always positive.

A shaking duration of 6 hrs is set as the lower limit to have at least two windows to estimate the ASD with a length of $N = 10000$ and resolve at least $1 \times 10^{-4}\,\mathrm{Hz}$ in the frequency domain.

7.2.2. Fuel Consumption

The simulation outputs the shaking acceleration time series both for linear and angular accelerations. Assuming the mass m of the spacecraft to stay constant at $1000\,\mathrm{kg}$ and the specific impulse $I_{sp} = 60\,\mathrm{s}$ of the cold gas thruster (Wertz et al., 2011), the mass rate $\dot{m}_{fuel}$ is given by

$$\dot{m}_{fuel} = \frac{m a_{sh}(t)}{I_{sp} g_0} \tag{7.7}$$

where $a_{sh}(t)$ is the linear shaking acceleration and g_0 is the gravitational acceleration at sea level. Summing the absolute values (irrespective of the thrust direction) of the mass rate gives a preliminary estimate of fuel consumed (the data is available at every $1\,\mathrm{s}$).

The moment exerted on the satellite by angular accelerations is required to relate it to the fuel consumption. The expression relating angular accelerations $\dot{\boldsymbol{\omega}}$ to the external moment $\boldsymbol{M}$ is

$$\boldsymbol{M} = J\dot{\boldsymbol{\omega}} + \boldsymbol{\omega} \times J\boldsymbol{\omega}, \tag{7.8}$$

where *J* is the inertia tensor of the satellite.

The inertia tensor is based on GRACE-FO's leading satellite (Wen et al., 2019), which is scaled to the mass of NGGM, assuming that the mass distribution does not change.

$$J = \frac{1000}{601.214} \cdot \begin{bmatrix} 110.491 & -1.024 & 0.347 \\ -1.024 & 580.673 & 0.036 \\ 0.347 & 0.036 & 649.690 \end{bmatrix} \mathrm{kgm}^2 \tag{7.9}$$

It is assumed that the moments are generated by linear thrust in only the y- and z-axis thrusters (based on GRACE-FO) given by

$$\boldsymbol{M} = \begin{bmatrix} M_x \\ M_y \\ M_z \end{bmatrix} = \begin{bmatrix} -z \cdot F_y \\ -x \cdot F_z \\ x \cdot F_y . \end{bmatrix} \tag{7.10}$$

By rearranging the equations, the linear force can be used to generate the angular accelerations can be expressed as

$$F_y = \frac{M_x + M_z}{x - z}, \qquad Fz = -\frac{M_y}{x}. \tag{7.11}$$

The mass rate is subsequently calculated from the extracted linear acceleration by dividing the force in each direction $F_{x,y,z}$ by the satellite's mass. Finally, the generated linear and angular accelerations are assumed to be independent. Thus, the total mass rate is an addition of both mass rates, giving a conservative estimate of fuel consumption.

GOCE performed 24 shaking manoeuvres for calibration in a four-year mission due to the drift of accelerometer imperfections with time (Siemes et al., 2019). Assuming a similar drift occurs for NGGM, 42 shaking manoeuvres will be required for a seven-year mission.

7.3. Narrowing down to favourable settings

Axis Placement Analysis

To start, Table 7.1 shows the settings selected for the first analysis. From here on, each new shaking setting will be displayed in this table format with an ID given to each table, which will be included in the figure to track which figure belongs to which shaking setting. In all box plots, the thrust acceleration is varied on the plot's x-axis to get a global view of the effect of settings.

Table 7.1: Initial shaking settings (ID: Setting 1)

t_{sh} [hrs]	f_{UB} [Hz]	L [m]	Layout [-]	Axis [-]
24	0.1	0.6	3	x, y, z

Figure 7.3 gives the box plot representation of ratio variation across 30 seeds for different thrust values at a given axis placement. The box plot contains the following features:

- The middle black line in the box is the median. The median is robust against large outlier values compared to the mean.
- The bottom line of the box is the first quartile $Q1$. 25% of the data lies below this value.
- The top line of the box is the third quartile $Q3$. 75% of the data lies below this value.
- The box contains the middle 50% of the data.
- The height of the box is the Inter-Quartile Range (IQR), given by IQR $= Q3 - Q1$. Tall/slender box shows high variability in the data.
- The whiskers (T and $\perp$) are $\pm 1.5 \times$ IQR away from the quartiles. Note that since the ratio is always positive, the lower whisker will end at the minimum value in the dataset if $Q1 - 1.5 \times$ IQR is larger than the minimum ratio in the dataset.
- The points outside the whiskers are defined as outliers. They are not analysed and discarded.
- The crosses in the box plots are the means.
- The red dashed line is the defined ratio requirement of 1.

The median ratio for x-axis placement (blue boxes) is more than an order of magnitude lower than the y-axis (orange boxes) and approximately by a factor of six from the z-axis (green boxes). The spread (box height) for the x- and z-axis reduces approximately by a factor of two as the thrust acceleration magnitude increases, whereas the y-axis spread stays more or less consistent spanning an order of magnitude, indicating that the calibration is more robust to different noise realisations for the x- and z-axis accelerometer placement.

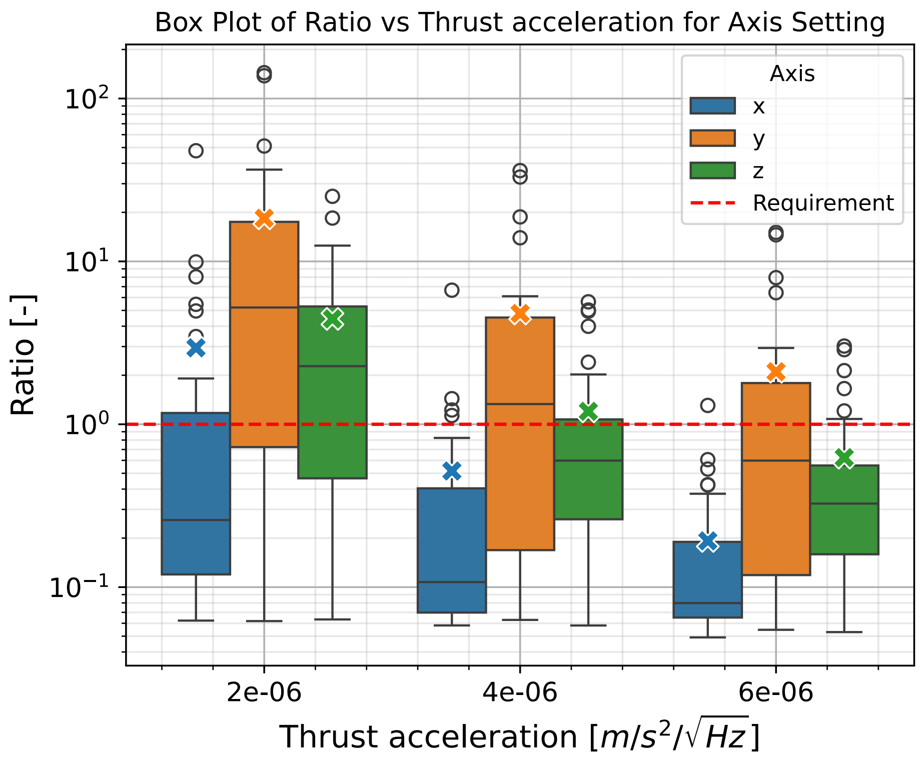

Figure 7.3: Box plot of Ratio vs Thrust for different axis placement (ID: Setting 1).

The reason for poor performance for the y-axis placement can be narrowed to Equation 5.5. For an accelerometer away from the COM, the acceleration expression can be simplified for different axis placements as

- x-axis placement:

$$\boldsymbol{a} = -\begin{bmatrix} V_{xx} + \omega_y^2 + \omega_z^2 \\ V_{xy} - \omega_x\omega_y - \dot{\omega}_z \\ V_{xz} - \omega_x\omega_z + \dot{\omega}_y \end{bmatrix} r_x + \boldsymbol{a}_{ng} \tag{7.12}$$

- y-axis placement:

$$\boldsymbol{a} = -\begin{bmatrix} V_{xy} - \omega_x\omega_y + \dot{\omega}_z \\ V_{yy} + \omega_x^2 + \omega_z^2 \\ V_{yz} - \omega_y\omega_z - \dot{\omega}_x \end{bmatrix} r_y + \boldsymbol{a}_{ng} \tag{7.13}$$

- z-axis placement:

$$\boldsymbol{a} = -\begin{bmatrix} V_{xz} - \omega_x\omega_z - \dot{\omega}_y \\ V_{yz} - \omega_y\omega_z + \dot{\omega}_x \\ V_{zz} + \omega_x^2 + \omega_y^2 \end{bmatrix} r_z + \boldsymbol{a}_{ng}. \tag{7.14}$$

The diagonal elements of the centrifugal acceleration matrix $\boldsymbol{\Omega}^2$ of Equation 5.5, which correspond to the first, second and third element of the column in Equations (7.12) to (7.14). For a given axis placement, the centrifugal acceleration along that axis is the sum of the squares of the angular velocities about the other two axes. For the x- and z-axis placement, ω_y^2 is involved, which can be broken down during the shaking manoeuvre as

$$\omega_y^2 = (\omega_{y,nom} + \Delta\omega_y)^2 = \omega_{y,nom}^2 + \Delta\omega_y^2 + 2\omega_{y,nom}\Delta\omega_y = \Delta\omega_y^2 + 2\omega_{y,nom}\Delta\omega_y, \tag{7.15}$$

where $\omega_{y,nom}$ is the constant nominal pitch rate of the satellite due to its approximately along-track attitude given by Equation 6.2, and $\Delta\omega_y$ is the pitch rate resulting from the shaking manoeuvre. The calibration operation filters out the constant rate and only applies the shaking signal $\Delta\omega_y$, but the shaking signal in the term $2\omega_{y,nom}\Delta\omega_y$ gets boosted by the constant pitch rate of the orbit compared to $\Delta\omega_x$ and $\Delta\omega_z$. The nominal pitch rate of $1.13\,\mathrm{mrad\,s^{-1}}$ is two orders of magnitude higher than the magnitude of the pitch rate from the shaking manoeuvre. Thus, the total angular rate signal during shaking about the y-axis is also two orders of magnitude higher than $\Delta\omega_x$ and $\Delta\omega_z$ as highlighted in Figure 7.4a.

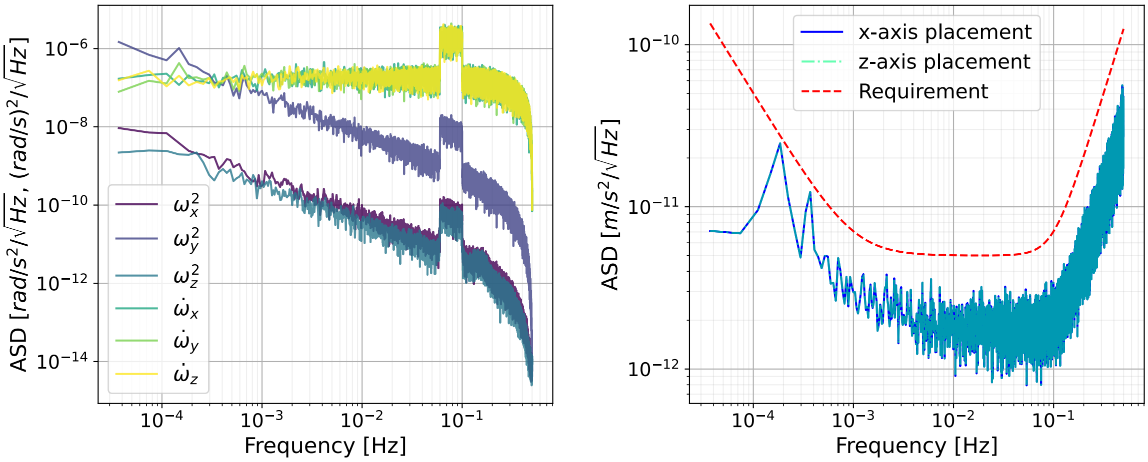

(a) **(b)**

Figure 7.4: a) ASDs due to angular accelerations and the square of angular rates of the shaking signal. b) ASD of $\epsilon_{ng,LoS,rel}$ in science mode after calibration for the x- and z-axis accelerometers placement.

However, one should notice a similar performance for the z-axis. Looking at the $\epsilon_{ng,LoS,rel}$ ASD in Figure 7.4b, there is no difference in the error signature for accelerometers placed on the x (dark blue) or z-axis (light blue) for the same set of hardware parameters. This suggests that the better performance of the x-axis placement stems from a better estimation of the parameters during calibration rather than an effect of noise amplification due to axis placement during the reconstruction of $\boldsymbol{a}_{ng}^{rcst}$ in science mode. The suspected cause lies in the definition of the electrode layout of the accelerometer. From Equation 5.16, the angular acceleration is projected only onto the y and z-component of the measured linear acceleration (Equation 5.15). Therefore, for the x-axis placed accelerometers, the z component of the linear acceleration signal should get a boost from the angular acceleration projection compared to the z-axis placed accelerometers, which do not get any signal amplification on the x component. Since the $\boldsymbol{W}$ parameters are an order of magnitude smaller than $\boldsymbol{M}$ parameters (Table 5.3), the ASD of the acceleration signal is plotted in Figure 7.5 without the $\boldsymbol{a}_{ng}$ and $\dot{\omega}$ in Equations (7.12) and (7.14) to see the effect of electrode layout. The pulse ceiling of the z component of the linear acceleration (orange) in Figure 7.5a is roughly five times that of the x component ceiling (purple) in Figure 7.5b.

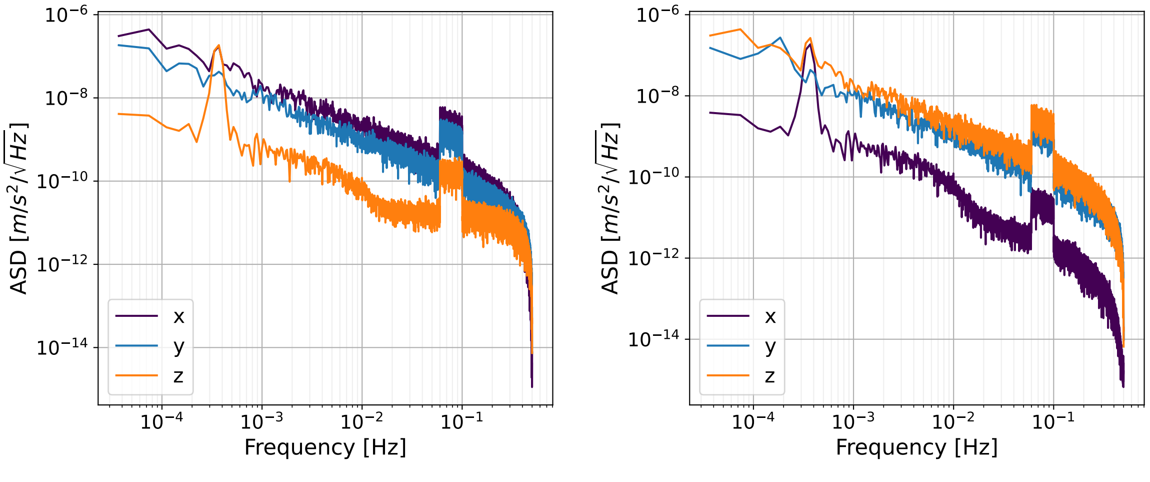

(a) **(b)**

Figure 7.5: a) ASD of linear acceleration components for x-axis placed accelerometers. b) ASD of linear acceleration components for z-axis placed accelerometers.

Shaking Frequency Analysis

Moving forward, the effect of shaking frequency is analysed (Table 7.2).

Table 7.2: Shaking settings after axis placement (ID: Setting 2)

t_{sh} [hrs]	f_{UB} [Hz]	L [m]	Layout [-]	Axis [-]
24	0.1, 0.01	0.6	3	x

Before carrying out the analysis, the thrust acceleration magnitude at different frequencies has to be investigated. Figures 7.6a and 7.7a show the ASD of the filter with $T_{acc} = 2 \times 10^{-6}\,\mathrm{m/s^2/\sqrt{Hz}}$ used to generate the high- and low-frequency signal and its corresponding time domain signal, respectively. The high-frequency signal varies in the time domain from -1.5×10^{-6} to $1.5 \times 10^{-6}\,\mathrm{m\,s^{-2}}$ (Figure 7.6b). The low-frequency shaking signal with the same thrust magnitude in the ASD has a variability of -6×10^{-7} to $6 \times 10^{-7}\,\mathrm{m\,s^{-2}}$ in the time domain (Figure 7.7b). This discrepancy arises because the higher-frequency shaking signal has a higher area under the pulse in the frequency domain, leading to greater power.

To match the same time domain magnitude variability across high and low-frequency shaking, the power of the low-frequency signal is amplified by scaling up the acceleration magnitude of the ASD filter in the frequency domain. The power of the signal is given by the

$$P = \Sigma_{f=f_s/N}^{f=0.5} A(f)^2 df, \tag{7.16}$$

where df is defined by Equation 7.5.

The scale factor to amplify the low-frequency signal is calculated as the power ratio between the high- and low-frequency shaking:

$$k = \sqrt{\frac{P_{f_{high}}}{P_{f_{low}}}}. \tag{7.17}$$

The acceleration magnitude of the ASD filter is scaled by this factor (Figure 7.8a). The ASD of the filter is lifted, with the pulse ceiling approximately thrice its original value. The corresponding time domain acceleration signal (Figure 7.8b) now has a similar variability -1.5×10^{-6} to $1.5 \times 10^{-6}\,\mathrm{m\,s^{-2}}$ in magnitude.

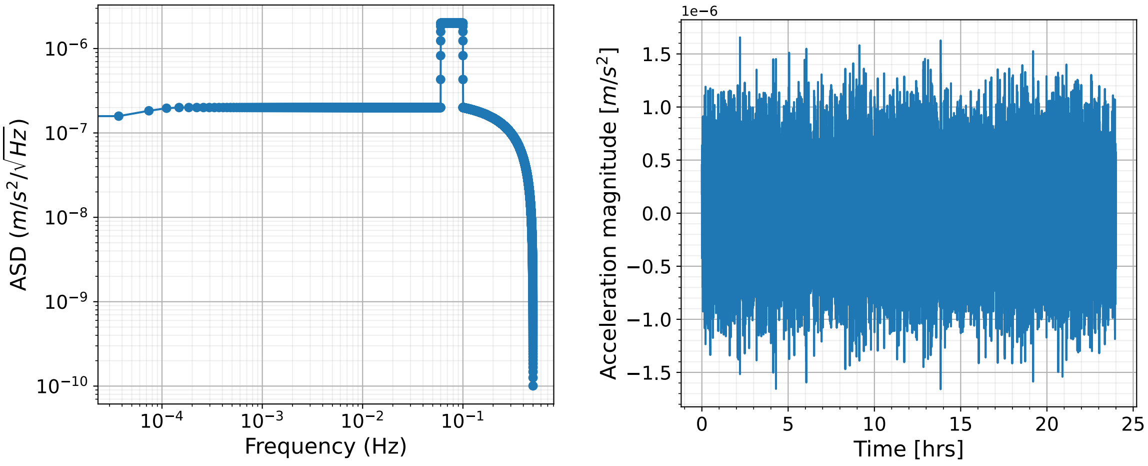

(a) **(b)**

Figure 7.6: a) Filter ASD to generate the high-frequency signal. b)Time domain representation of the high-frequency shaking with an RMS of $4.08 \times 10^{-7}\,\mathrm{m\,s^{-2}}$.

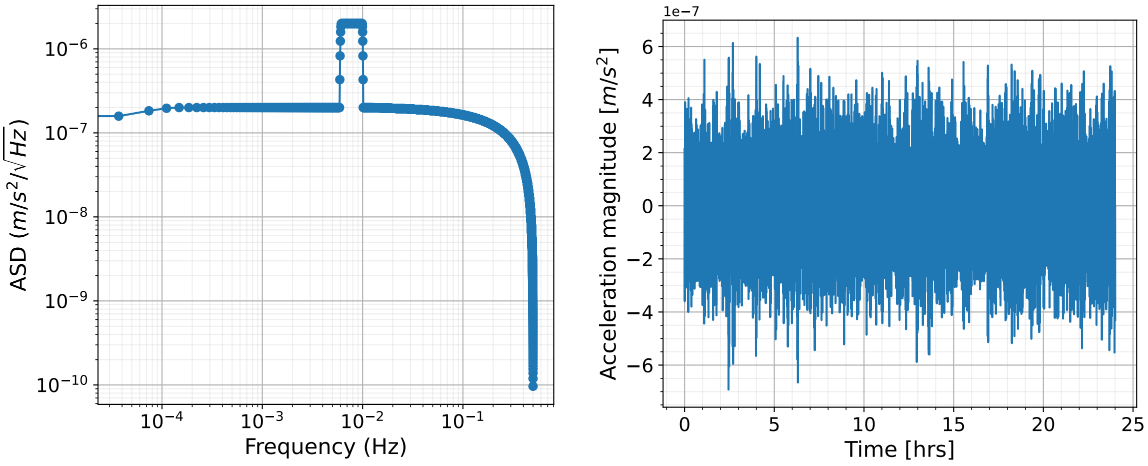

(a) **(b)**

Figure 7.7: a) Filter ASD to generate the low-frequency signal without thrust scaling. b) Time domain representation of the low-frequency shaking without thrust scaling with an RMS of $1.51 \times 10^{-7}\,\mathrm{m\,s^{-2}}$.

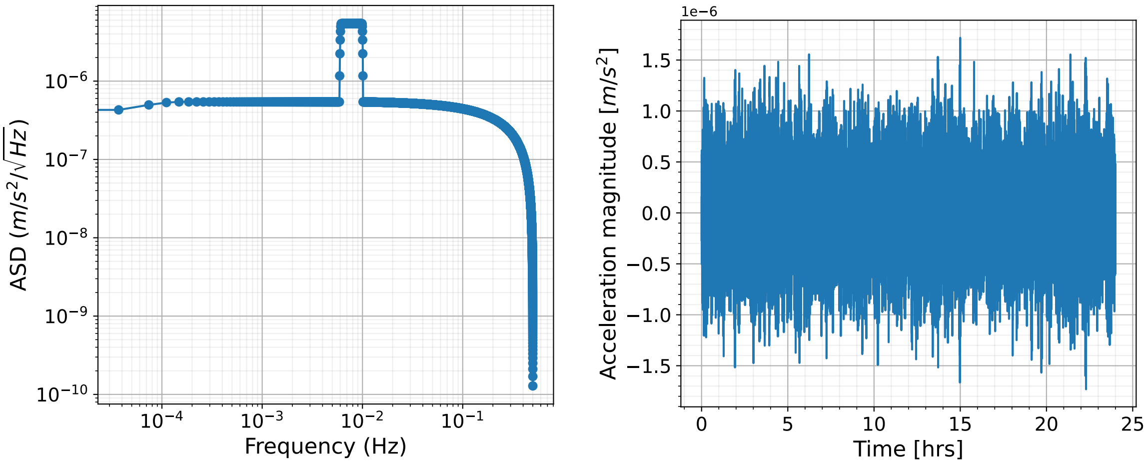

(a) **(b)**

Figure 7.8: a) Filter ASD to generate the low-frequency signal with thrust scaling. b) Time domain representation of the low-frequency shaking with thrust scaling with an RMS of $4.1 \times 10^{-7}\,\mathrm{m\,s^{-2}}$.

With the thrust acceleration appropriately scaled to have the same magnitude variability in the time domain, the ratio variation across 30 seeds for different thrust acceleration values for high and low-frequency shaking is highlighted in Figure 7.9. For all thrust acceleration levels, the low-frequency shaking (blue boxes) produces ratio values approximately half in value compared to its counterpart for the $Q3$, with lower variation.

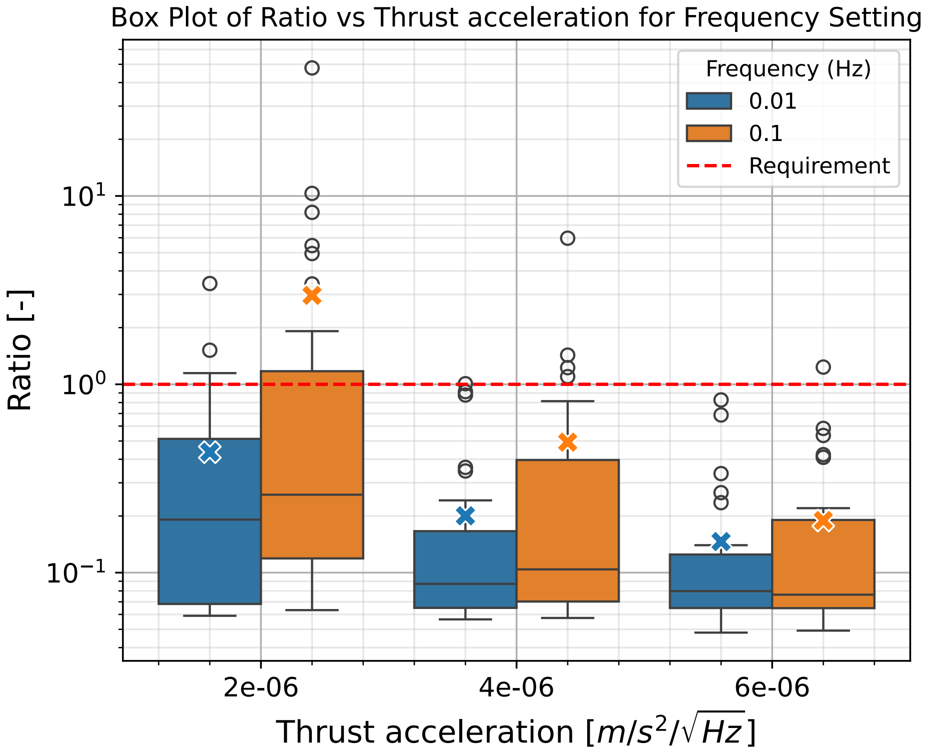

Figure 7.9: Box plot of Ratio vs Thrust for high and low shaking frequency (ID: Setting 2).

This is explained by the angular rates for the high- and low-frequency shaking in the time domain presented by Figures 7.10a and 7.10b in the satellite's body-fixed frame. The lower frequency shaking (Figure 7.10b) accumulates a higher magnitude of angular rates with a variation of about $\pm 6 \times 10^{-5}\,\mathrm{rad\,s^{-1}}$, thrice the angular rate magnitude achieved at the higher frequency shaking (Figure 7.10a). This is again tied into Equation 5.5, where higher angular rates will boost the acceleration signal due to centrifugal force for off-centre accelerometers during calibration.

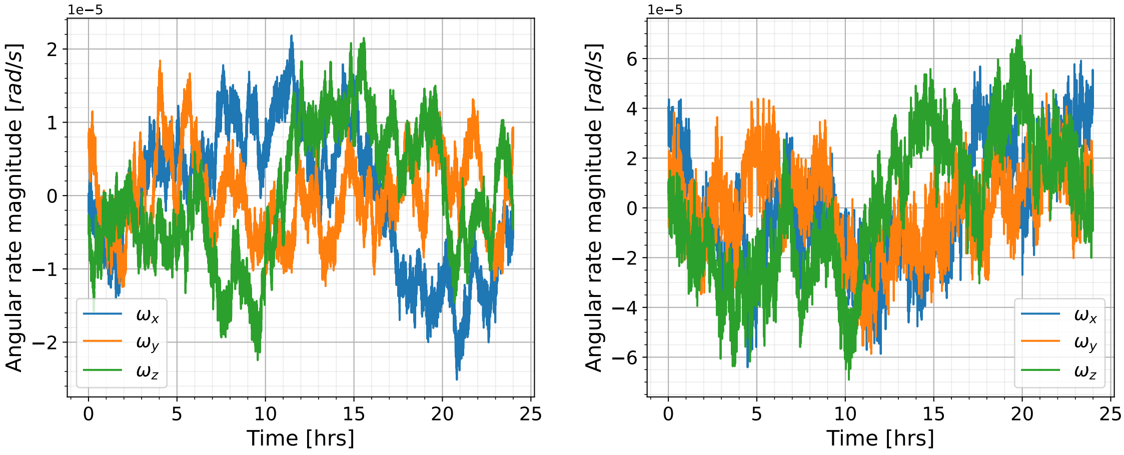

(a) **(b)**

Figure 7.10: Time domain evolution of angular rates. a) Angular rates at high-frequency shaking. b) Angular rates at low-frequency shaking.

Figure 7.11 compares the ratio across 200 seeds for scaled and unscaled thrust acceleration cases. When the thrust scaling is omitted, the low-frequency produces higher valued ratios with approximately half the realizations violating the requirement, than when scaling is applied, confirming the conclusion drawn from just 30 realizations. Without the thrust scaling, the thrust magnitude in the time domain is smaller, so the frequency effect cannot be compared on the same grounds. A choice was made to compare them similarly at the acceleration unit level.

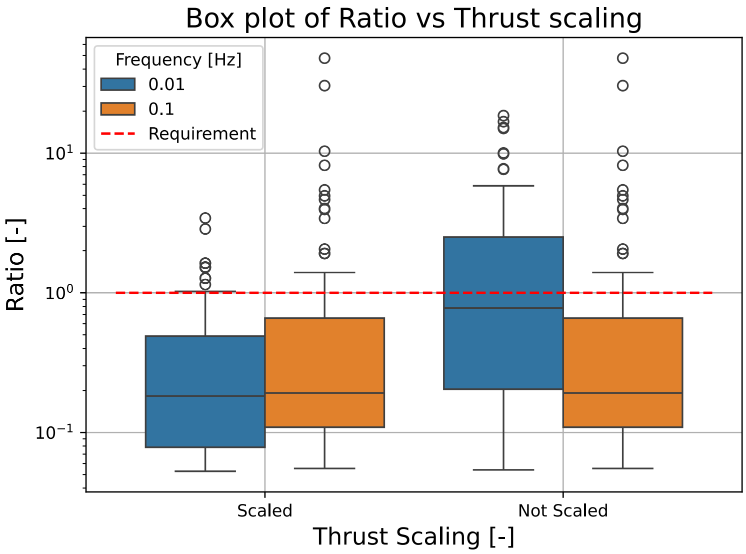

Figure 7.11: Box plot of Ratio vs application of thrust scaling for high- and low-frequency shaking

Layout and Arm Length Analysis

Fixing the configuration with placement on the x-axis with a low frequency shaking, the layout and inter-accelerometer arm lengths are varied with the values given in Table 7.3. Three different layouts with varying numbers of accelerometers are described in Section 3.3.2. The x-axis placement for Layout 4 has one pair on the x-axis and the other on the y-axis. Also, three gradiometer arm lengths for the pair are explored to observe any effect on the distance from the COM.

Table 7.3: Shaking settings for layout and arm length variations (ID: Setting 3)

t_{sh} [hrs]	f_{UB} [Hz]	L [m]	Layout [-]	Axis [-]
24	0.01	0,4, 0.6, 0.8	2, 3, 4	x

Figures 7.12a and 7.12b illustrates the ratio distribution for different layout configurations and the inter-accelerometer arm lengths across 30 seeds, respectively. In Figure 7.12a, having an additional accelerometer in Layout 3 (orange boxes) than in Layout 2 (blue boxes) lowers the median ratio by ≈ 1.5. Layout 3 performs better with a lower median than Layout 2 because of the addition of common mode observations. In contrast, Layout 2 only has differential mode equations, thus having three fewer observation equations to solve during calibration, making the parameter estimation more susceptible to noise in observations. However, the performance improvement only becomes apparent at higher thrust acceleration levels. At thrust acceleration of $T_{acc} = 2 \times 10^{-6}\,\mathrm{m/s^2/\sqrt{Hz}}$ (leftmost group of boxes), the variability between the two (blue and orange boxes) is quite similar, indicating susceptibility to noise in the observations. On the other hand, Layout 4 (green boxes) significantly outperforms the other two layouts by an order of magnitude. Although adding an accelerometer at the COM in Layout 3 provides another set of observations, the centre accelerometer is oblivious to the impact of gravity gradients and rotational acceleration terms as it is at the COM. In contrast, with an additional pair on another axis in Layout 4, not only does it provide common mode observations but also an additional set of differential mode observations, thus adding sensitivity of gravity gradients and rotational acceleration to the observations, resulting in an improved performance by a significant reduction in ratio magnitude and variability across the seeds.

Figure 7.12b depicts the effect of inter-accelerometer arm lengths on the ratio quality. One would expect that having a longer arm length will help boost the gravity gradients and rotational acceleration effects during calibration, but the same applies when reconstructing $\boldsymbol{a}_{ng}^{rcst}$ and $\boldsymbol{\epsilon}_{ng}$. However, the ratio variation and median across all the lengths have similar variability (box height) and medians, and no stand-out improvement in ratio for a given arm length. Therefore, the inter-accelerometer arm length is deemed as a trivial factor and is left as a free variable for designers.

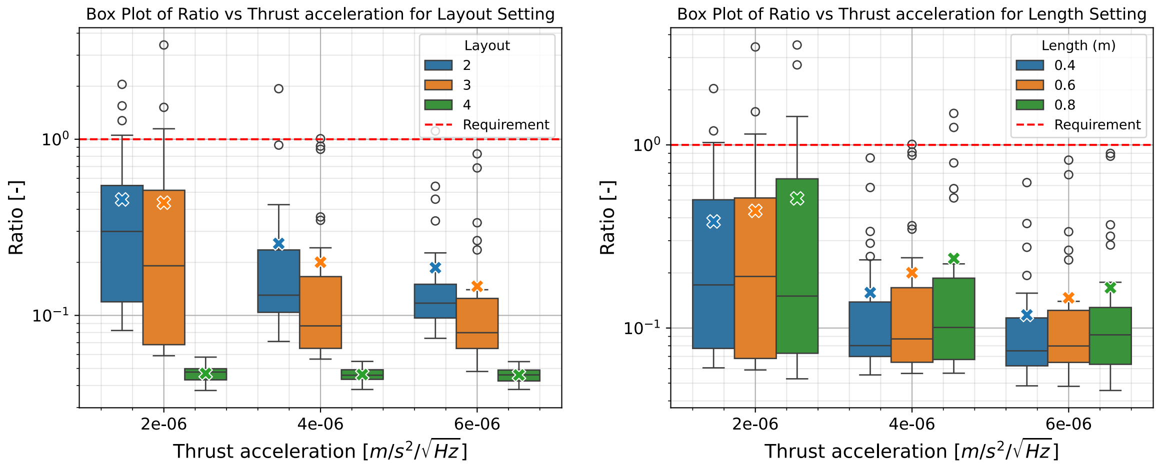

(a) **(b)**

Figure 7.12: a) Box plot of Ratio vs Thrust for Layouts 2, 3 and 4. b) Box plot of Ratio vs Thrust for gradiometer arm lengths of 0.4, 0.6 and 0.8 m. (ID: Setting 3)

Shaking Duration Analysis

Finally, the shaking duration for calibration is varied, lasting a few hours to a day, as given in Table 7.4. For the time being, Layout 3 is selected as the improved performance of Layout 4 would not explicitly highlight the shaking duration's effect. Figure 7.13 visualizes the ratio variation for duration settings. As expected, longer shaking durations help lower the ratio *Q3*, as longer shaking leads to more observations for the least squares inversion. At a thrust acceleration of $2 \times 10^{-6}\,\mathrm{m/s^2/\sqrt{Hz}}$ (leftmost group), a shaking duration of at least 24 hrs is required to be confident that the requirement is fulfilled as the box lies well below it because for shorter durations (blue, orange and green box), the boxes violate the requirement. To achieve short durations, one must choose a higher thrust acceleration magnitude.

Table 7.4: Shaking settings for shaking duration variation (ID: Setting 4)

t_{sh} [hrs]	f_{UB} [Hz]	L [m]	Layout [-]	Axis [-]
6, 12, 18, 24	0.01	0.6	3	x

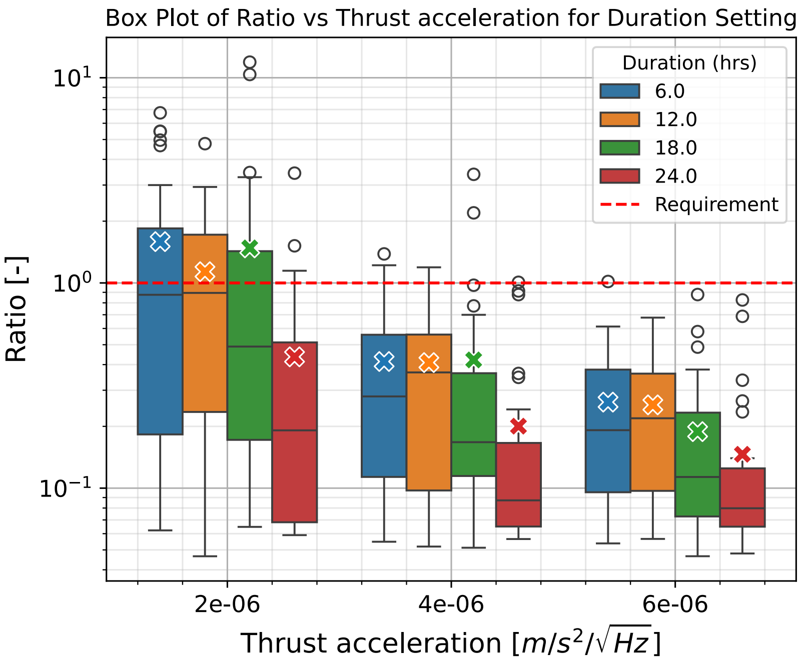

Figure 7.13: Box plot of Ratio vs Thrust for different shaking durations (ID: Setting 4).

A higher thrust acceleration (middle and rightmost group) lowers the ratio for all settings as the box height gets shorter by approximately 1.5. This indicates that randomness plays a major role in calibration performance at lower thrust levels. Opting for a higher thrust acceleration gives more freedom to select other variables, such as the shaking duration and frequency, which can help conserve fuel, and the number of accelerometers and their placement, which is imperative for the volume and power budget of the satellite. However, a thrust value of $2 \times 10^{-6}\,\mathrm{m/s^2/\sqrt{Hz}}$ is already at the limits of the FCT requirements considered in this report (refer to Section 3.3.3), making those variables vital for the performance of the calibrated accelerometers.

Confirming the Analysis across 200 seeds

A shaking duration analysis of 200 seed realizations is conducted to gain further confidence in the choices made so far with the settings mentioned in Table 7.5. Figure 7.14 depicts that at least 24 hrs of shaking (middle teal coloured box) is indeed required for the middle 50% of the ratios produced to be below the requirement. Around 88% of realizations satisfy the requirement. For longer shaking durations, the ratio improves, but the reduction rate slows down as well. Figure 7.15a depicts the evolution of the square root of the ratio's median as the shaking duration increases, normalized to the 6 hrs of shaking. The red line is the theoretical $\sqrt{n}$ law, which states that the standard error of the estimated parameters in a least squares fit reduces by a factor of $\sqrt{n}$, where n is the number of observations in a least squares problem. The normalized median does not fully agree with the law. The law is for the estimated parameters of the least squares fit following a normal distribution. In contrast, the ratio is a derived parameter that does not follow a normal distribution but a right-skewed distribution, as shown in Figure 7.15b, where the histogram representation of the ratio for different shaking durations is given. The right-skewness can also be spotted from all the box plots where the mean of the ratio lies close to or above the *Q3* of the data set. However, qualitatively, it does signify that the reduction rate slows down for higher shaking durations. Shaking durations above 30 hrs have little performance improvement, with approximately 95% of realizations satisfying the requirement.

At a thrust acceleration of $2 \times 10^{-6}\,\mathrm{m/s^2/\sqrt{Hz}}$, an average of $0.16\,\mathrm{kg}$ of fuel is consumed at 24 hrs per manoeuvre. A total of $6.72\,\mathrm{kg}$ of fuel is consumed in the mission's lifetime if 42 shaking manoeuvres are performed.

Table 7.5: Shaking settings for shaking duration variation at $T_{acc} = 2 \times 10^{-6}\,\mathrm{m/s^2/\sqrt{Hz}}$. (ID: Setting 5)

T_{acc} [$\mathrm{m/s^2/\sqrt{Hz}}$]	t_{sh} [hrs]	f_{UB} [Hz]	L [m]	Layout [-]	Axis [-]
2×10^{-6}	6, 12, 18, 24, 30, 36, 42	0.01	0.6	3	x

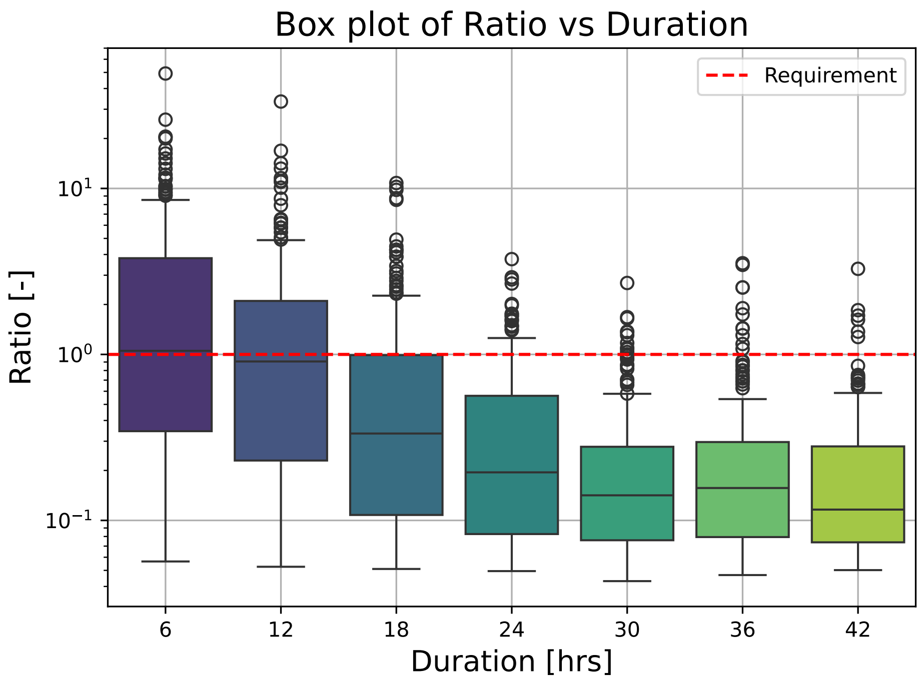

Figure 7.14: Box plot of Ratio vs Duration for 200 realizations (ID: Setting 5)

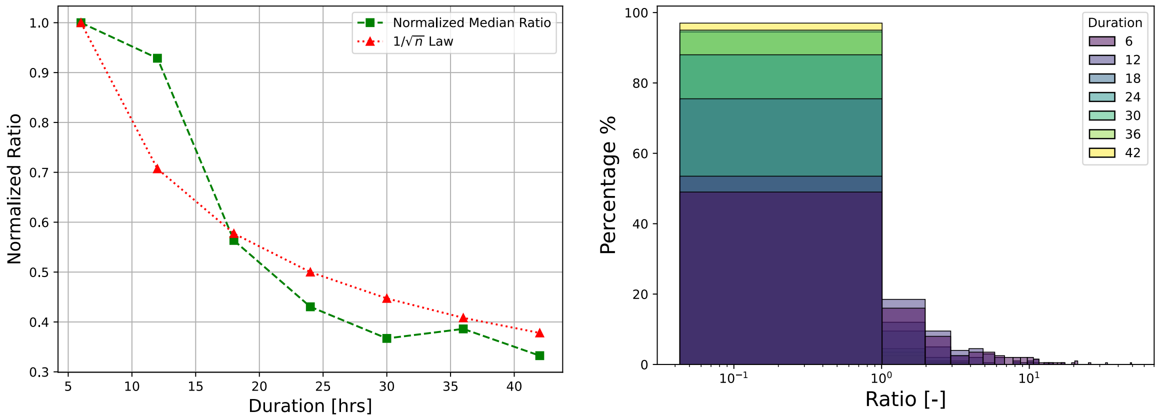

(a) (b)

Figure 7.15: a) Median of the square root of the ratio normalized w.r.t. the 6 hrs of shaking duration (ID: Setting 5). b) Percentage histogram of ratio for different durations (ID: Setting 5).

If the budget allows, one could always opt for one additional accelerometer for Layout 4, as it greatly outperforms other layouts. Figure 7.16 shows the ratio variation for Layout 4 across 200 seeds. It allows us to lower the thrust acceleration level to $6 \times 10^{-7}\,\mathrm{m/s^2/\sqrt{Hz}}$ and reduce the shaking duration to 6 hours (second group's blue box). This leads to a fuel consumption of $0.012\,\mathrm{kg}$ per manoeuvre. As discussed, an additional pair adds sensitivity to gravity gradients and rotational acceleration terms on another axis. However, this comes at a price of additional power consumption of $2\,\mathrm{W}$ and a mass of $1.5\,\mathrm{kg}$.

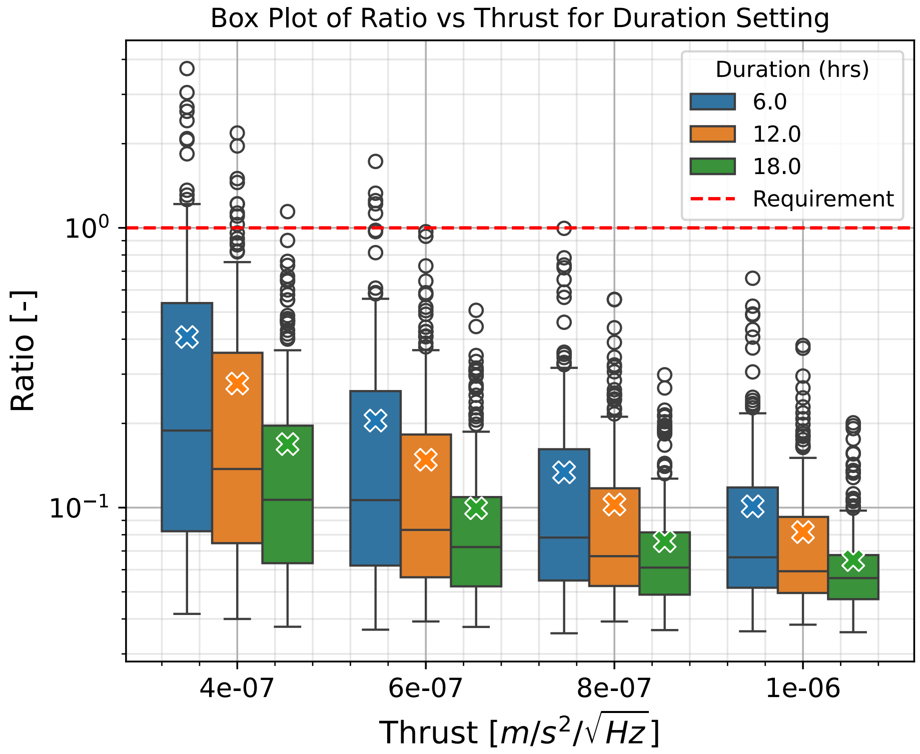

Figure 7.16: Box plot of Ratio vs Thrust for different shaking durations for Layout 4.

7.4. Modified Power Ratio

Due to the accommodation of the LTI assembly, the along-track placement of the accelerometers may not be possible. Layout 3 with y-axis placement is envisioned to be flown on board the NGGM satellites. As discovered in Section 7.3, the y-axis placement is the worst-performing due to the absence of a constant pitch rate from attitude control, making the configuration susceptible to noise for calibration. However, the presence of the centre accelerometer in Layout 3 allows a modified approach to reconstruct the non-gravitational acceleration $\boldsymbol{a}_{ng}^{rcst}$ for science mode.

Previously, $\boldsymbol{a}_{ng}^{rcst}$ was constructed by averaging the calibrated acceleration at nominal positions of all three accelerometers using Equation 5.69. However, the off-centre placement and position offset $\delta\boldsymbol{r}$ will increase the estimation error of calibrated acceleration in Equation 5.67. Therefore, instead of reconstructing $\boldsymbol{a}_{ng}^{rcst}$ by averaging the three accelerometers, $\boldsymbol{a}_{ng}^{rcst}$ is reconstructed by just the centre accelerometer. It has no gravity gradients and rotational acceleration effects as it is defined as the reference for COM. The rest of the steps to calculate the power ratio follow as described in subsection 7.2.1. The shaking signal settings are defined in Table 7.6. The thrust acceleration is set to the upper limit for FCT and a shaking duration of 24 hrs to simulate a likely scenario for the mission. The shaking frequency is also varied since its performance was not assessed for the y-axis placement.

Figure 7.17 compares the effect of two ways of reconstructing $\boldsymbol{a}_{ng}^{rcst}$ on the ratio at high- and low-frequency shaking. Using just the central accelerometer provides no improvement over averaging all three accelerometers, as the median, *Q1*, and *Q3* are similar when incorporating all three or using just the central accelerometer for high- and low-frequency shaking. Even shaking at low frequency proves to be fruitless, as the observations are too noisy. Moreover, Figure 7.18 shows that utilizing only the central accelerometer increases the noise, especially at high frequencies, which is averaged out when using three accelerometers.

As it turns out, the off-centre placement and position offset $\delta\boldsymbol{r}$ are not influential in reconstructing the measurement error in science mode. During the calibration, all three accelerometers have to be used, and due to the placement on the y-axis, the estimation of $\boldsymbol{M}$ and $\boldsymbol{K}$ matrices is marred, leading to poor calibration quality. Only 35% of realizations out of 200 (retrieved from the histogram, not shown) fall under the requirement for low-frequency shaking compared to 88% for the same shaking signal, but the accelerometers were placed on the x-axis. A higher thrust acceleration is a must to calibrate this configuration. From Figure 7.19, a thrust acceleration of at least $8 \times 10^{-6}\,\mathrm{m/s^2/\sqrt{Hz}}$ is required for the box to fall below the requirement, which is not possible with the current cold gas thruster's capability. Additionally, such high thrust acceleration falls outside the measurement range $\pm 6.4 \times 10^{-6}\,\mathrm{m\,s^{-2}}$ of the accelerometers. Assuming it is possible, it will consume at least $0.80\,\mathrm{kg}$ of fuel for 30 hrs of shaking, which results in around $34\,\mathrm{kg}$ of fuel for 42 shaking manoeuvres.

Table 7.6: Shaking settings for modified metric. (ID: Setting 6)

T $[\mathrm{m/s^2/\sqrt{Hz}}]$	t_{sh} [hrs]	f_{UB} [Hz]	L [m]	Layout [-]	Axis [-]
2×10^{-6}	24	0.01, 0.1	0.6	3	y

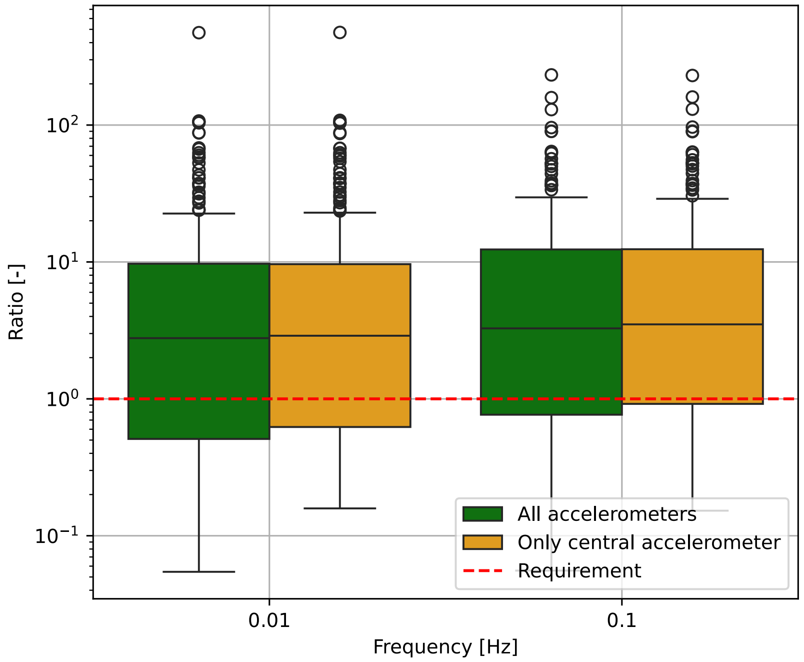

Figure 7.17: Box plot of Ratio vs Shaking frequency for $\boldsymbol{a}_{ng}^{rcst}$ reconstruction using all three accelerometers or just the central accelerometer (ID: Setting 6).

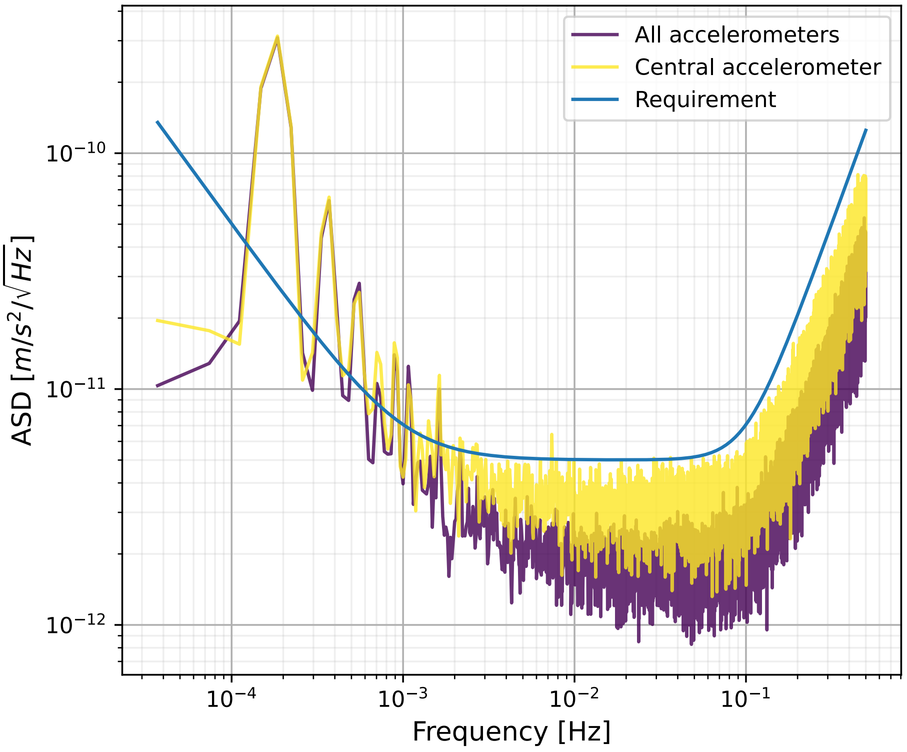

Figure 7.18: ASD of the $\epsilon_{ng,LoS,rel}$ for $\boldsymbol{a}_{ng}^{rcst}$ reconstruction by averaging all three accelerometers or utilizing just the central accelerometer at $T = 2 \times 10^{-6}\ \mathrm{m/s^2/\sqrt{Hz}}$ (ID: Setting 6).

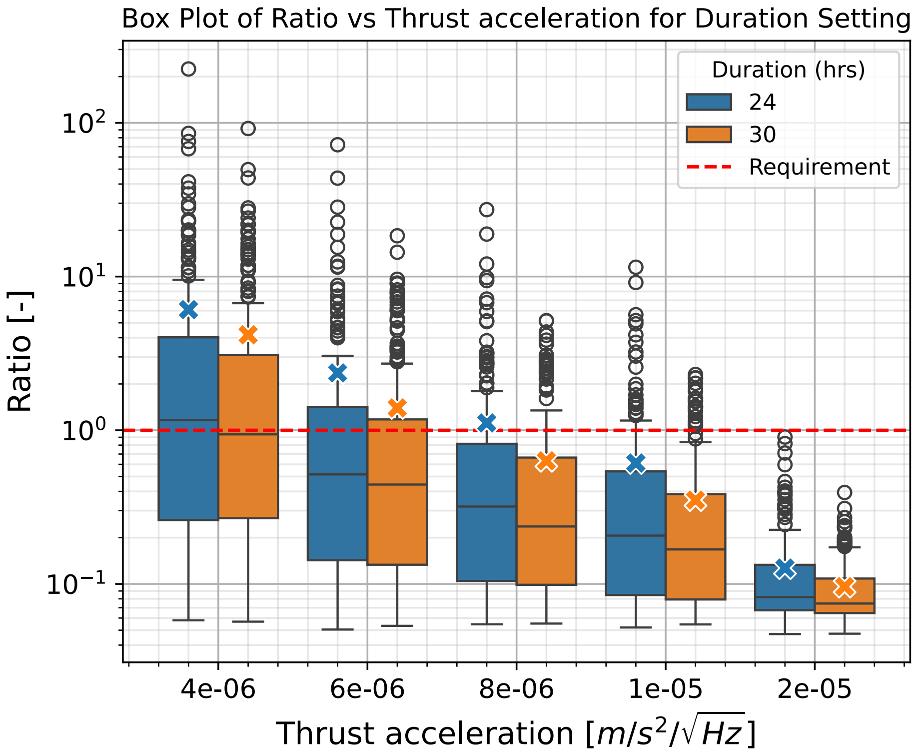

Figure 7.19: Box plot of Ratio vs Thrust for 24 and 30 hrs of shaking for Layout 3 placed on y-axis.

8

Conclusion and Recommendations

This chapter brings a conclusion to the study by answering the research questions in Section 8.1 based on the results presented in Chapter 7, as well as the recommendations for future work in Section 8.2.

8.1. Conclusion

This study aimed to support the accelerometer data calibration for the proposed NGGM mission, incorporating the lessons learnt from previous gravity missions. The development of a comprehensive calibration tool allowed the exploration of multiple accelerometer configurations at varying shaking signals to understand the factors influencing the calibration performance. The objective of this thesis was to answer the following research question:

To what extent can the shaking manoeuvres be used to calibrate the accelerometers by incorporating accurately the noise and error characteristics of the accelerometers and star trackers?

To achieve this, the following set of sub-questions was formulated. Each sub-question is addressed in the following paragraphs, leading to answering the main research question.

1. *What is a favourable configuration of accelerometer placement to retrieve non-gravitational acceleration along the laser's LoS?*

   The calibration of the data is best when the accelerometers are placed along the x-axis of the body-fixed frame (approximately in the along-track direction), followed by the z-axis, and the y-axis performs the worst. This is attributed to the presence of an angular rate of $-1.13\,\mathrm{mrad/s}$ about the y-axis (pitch rate) arising from the satellite's attitude following approximately an along-track pointing of its body-fixed x-axis. The presence of pitch rate boosts the centrifugal acceleration of the shaking manoeuvre for the x- and z-axis placed acceleration, contrary to the y-axis placement. Moreover, the x-axis performs better than the z-axis, even though the pitch rate effect is also felt for the radially placed accelerometers. Analysis of the relative non-gravitational measurement error $\epsilon_{ng,LoS,rel}$ for the same set of parameters revealed that the accelerometer placement makes no difference in the error signature, indicating that the along-track placement performance stems from the better estimation of parameters during calibration. Due to the electrode layout of the accelerometers, the along-track placed accelerometers get a signal boost due to the projection of the angular acceleration about the y-axis onto the z component of the linear acceleration. The radially placed accelerometers lack any projection of angular acceleration on the x component of the linear acceleration, leading to worse estimation relatively.

Having more accelerometers further aids the calibration. Layout 3 produces a lower median error ratio by ≈ 1.5 than Layout 2 due to the addition of common mode observations. However, the variability in the ratio is similar at lower thrust acceleration levels at $2 \times 10^{-6}\,\mathrm{m/s^2/\sqrt{Hz}}$ with a shaking duration of 24 hrs. Layout 4 outperforms the other layouts with a median lower by a factor of 4 to 6, and has little variability with the same shaking manoeuvre setting. A second pair of accelerometers provides common mode observations and an additional sensitivity to gravity gradients, centrifugal and Euler accelerations, which are lacking in Layout 3.

Finally, the inter-accelerometer length (distance between the accelerometers in a pair) has little effect on calibration with lengths tested between 0.4 to $0.8\,\mathrm{m}$. The ratio values are similar across all thrust levels, with no standout improvement for a particular length.

Due to the accommodation of the LTI assembly, only a y-axis placement might be possible for the accelerometers. Layout 3 allows us to modify the calculation of $\epsilon_{ng,LoS,rel}$ in science mode by accounting only for the central accelerometer to avoid the error amplification due to the off-centre placement of accelerometers. The calibration performance shows no improvement for the modified metric. On the contrary, the noise at higher frequencies is amplified. A thrust of at least $8 \times 10^{-6}\,\mathrm{m/s^2/\sqrt{Hz}}$ is required to have a chance of fulfilling the requirement with confidence. But the thrust falls outside the measurement range of the accelerometers. If an along-track configuration is considered, the racetrack configuration of the LTI system may have to be modified with longer optical tubes to accommodate the accelerometers in an already tight space, making the LTI system vulnerable to thermal effects.

2. *What shaking manoeuvre is optimal for data calibration?*

The lower frequency shaking improves the calibration quality as it is more stable across different seeds and is less prone to producing large ratios. It shows a lower variability due to the accumulation of a higher angular rate magnitude variation during shaking compared to the high-frequency signal. However, to compare the shaking frequency on similar grounds, the thrust acceleration is scaled during the low-frequency shaking signal generation to have the same magnitude variability in acceleration units for low- and high-frequency shaking. The thrust of the low-frequency ASD filter used to create the shaking signal must be scaled as it has a lower power due to a lower area under the signal than the high-frequency shaking ASD filter. This produces a similar magnitude variability of the acceleration shaking signal in the time domain, but also increases the angular rates of the shaking signal for low-frequency shaking.

Longer shaking durations improve the quality by adding more observations into the least squares problem. But, the rate of improvement slows down at higher shaking durations with the reduction of the square root of the ratio's median roughly following the $\sqrt{n}$ law. The discrepancy arises as the ratio is a derived parameter and follows a right-skewed distribution instead of a normal distribution.

A higher thrust acceleration improves the shaking quality by reducing the ratio values and variability across all settings. A high enough thrust acceleration, such as more than $4\times10^{-6}\,\mathrm{m/s^2/\sqrt{Hz}}$, gives more freedom to choose other variables such as the number of accelerometers, their placement in the body and the shaking duration of calibration but any acceleration higher than $\pm 6.4 \times 10^{-6}\,\mathrm{m\,s^{-2}}$ falls outside the measurement range of the accelereomters. Additionally, given the current thruster requirements and cold gas thrusters capability, a maximum of $2 \times 10^{-6}\,\mathrm{m/s^2/\sqrt{Hz}}$ is considered which is already at the limits of thrusters for fulfilling the $\epsilon_{ng,LoS,rel}$ requirement for Layout 3 placed on x-axis at 24 hrs of shaking duration. Any lower thrust or shaking duration would require switching to Layout 4.

3. *What is the effect of the shaking method on mission performance?*

   Assuming that 42 shaking manoeuvres are performed in the mission, Layout 3, with accelerometers placed on the x-axis, will consume at least $7\,\mathrm{kg}$ of fuel in total for a thrust of $2 \times 10^{-6}\,\mathrm{m/s^2/\sqrt{Hz}}$ and 24 hrs of shaking. Suppose the accelerometers must be placed on the y-axis due to accommodation constraints, a higher thrust is necessary with at least 24-30 hrs of shaking manoeuvres, consuming about $34\,\mathrm{kg}$ of fuel overall assuming that the accelerometers and thrusters are capable to achieve it. Any lower thrust or shaking duration to reduce fuel consumption would require opting for Layout 4 with four accelerometers. However, an additional accelerometer will add $1.5\,\mathrm{kg}$ to the satellite's mass and a power consumption of $2\,\mathrm{W}$. Although the derived estimates fall within the $100\,\mathrm{kg}$ fuel limit, a smart selection of configuration can help conserve fuel for other manoeuvres such as detumbling, orbit maintenance and laser acquisition, thus prolonging the mission lifetime beyond seven years. Although Layout 4 helps conserve fuel, the additional power consumption of $2\,\mathrm{W}$ may be detrimental depending upon the power budget. With the presence of the central accelerometer in Layout 3, the off-centre accelerometers can be switched off during science mode to reconstruct $\boldsymbol{a}_{ng}^{rcst}$ to conserve power.

Based on the current thruster requirements and hardware performance, an along-track placement of accelerometers with low-frequency shaking is necessary to achieve an acceptable level of calibration performance and fulfill the stipulated relative non-gravitational acceleration measurement error. If the along-track placement is impossible due to LTI accommodation, the thruster requirements and accelerometer characteristics must be revised to make the calibration more stable to random noise in the measured data.

Overall, calibrating accelerometer data with a shaking manoeuvre is a powerful technique that accounts for a comprehensive accelerometer model that other calibration techniques lack. It is an internal calibration technique that solely relies on the data recorded by the satellite's sensors on board, avoiding the reliance on generating a detailed satellite model and/or using external physical models of the atmosphere or Earth's gravitational field. However, the biases in the data cannot be estimated using this method. A hybrid calibration method combining the calibration via GPS-based orbit determination and calibration via shaking manoeuvre is required for a total calibration. The GPS-based orbit determination calibration uses a simple model of bias and scale factors for the accelerometer, where the scale factors can be supplied by the calibration via a shaking manoeuvre.

8.2. Recommendations

This report established a foundation to study the different shaking manoeuvres and configurations to aid the calibration of the proposed NGGM mission. Several points of interest require further investigation and refinement to address the limitations encountered in this study:

1. The ratio metric to assess the calibration performance is influenced by the window length selected in Welch's method to estimate the ASD, and the sampling frequency of the instrument. A different selection for them would result in a different spectrum. A metric which stays comparable across accelerometers with different sampling rates and window selection will help generalise the method to other missions.
2. The star-tracker and body-fixed frame are assumed to be aligned perfectly. A misalignment for future studies should be considered to study the effect of this error.
3. The orbit generation in this study is used only for the satellite's position w.r.t. Earth for

gravity gradients and attitude observations. The shaking signal generation is decoupled from the orbit simulation, assuming that any desired shaking signal can be generated given an ASD. There is no closed-loop dynamic system simulating a shaking where thruster limitations, such as slew and thruster command rates, are considered. Having chosen an optimal region of the shaking signal, the settings could be refined more appropriately, considering the thruster limitations. Furthermore, the attitude dynamics are not considered. It is assumed that the attitude control system can meet the needs of the shaking manoeuvre. Therefore a fully-coupled simulation between the satellite dynamics and desired shaking signal is recommended.

4. The study considers the ion thruster noise and thrust range requirements as the thrusters' noise and thrust range capabilities. Moreover, the cold gas thrusters are assumed to have similar noise and thrust magnitude capabilities (even higher thrust for y-axis placement of the accelerometers). The study should be refined once more information on the thrusters is available. This study considers the noise requirement of thrusters as the actual noise, which is a conservative estimate.
5. The shaking signal generation follows a similar production method as the noise of the sensors, that is, convolving a filter of desired ASD with white noise. However, in a real mission, the shaking signals are pseudo-random and pre-programmed into the flight computer. Therefore, the shaking signal generation should be made more deterministic once an optimal region of shaking settings is identified to run a comprehensive analysis on narrowing down the optimum while considering the recommendations of the previous point.
6. The orbit generation does not consider the effect of solar cycles on calibration performance. At high solar activity, the non-gravitational signal has a higher signature. While the satellite is assumed to be drag compensated in this study, the calibration performance should be assessed for an uncompensated high solar activity scenario.
7. Finally, the calibration tool works independently of the data generation tool. Therefore, the data generation tool can be tweaked according to different missions/applications. For future studies, more emphasis has to be placed on the data generation tool.

A

Linearization Tools

A.1. Linearization of an Inverse Matrix

During the derivation of observation equations, partials of the inverse of the calibration matrix $\boldsymbol{M}^{-1}$ w.r.t to the elements of the original matrix $\boldsymbol{M}$ are required, where $\boldsymbol{M} \approx \boldsymbol{I}$.

Let the calibration matrix be expressed as

$$\boldsymbol{M} = \boldsymbol{I} + \delta\boldsymbol{M} + \delta\delta\boldsymbol{M} \tag{A.1}$$

where $\boldsymbol{I} \gg \delta\boldsymbol{M} \gg \delta\delta\boldsymbol{M}$. Further, using a Neumann series, an inverse of a matrix can be written as

$$(\boldsymbol{I} - \boldsymbol{A})^{-1} = \boldsymbol{I} + \boldsymbol{A} + \boldsymbol{A}^2 + \boldsymbol{A}^3 + ... \tag{A.2}$$

Then the inverse of the calibration matrix is expressed as

$$\begin{aligned}
\boldsymbol{M}^{-1} &= (\boldsymbol{I} + \delta\boldsymbol{M} + \delta\delta\boldsymbol{M})^{-1} \\
&= (\boldsymbol{I} + \delta\boldsymbol{M} + \delta\delta\boldsymbol{M})^{-1}(\boldsymbol{I} + \delta\boldsymbol{M})(\boldsymbol{I} + \delta\boldsymbol{M})^{-1} \\
&= ((\boldsymbol{I} + \delta\boldsymbol{M})^{-1}(\boldsymbol{I} + \delta\boldsymbol{M} + \delta\delta\boldsymbol{M}))^{-1}(\boldsymbol{I} + \delta\boldsymbol{M})^{-1} \\
&= (\boldsymbol{I} + (\boldsymbol{I} + \delta\boldsymbol{M})^{-1}\delta\delta\boldsymbol{M})^{-1}(\boldsymbol{I} + \delta\boldsymbol{M})^{-1} \\
&= (\boldsymbol{I} - (\boldsymbol{I} + \delta\boldsymbol{M})^{-1}\delta\delta\boldsymbol{M} + O(((\boldsymbol{I} + \delta\boldsymbol{M})^{-1}\delta\delta\boldsymbol{M})^2))(\boldsymbol{I} + \delta\boldsymbol{M})^{-1} \\
&= (\boldsymbol{I} - (\boldsymbol{I} + \delta\boldsymbol{M})^{-1}\delta\delta\boldsymbol{M} + O(\delta\delta\boldsymbol{M}^2))(\boldsymbol{I} + \delta\boldsymbol{M})^{-1} \\
&= (\boldsymbol{I} + \delta\boldsymbol{M})^{-1} - (\boldsymbol{I} + \delta\boldsymbol{M})^{-1}\delta\delta\boldsymbol{M}(\boldsymbol{I} + \delta\boldsymbol{M})^{-1} + O(\delta\delta\boldsymbol{M}^2)
\end{aligned} \tag{A.3}$$

Consider matrix $\boldsymbol{M}$ as a function of $\delta\boldsymbol{M}$, $\boldsymbol{M}(\delta\boldsymbol{M}) = \boldsymbol{I} + \delta\boldsymbol{M}$. Expanding it using a Taylor series expansion, the linearized equation is

$$\boldsymbol{M}(\delta\boldsymbol{M}) = \boldsymbol{I} + \delta\boldsymbol{M}_0 + \delta\delta\boldsymbol{M}, \text{ where } \delta\delta\boldsymbol{M} = \delta\boldsymbol{M} - \delta\boldsymbol{M}_0 \tag{A.4}$$

The inverse $\boldsymbol{M}^{-1}$ is also a function of $\delta\boldsymbol{M}$ from Equation A.1 and can be expanded into a series using Equation A.3:

$$\boldsymbol{M}^{-1}(\delta\boldsymbol{M}) = (\boldsymbol{I} + \delta\boldsymbol{M}_0)^{-1} - (\boldsymbol{I} + \delta\boldsymbol{M}_0)^{-1}\delta\delta\boldsymbol{M}(\boldsymbol{I} + \delta\boldsymbol{M}_0)^{-1} \tag{A.5}$$

where $\delta\delta\boldsymbol{M} = \delta\boldsymbol{M} - \delta\boldsymbol{M}_0$ is the parameter update to the approximate value $\delta\boldsymbol{M}_0$. Only $(\boldsymbol{I} + \delta\boldsymbol{M}_0)^{-1}$ is relevant when calculating the inverse $\boldsymbol{M}^{-1}(\delta\boldsymbol{M}_0)$, and $(\boldsymbol{I} + \delta\boldsymbol{M}_0)^{-1}\delta\delta\boldsymbol{M}(\boldsymbol{I} + \delta\boldsymbol{M}_0)^{-1}$ is relevant for calculating the partials $\frac{\partial(\delta\boldsymbol{M}^{-1})}{\partial(\delta\boldsymbol{M})}$

A.2. Derivatives of Matrix Products

In many instances, partials of a matrix product $\boldsymbol{AXB}$ is required w.r.t. the parameter matrix $\boldsymbol{X}$. Consider a matrix product $\boldsymbol{C} = \boldsymbol{AXB}$.

The vectorization operation vec($\boldsymbol{C}$) stacks the columns of the matrix into one column vector $\boldsymbol{c}$

$$\boldsymbol{c} = \text{vec}(\boldsymbol{C}) = \text{vec}(\boldsymbol{AXB}) = (\boldsymbol{B}^T \otimes \boldsymbol{A})\boldsymbol{x} \tag{A.6}$$

where $\otimes$ is the Kronecker product. Thus, the derivative of $\boldsymbol{c}$ w.r.t to $\boldsymbol{x}$ is

$$\frac{\partial \boldsymbol{c}}{\partial \boldsymbol{x}} = \frac{(\boldsymbol{B}^T \otimes \boldsymbol{A})\boldsymbol{x}}{\partial \boldsymbol{x}} = (\boldsymbol{B}^T \otimes \boldsymbol{A}) \tag{A.7}$$

B

Linearized Equations

B.1. Differential mode

For the partials w.r.t. to the position offsets, $\boldsymbol{F}_d$ needs to be arranged differently. Let's look at the term $\delta\boldsymbol{r}_{d13}^T\boldsymbol{G}_n^T(\boldsymbol{H}_{c13} + \delta\delta\boldsymbol{M}_{c13})^T$ in Equation 5.42. For further convenience, define $\boldsymbol{U}_n = (\boldsymbol{H}_{c13} + \delta\delta\boldsymbol{M}_{c13})\boldsymbol{G}_n$. Then $\boldsymbol{F}_d$ can be written as

$$\begin{aligned}
\boldsymbol{F}_d &= ... + \begin{bmatrix} \delta\boldsymbol{r}_{d13}^T\boldsymbol{U}_1^T \\ \vdots \\ \delta\boldsymbol{r}_{d13}^T\boldsymbol{U}_N^T \end{bmatrix} + ... \\
&= ... + \begin{bmatrix} \delta\boldsymbol{r}_{d13}^T\text{col}(\boldsymbol{U}_1^T,1) & \delta\boldsymbol{r}_{d13}^T\text{col}(\boldsymbol{U}_1^T,2) & \delta\boldsymbol{r}_{d13}^T\text{col}(\boldsymbol{U}_1^T,3) \\ \vdots & \vdots & \vdots \\ \delta\boldsymbol{r}_{d13}^T\text{col}(\boldsymbol{U}_N^T,1) & \delta\boldsymbol{r}_{d13}^T\text{col}(\boldsymbol{U}_N^T,2) & \delta\boldsymbol{r}_{d13}^T\text{col}(\boldsymbol{U}_N^T,3) \end{bmatrix} + ... \qquad \text{(B.1)} \\
&= ... + \begin{bmatrix} \text{col}(\boldsymbol{U}_1^T,1)^T\delta\boldsymbol{r}_{d13} & \text{col}(\boldsymbol{U}_1^T,2)^T\delta\boldsymbol{r}_{d13} & \text{col}(\boldsymbol{U}_1^T,3)^T\delta\boldsymbol{r}_{d13} \\ \vdots & \vdots & \vdots \\ \text{col}(\boldsymbol{U}_N^T,1)^T\delta\boldsymbol{r}_{d13} & \text{col}(\boldsymbol{U}_N^T,2)^T\delta\boldsymbol{r}_{d13} & \text{col}(\boldsymbol{U}_N^T,3)^T\delta\boldsymbol{r}_{d13} \end{bmatrix} + ...
\end{aligned}$$

where col$(\boldsymbol{A}, n)$ returns the n-th column of a matrix A. Note that col$(\boldsymbol{A}^T, n) =$ row$(\boldsymbol{A}, n)^T$

$$
\begin{aligned}
\text{vec}(\boldsymbol{F}_d) &= ... + \text{vec}\left(\begin{bmatrix} \text{row}(\boldsymbol{U}_1,1)\delta\boldsymbol{r}_{d13} & \text{row}(\boldsymbol{U}_1,2)\delta\boldsymbol{r}_{d13} & \text{row}(\boldsymbol{U}_1,3)\delta\boldsymbol{r}_{d13} \\ \cdot & \cdot & \cdot \\ \cdot & \cdot & \cdot \\ \text{row}(\boldsymbol{U}_N,1)\delta\boldsymbol{r}_{d13} & \text{row}(\boldsymbol{U}_N,2)\delta\boldsymbol{r}_{d13} & \text{row}(\boldsymbol{U}_N,3)\delta\boldsymbol{r}_{d13} \end{bmatrix}\right) + ... \\
&= ... + \begin{bmatrix} \text{row}(\boldsymbol{U}_1,1) \\ \cdot \\ \cdot \\ \cdot \\ \text{row}(\boldsymbol{U}_N,1) \\ \text{row}(\boldsymbol{U}_1,2) \\ \cdot \\ \cdot \\ \text{row}(\boldsymbol{U}_N,2) \\ \text{row}(\boldsymbol{U}_1,3) \\ \cdot \\ \cdot \\ \text{row}(\boldsymbol{U}_N,3) \end{bmatrix} \delta\boldsymbol{r}_{d13} + ...,
\end{aligned}
\tag{B.2}
$$

Since

$$
\begin{aligned}
\text{row}(\boldsymbol{U}_n, r) &= \text{row}((\boldsymbol{H}_{c13} + \delta\delta\boldsymbol{M}_{c13})\boldsymbol{G}_n, r) \\
&= \text{row}((\boldsymbol{H}_{c13} + \delta\delta\boldsymbol{M}_{c13}, r)\boldsymbol{G}_n,
\end{aligned}
\tag{B.3}
$$

the partials w.r.t. $\delta\boldsymbol{r}_{d13}$ and $\delta\boldsymbol{r}_{c13}$

$$
\frac{\partial \text{vec}(\boldsymbol{F}_d)}{\partial(\delta\boldsymbol{r}_{d13})} = \begin{bmatrix} \text{row}(\boldsymbol{U}_1,1) \\ \cdot \\ \cdot \\ \text{row}(\boldsymbol{U}_N,1) \\ \text{row}(\boldsymbol{U}_1,2) \\ \cdot \\ \cdot \\ \text{row}(\boldsymbol{U}_N,2) \\ \text{row}(\boldsymbol{U}_1,3) \\ \cdot \\ \cdot \\ \text{row}(\boldsymbol{U}_N,3) \end{bmatrix} + ... = \begin{bmatrix} \text{row}(\boldsymbol{H}_{c13},1)\boldsymbol{G}_1 \\ \cdot \\ \cdot \\ \text{row}(\boldsymbol{H}_{c13},1)\boldsymbol{G}_N \\ \text{row}(\boldsymbol{H}_{c13},2)\boldsymbol{G}_1 \\ \cdot \\ \cdot \\ \text{row}(\boldsymbol{H}_{c13},2)\boldsymbol{G}_N \\ \text{row}(\boldsymbol{H}_{c13},3)\boldsymbol{G}_1 \\ \cdot \\ \cdot \\ \text{row}(\boldsymbol{H}_{c13},3)\boldsymbol{G}_N \\ \\ \end{bmatrix} + ...
\tag{B.4}
$$

$$\frac{\partial \text{vec}(\boldsymbol{F}_d)}{\partial(\delta \boldsymbol{r}_{c13})} = \begin{bmatrix} \text{row}(\boldsymbol{H}_{d13},1)\boldsymbol{G}_1 \\ . \\ . \\ \text{row}(\boldsymbol{H}_{d13},1)\boldsymbol{G}_N \\ \text{row}(\boldsymbol{H}_{d13},2)\boldsymbol{G}_1 \\ . \\ . \\ \text{row}(\boldsymbol{H}_{d13},2)\boldsymbol{G}_N \\ \text{row}(\boldsymbol{H}_{d13},3)\boldsymbol{G}_1 \\ . \\ . \\ \text{row}(\boldsymbol{H}_{d13},3)\boldsymbol{G}_N \\ \end{bmatrix} + ... \tag{B.5}$$

But this is just one part of the partials w.r.t. the position offsets. In Equation 5.42 the terms $\boldsymbol{K}_1(\boldsymbol{a}_1^{np} + \boldsymbol{G}\delta\boldsymbol{r}_1)^2$ and $\boldsymbol{K}_3(\boldsymbol{a}_3^{np} + \boldsymbol{G}\delta\boldsymbol{r}_3)^2$ depend on $\delta\boldsymbol{r}_1$ and $\delta\boldsymbol{r}_3$, respectively. Therefore, $\delta\boldsymbol{r}_1$ dependent term of $\boldsymbol{F}_d$ can be written as

$$\text{vec}(\boldsymbol{F}_d) = ... + \frac{1}{2}\text{vec}\left(\begin{bmatrix} . \\ . \\ ((\boldsymbol{a}_{1,n}^{np} + \boldsymbol{G}_n\delta\boldsymbol{r}_1)^2)^T \boldsymbol{K}_1^T \\ . \\ . \end{bmatrix}\right) + ... \tag{B.6}$$

Since $\boldsymbol{K}_1$ is a diagonal matrix, it can be simplified to

$$\text{vec}(\boldsymbol{F}_d) = ... + \frac{1}{2}\begin{bmatrix} . \\ . \\ (\boldsymbol{a}_{1x,n}^{np} + \text{row}(\boldsymbol{G}_n,1)\delta\boldsymbol{r}_1)^2 K_{1x} \\ . \\ . \\ (\boldsymbol{a}_{1y,n}^{np} + \text{row}(\boldsymbol{G}_n,2)\delta\boldsymbol{r}_1)^2 K_{1y} \\ . \\ . \\ (\boldsymbol{a}_{1z,n}^{np} + \text{row}(\boldsymbol{G}_n,3)\delta\boldsymbol{r}_1)^2 K_{1z} \\ . \\ . \\ \end{bmatrix} + ... \tag{B.7}$$

The partial w.r.t. $\delta\boldsymbol{r}_1$ is then

$$\frac{\partial \text{vec}(\boldsymbol{F}_d)}{\partial(\delta\boldsymbol{r}_1)} = \begin{bmatrix} \vdots \\ (\boldsymbol{a}^{np}_{1x,n} + \text{row}(\boldsymbol{G}_n,1)\delta\boldsymbol{r}_1)^2 K_{1x}\text{row}(\boldsymbol{G}_n,1) \\ \vdots \\ (\boldsymbol{a}^{np}_{1y,n} + \text{row}(\boldsymbol{G}_n,2)\delta\boldsymbol{r}_1)^2 K_{1y}\text{row}(\boldsymbol{G}_n,2) \\ \vdots \\ (\boldsymbol{a}^{np}_{1z,n} + \text{row}(\boldsymbol{G}_n,3)\delta\boldsymbol{r}_1)^2 K_{1z}\text{row}(\boldsymbol{G}_n,3) \\ \vdots \\ \end{bmatrix}. \tag{B.8}$$

Similarly, the partial w.r.t. $\delta\boldsymbol{r}_3$ is (note the sign difference)

$$\frac{\partial \text{vec}(\boldsymbol{F}_d)}{\partial(\delta\boldsymbol{r}_3)} = - \begin{bmatrix} \vdots \\ (\boldsymbol{a}^{np}_{3x,n} + \text{row}(\boldsymbol{G}_n,1)\delta\boldsymbol{r}_3)^2 K_{3x}\text{row}(\boldsymbol{G}_n,1) \\ \vdots \\ (\boldsymbol{a}^{np}_{3y,n} + \text{row}(\boldsymbol{G}_n,2)\delta\boldsymbol{r}_3)^2 K_{3y}\text{row}(\boldsymbol{G}_n,2) \\ \vdots \\ (\boldsymbol{a}^{np}_{3z,n} + \text{row}(\boldsymbol{G}_n,3)\delta\boldsymbol{r}_3)^2 K_{3z}\text{row}(\boldsymbol{G}_n,3) \\ \vdots \\ \end{bmatrix}. \tag{B.9}$$

For any function $\boldsymbol{f}$, the partial derivative w.r.t. $\delta\boldsymbol{r}_{c13}$ can be written as

$$\frac{\partial \boldsymbol{f}}{\partial(\delta\boldsymbol{r}_{c13})} = \frac{\partial \boldsymbol{f}}{\partial(\delta\boldsymbol{r}_1)} \cdot \frac{\partial(\delta\boldsymbol{r}_1)}{\partial(\delta\boldsymbol{r}_{c13})} + \frac{\partial \boldsymbol{f}}{\partial(\delta\boldsymbol{r}_3)} \cdot \frac{\partial(\delta\boldsymbol{r}_3)}{\partial(\delta\boldsymbol{r}_{c13})} \tag{B.10}$$

Since $\delta\boldsymbol{r}_1 = \delta\boldsymbol{r}_{c13} + \delta\boldsymbol{r}_{d13}$ and $\delta\boldsymbol{r}_3 = \delta\boldsymbol{r}_{c13} - \delta\boldsymbol{r}_{d13}$

$$\frac{\partial(\delta\boldsymbol{r}_1)}{\partial(\delta\boldsymbol{r}_{c13})} = \boldsymbol{I}, \frac{\partial(\delta\boldsymbol{r}_1)}{\partial(\delta\boldsymbol{r}_{d13})} = \boldsymbol{I}, \qquad \frac{\partial(\delta\boldsymbol{r}_3)}{\partial(\delta\boldsymbol{r}_{c13})} = \boldsymbol{I}, \frac{\partial(\delta\boldsymbol{r}_3)}{\partial(\delta\boldsymbol{r}_{d13})} = -\boldsymbol{I} \tag{B.11}$$

Therefore,

$$\frac{\partial \boldsymbol{f}}{\partial(\delta\boldsymbol{r}_{c13})} = \frac{\partial \boldsymbol{f}}{\partial(\delta\boldsymbol{r}_1)} + \frac{\partial \boldsymbol{f}}{\partial(\delta\boldsymbol{r}_3)}, \tag{B.12}$$

and similarly

$$\frac{\partial \boldsymbol{f}}{\partial(\delta\boldsymbol{r}_{d13})} = \frac{\partial \boldsymbol{f}}{\partial(\delta\boldsymbol{r}_1)} - \frac{\partial \boldsymbol{f}}{\partial(\delta\boldsymbol{r}_3)}. \tag{B.13}$$

Now, the partials in Equations (B.8) and (B.9) can be combined with partials in Equations (B.4) and (B.5):

$$\begin{aligned}\frac{\partial \text{vec}(\boldsymbol{F}_d)}{\partial(\delta \boldsymbol{r}_{d13})} = & \begin{bmatrix} \vdots \\ \text{row}(\boldsymbol{H}_{c13},1)\boldsymbol{G}_n \\ \vdots \\ \text{row}(\boldsymbol{H}_{c13},2)\boldsymbol{G}_n \\ \vdots \\ \text{row}(\boldsymbol{H}_{c13},3)\boldsymbol{G}_n \\ \vdots \end{bmatrix} + \begin{bmatrix} \vdots \\ (\boldsymbol{a}^{np}_{1x,n} + \text{row}(\boldsymbol{G}_n,1)\delta\boldsymbol{r}_1)^2 K_{1x}\text{row}(\boldsymbol{G}_n,1) \\ \vdots \\ (\boldsymbol{a}^{np}_{1y,n} + \text{row}(\boldsymbol{G}_n,2)\delta\boldsymbol{r}_1)^2 K_{1y}\text{row}(\boldsymbol{G}_n,2) \\ \vdots \\ (\boldsymbol{a}^{np}_{1z,n} + \text{row}(\boldsymbol{G}_n,3)\delta\boldsymbol{r}_1)^2 K_{1z}\text{row}(\boldsymbol{G}_n,3) \\ \vdots \end{bmatrix} \\ & + \begin{bmatrix} \vdots \\ (\boldsymbol{a}^{np}_{3x,n} + \text{row}(\boldsymbol{G}_n,1)\delta\boldsymbol{r}_3)^2 K_{3x}\text{row}(\boldsymbol{G}_n,1) \\ \vdots \\ (\boldsymbol{a}^{np}_{3y,n} + \text{row}(\boldsymbol{G}_n,2)\delta\boldsymbol{r}_3)^2 K_{3y}\text{row}(\boldsymbol{G}_n,2) \\ \vdots \\ (\boldsymbol{a}^{np}_{3z,n} + \text{row}(\boldsymbol{G}_n,3)\delta\boldsymbol{r}_3)^2 K_{3z}\text{row}(\boldsymbol{G}_n,3) \\ \vdots \end{bmatrix}, \end{aligned} \tag{B.14}$$

$$\begin{aligned}\frac{\partial \text{vec}(\boldsymbol{F}_d)}{\partial(\delta \boldsymbol{r}_{c13})} = & \begin{bmatrix} \vdots \\ \text{row}(\boldsymbol{H}_{d13},1)\boldsymbol{G}_n \\ \vdots \\ \text{row}(\boldsymbol{H}_{d13},2)\boldsymbol{G}_n \\ \vdots \\ \text{row}(\boldsymbol{H}_{d13},3)\boldsymbol{G}_n \\ \vdots \end{bmatrix} + \begin{bmatrix} \vdots \\ (\boldsymbol{a}^{np}_{1x,n} + \text{row}(\boldsymbol{G}_n,1)\delta\boldsymbol{r}_1)^2 K_{1x}\text{row}(\boldsymbol{G}_n,1) \\ \vdots \\ (\boldsymbol{a}^{np}_{1y,n} + \text{row}(\boldsymbol{G}_n,2)\delta\boldsymbol{r}_1)^2 K_{1y}\text{row}(\boldsymbol{G}_n,2) \\ \vdots \\ (\boldsymbol{a}^{np}_{1z,n} + \text{row}(\boldsymbol{G}_n,3)\delta\boldsymbol{r}_1)^2 K_{1z}\text{row}(\boldsymbol{G}_n,3) \\ \vdots \end{bmatrix} \\ & - \begin{bmatrix} \vdots \\ (\boldsymbol{a}^{np}_{3x,n} + \text{row}(\boldsymbol{G}_n,1)\delta\boldsymbol{r}_3)^2 K_{3x}\text{row}(\boldsymbol{G}_n,1) \\ \vdots \\ (\boldsymbol{a}^{np}_{3y,n} + \text{row}(\boldsymbol{G}_n,2)\delta\boldsymbol{r}_3)^2 K_{3y}\text{row}(\boldsymbol{G}_n,2) \\ \vdots \\ (\boldsymbol{a}^{np}_{3z,n} + \text{row}(\boldsymbol{G}_n,3)\delta\boldsymbol{r}_3)^2 K_{3z}\text{row}(\boldsymbol{G}_n,3) \\ \vdots \end{bmatrix}. \end{aligned} \tag{B.15}$$

B.2. Common mode

First, the offset $\delta \boldsymbol{r}_{d13}$ is looked at:

$$\boldsymbol{F}_c = ... + \begin{bmatrix} \vdots \\ \delta \boldsymbol{r}_{d13}^T \boldsymbol{G}_n^T \boldsymbol{M}_{d13}^T (\boldsymbol{H}_{c13}^{-T} \delta\delta \boldsymbol{M}_{c13}^T \boldsymbol{H}_{c13}^{-T} - \boldsymbol{H}_{c13}^{-T}) \\ \vdots \end{bmatrix} + ... \tag{B.16}$$

As derived during linearization of differential mode equations

$$\frac{\partial \text{vec}\left(\begin{bmatrix} \vdots \\ \boldsymbol{x}^T \boldsymbol{A}_n^T \\ \vdots \end{bmatrix}\right)}{\partial \boldsymbol{x}} = \begin{bmatrix} \vdots \\ \text{row}(\boldsymbol{A}_n, 1) \\ \vdots \\ \text{row}(\boldsymbol{A}_n, 2) \\ \vdots \end{bmatrix}, \tag{B.17}$$

the partial w.r.t.. $\delta \boldsymbol{r}_{d13}$ is

$$\frac{\partial \text{vec}(\boldsymbol{F}_c)}{\partial (\delta \boldsymbol{r}_{d13})} = -\begin{bmatrix} \vdots \\ \text{row}(\boldsymbol{H}_{c13}^{-1} \boldsymbol{M}_{d13} \boldsymbol{G}_n, 1) \\ \vdots \\ \text{row}(\boldsymbol{H}_{c13}^{-1} \boldsymbol{M}_{d13} \boldsymbol{G}_n, 2) \\ \vdots \\ \text{row}(\boldsymbol{H}_{c13}^{-1} \boldsymbol{M}_{d13} \boldsymbol{G}_n, 1) \\ \vdots \end{bmatrix}, \tag{B.18}$$

Second, consider the offset $\delta \boldsymbol{r}_{c13}$:

$$\boldsymbol{F}_c = ... - \begin{bmatrix} \vdots \\ (\delta \boldsymbol{r}_{c13} - \delta \boldsymbol{r}_2)^T \boldsymbol{G}_n^T \\ \vdots \end{bmatrix}. \tag{B.19}$$

Using Equation (B.17), the partial is

$$\frac{\partial \text{vec}(\boldsymbol{F}_c)}{\partial(\delta \boldsymbol{r}_{c13})} = - \begin{bmatrix} . \\ . \\ \text{row}(\boldsymbol{G}_n,1) \\ . \\ . \\ \text{row}(\boldsymbol{G}_n,2) \\ . \\ . \\ \text{row}(\boldsymbol{G}_n,3) \\ . \\ . \end{bmatrix} . \tag{B.20}$$

The partial w.r.t. offsets $\delta \boldsymbol{r}_1$ and $\delta \boldsymbol{r}_3$ are still to be derived:

$$\begin{aligned} \boldsymbol{F}_c = ... - \frac{1}{2} & \begin{bmatrix} . \\ . \\ ((\boldsymbol{a}^{np}_{1,n} + \boldsymbol{G}_n \delta \boldsymbol{r}_1)^2)^T \boldsymbol{K}_1 (\boldsymbol{H}^{-T}_{c13} - \boldsymbol{H}^{-T}_{c13} \delta\delta \boldsymbol{M}^T_{c13} \delta\delta \boldsymbol{H}^{-T}_{c13}) \\ . \\ . \end{bmatrix} \\ - \frac{1}{2} & \begin{bmatrix} . \\ . \\ ((\boldsymbol{a}^{np}_{3,n} + \boldsymbol{G}_n \delta \boldsymbol{r}_3)^2)^T \boldsymbol{K}_3 (\boldsymbol{H}^{-T}_{c13} - \boldsymbol{H}^{-T}_{c13} \delta\delta \boldsymbol{M}^T_{c13} \delta\delta \boldsymbol{H}^{-T}_{c13}) \\ . \\ . \end{bmatrix} + ... \\ ... + \frac{1}{2} & \begin{bmatrix} . \\ . \\ ((\boldsymbol{a}^{np}_{2,n} + \boldsymbol{G}_n \delta \boldsymbol{r}_2)^2)^T \boldsymbol{K}_2 (\boldsymbol{H}_2^{-T} - \boldsymbol{H}_2^{-T} \delta\delta \boldsymbol{M}^T_2 \delta\delta \boldsymbol{H}_2^{-T}) \\ . \\ . \end{bmatrix} . \end{aligned} \tag{B.21}$$

The above equation is of the form

$$\text{vec}(\boldsymbol{F}_c) = \text{vec}\left(\begin{bmatrix} . \\ . \\ ((\boldsymbol{a}_n + \boldsymbol{A}_n \boldsymbol{x})^2)^T \boldsymbol{B} \\ . \\ . \end{bmatrix} \right) = \begin{bmatrix} . \\ . \\ ((\boldsymbol{a}_n + \boldsymbol{A}_n \boldsymbol{x})^2)^T \text{col}(\boldsymbol{B},1) \\ . \\ . \\ ((\boldsymbol{a}_n + \boldsymbol{A}_n \boldsymbol{x})^2)^T \text{col}(\boldsymbol{B},2) \\ . \\ . \\ ((\boldsymbol{a}_n + \boldsymbol{A}_n \boldsymbol{x})^2)^T \text{col}(\boldsymbol{B},3) \\ . \\ . \end{bmatrix} . \tag{B.22}$$

Then, the partial of this equation is

$$\frac{\partial \text{vec}(\boldsymbol{F}_c)}{\partial(\boldsymbol{x})} = 2\begin{bmatrix} \vdots & & \vdots \\ (\boldsymbol{a}_n + \boldsymbol{A}_n\boldsymbol{x})^T \text{col}(\boldsymbol{A}_n,1) \circ \text{col}(\boldsymbol{B},1) & \dots & (\boldsymbol{a}_n + \boldsymbol{A}_n\boldsymbol{x})^T \text{col}(\boldsymbol{A}_n,3) \circ \text{col}(\boldsymbol{B},1) \\ \vdots & & \vdots \\ (\boldsymbol{a}_n + \boldsymbol{A}_n\boldsymbol{x})^T \text{col}(\boldsymbol{A}_n,1) \circ \text{col}(\boldsymbol{B},2) & \dots & (\boldsymbol{a}_n + \boldsymbol{A}_n\boldsymbol{x})^T \text{col}(\boldsymbol{A}_n,3) \circ \text{col}(\boldsymbol{B},2) \\ \vdots & & \vdots \\ (\boldsymbol{a}_n + \boldsymbol{A}_n\boldsymbol{x})^T \text{col}(\boldsymbol{A}_n,1) \circ \text{col}(\boldsymbol{B},3) & \dots & (\boldsymbol{a}_n + \boldsymbol{A}_n\boldsymbol{x})^T \text{col}(\boldsymbol{A}_n,3) \circ \text{col}(\boldsymbol{B},3) \\ \vdots & & \vdots \end{bmatrix}, \tag{B.23}$$

where $\circ$ denotes element-wise multiplication. Using Equation (B.23), the partials are

$$\frac{\partial \text{vec}(\boldsymbol{F}_c)}{\partial(\delta\boldsymbol{r}_1)} =$$

$$-\begin{bmatrix} \vdots & & \vdots \\ (\boldsymbol{a}_{1,n}^{np} + \boldsymbol{G}_n\delta\boldsymbol{r}_1)^T \text{col}(\boldsymbol{G}_n,1) \circ \text{col}(\boldsymbol{K}_1\boldsymbol{H}_{c13}^{-T},1) & \dots & (\boldsymbol{a}_{1,n}^{np} + \boldsymbol{G}_n\delta\boldsymbol{r}_1)^T \text{col}(\boldsymbol{G}_n,3) \circ \text{col}(\boldsymbol{K}_1\boldsymbol{H}_{c13}^{-T},1) \\ \vdots & & \vdots \\ (\boldsymbol{a}_{1,n}^{np} + \boldsymbol{G}_n\delta\boldsymbol{r}_1)^T \text{col}(\boldsymbol{G}_n,1) \circ \text{col}(\boldsymbol{K}_1\boldsymbol{H}_{c13}^{-T},2) & \dots & (\boldsymbol{a}_{1,n}^{np} + \boldsymbol{G}_n\delta\boldsymbol{r}_1)^T \text{col}(\boldsymbol{G}_n,3) \circ \text{col}(\boldsymbol{K}_1\boldsymbol{H}_{c13}^{-T},2) \\ \vdots & & \vdots \\ (\boldsymbol{a}_{1,n}^{np} + \boldsymbol{G}_n\delta\boldsymbol{r}_1)^T \text{col}(\boldsymbol{G}_n,1) \circ \text{col}(\boldsymbol{K}_1\boldsymbol{H}_{c13}^{-T},3) & \dots & (\boldsymbol{a}_{1,n}^{np} + \boldsymbol{G}_n\delta\boldsymbol{r}_1)^T \text{col}(\boldsymbol{G}_n,3) \circ \text{col}(\boldsymbol{K}_1\boldsymbol{H}_{c13}^{-T},3) \\ \vdots & & \vdots \end{bmatrix}, \tag{B.24}$$

$$\frac{\partial \text{vec}(\boldsymbol{F}_c)}{\partial(\delta\boldsymbol{r}_3)} =$$

$$-\begin{bmatrix} \vdots & & \vdots \\ (\boldsymbol{a}_{3,n}^{np} + \boldsymbol{G}_n\delta\boldsymbol{r}_3)^T \text{col}(\boldsymbol{G}_n,1) \circ \text{col}(\boldsymbol{K}_3\boldsymbol{H}_{c13}^{-T},1) & \dots & (\boldsymbol{a}_{3,n}^{np} + \boldsymbol{G}_n\delta\boldsymbol{r}_3)^T \text{col}(\boldsymbol{G}_n,3) \circ \text{col}(\boldsymbol{K}_3\boldsymbol{H}_{c13}^{-T},1) \\ \vdots & & \vdots \\ (\boldsymbol{a}_{3,n}^{np} + \boldsymbol{G}_n\delta\boldsymbol{r}_3)^T \text{col}(\boldsymbol{G}_n,1) \circ \text{col}(\boldsymbol{K}_3\boldsymbol{H}_{c13}^{-T},2) & \dots & (\boldsymbol{a}_{3,n}^{np} + \boldsymbol{G}_n\delta\boldsymbol{r}_3)^T \text{col}(\boldsymbol{G}_n,3) \circ \text{col}(\boldsymbol{K}_3\boldsymbol{H}_{c13}^{-T},2) \\ \vdots & & \vdots \\ (\boldsymbol{a}_{3,n}^{np} + \boldsymbol{G}_n\delta\boldsymbol{r}_3)^T \text{col}(\boldsymbol{G}_n,1) \circ \text{col}(\boldsymbol{K}_3\boldsymbol{H}_{c13}^{-T},3) & \dots & (\boldsymbol{a}_{3,n}^{np} + \boldsymbol{G}_n\delta\boldsymbol{r}_3)^T \text{col}(\boldsymbol{G}_n,3) \circ \text{col}(\boldsymbol{K}_3\boldsymbol{H}_{c13}^{-T},3) \\ \vdots & & \vdots \end{bmatrix}. \tag{B.25}$$

$\delta\boldsymbol{r}_2$ is assumed to be zero; thus, its partials are not required. Finally, using Equations (B.12) and (B.13), the partials can be combined to arrive at the final form:

$$
\begin{aligned}
&\frac{\partial \text{vec}(\boldsymbol{F}_c)}{\partial(\delta \boldsymbol{r}_{d13})} = \\
&-\begin{bmatrix}
\vdots & & \vdots \\
(\boldsymbol{a}_{1,n}^{np} + \boldsymbol{G}_n \delta \boldsymbol{r}_1)^T \text{col}(\boldsymbol{G}_n,1) \circ \text{col}(\boldsymbol{K}_1 \boldsymbol{H}_{c13}^{-T},1) & \dots & (\boldsymbol{a}_{1,n}^{np} + \boldsymbol{G}_n \delta \boldsymbol{r}_1)^T \text{col}(\boldsymbol{G}_n,3) \circ \text{col}(\boldsymbol{K}_1 \boldsymbol{H}_{c13}^{-T},1) \\
\vdots & & \vdots \\
(\boldsymbol{a}_{1,n}^{np} + \boldsymbol{G}_n \delta \boldsymbol{r}_1)^T \text{col}(\boldsymbol{G}_n,1) \circ \text{col}(\boldsymbol{K}_1 \boldsymbol{H}_{c13}^{-T},2) & \dots & (\boldsymbol{a}_{1,n}^{np} + \boldsymbol{G}_n \delta \boldsymbol{r}_1)^T \text{col}(\boldsymbol{G}_n,3) \circ \text{col}(\boldsymbol{K}_1 \boldsymbol{H}_{c13}^{-T},2) \\
\vdots & & \vdots \\
(\boldsymbol{a}_{1,n}^{np} + \boldsymbol{G}_n \delta \boldsymbol{r}_1)^T \text{col}(\boldsymbol{G}_n,1) \circ \text{col}(\boldsymbol{K}_1 \boldsymbol{H}_{c13}^{-T},3) & \dots & (\boldsymbol{a}_{1,n}^{np} + \boldsymbol{G}_n \delta \boldsymbol{r}_1)^T \text{col}(\boldsymbol{G}_n,3) \circ \text{col}(\boldsymbol{K}_1 \boldsymbol{H}_{c13}^{-T},3) \\
\vdots & & \vdots
\end{bmatrix} \\
&+\begin{bmatrix}
\vdots & & \vdots \\
(\boldsymbol{a}_{3,n}^{np} + \boldsymbol{G}_n \delta \boldsymbol{r}_3)^T \text{col}(\boldsymbol{G}_n,1) \circ \text{col}(\boldsymbol{K}_3 \boldsymbol{H}_{c13}^{-T},1) & \dots & (\boldsymbol{a}_{3,n}^{np} + \boldsymbol{G}_n \delta \boldsymbol{r}_3)^T \text{col}(\boldsymbol{G}_n,3) \circ \text{col}(\boldsymbol{K}_3 \boldsymbol{H}_{c13}^{-T},1) \\
\vdots & & \vdots \\
(\boldsymbol{a}_{3,n}^{np} + \boldsymbol{G}_n \delta \boldsymbol{r}_3)^T \text{col}(\boldsymbol{G}_n,1) \circ \text{col}(\boldsymbol{K}_3 \boldsymbol{H}_{c13}^{-T},2) & \dots & (\boldsymbol{a}_{3,n}^{np} + \boldsymbol{G}_n \delta \boldsymbol{r}_3)^T \text{col}(\boldsymbol{G}_n,3) \circ \text{col}(\boldsymbol{K}_3 \boldsymbol{H}_{c13}^{-T},2) \\
\vdots & & \vdots \\
(\boldsymbol{a}_{3,n}^{np} + \boldsymbol{G}_n \delta \boldsymbol{r}_3)^T \text{col}(\boldsymbol{G}_n,1) \circ \text{col}(\boldsymbol{K}_3 \boldsymbol{H}_{c13}^{-T},3) & \dots & (\boldsymbol{a}_{3,n}^{np} + \boldsymbol{G}_n \delta \boldsymbol{r}_3)^T \text{col}(\boldsymbol{G}_n,3) \circ \text{col}(\boldsymbol{K}_3 \boldsymbol{H}_{c13}^{-T},3) \\
\vdots & & \vdots
\end{bmatrix} \\
&-\begin{bmatrix}
\vdots \\
\text{row}(\boldsymbol{H}_{c13}^{-1} \boldsymbol{M}_{d13} \boldsymbol{G}_n,1) \\
\vdots \\
\text{row}(\boldsymbol{H}_{c13}^{-1} \boldsymbol{M}_{d13} \boldsymbol{G}_n,2) \\
\vdots \\
\text{row}(\boldsymbol{H}_{c13}^{-1} \boldsymbol{M}_{d13} \boldsymbol{G}_n,1) \\
\vdots
\end{bmatrix},
\end{aligned}
\tag{B.26}
$$

$$
\begin{aligned}
&\frac{\partial \text{vec}(\boldsymbol{F}_c)}{\partial(\delta \boldsymbol{r}_{c13})} = \\
&-\begin{bmatrix}
\vdots & & \vdots \\
(\boldsymbol{a}_{1,n}^{np} + \boldsymbol{G}_n \delta \boldsymbol{r}_1)^T \text{col}(\boldsymbol{G}_n,1) \circ \text{col}(\boldsymbol{K}_1 \boldsymbol{H}_{c13}^{-T},1) & \dots & (\boldsymbol{a}_{1,n}^{np} + \boldsymbol{G}_n \delta \boldsymbol{r}_1)^T \text{col}(\boldsymbol{G}_n,3) \circ \text{col}(\boldsymbol{K}_1 \boldsymbol{H}_{c13}^{-T},1) \\
\vdots & & \vdots \\
(\boldsymbol{a}_{1,n}^{np} + \boldsymbol{G}_n \delta \boldsymbol{r}_1)^T \text{col}(\boldsymbol{G}_n,1) \circ \text{col}(\boldsymbol{K}_1 \boldsymbol{H}_{c13}^{-T},2) & \dots & (\boldsymbol{a}_{1,n}^{np} + \boldsymbol{G}_n \delta \boldsymbol{r}_1)^T \text{col}(\boldsymbol{G}_n,3) \circ \text{col}(\boldsymbol{K}_1 \boldsymbol{H}_{c13}^{-T},2) \\
\vdots & & \vdots \\
(\boldsymbol{a}_{1,n}^{np} + \boldsymbol{G}_n \delta \boldsymbol{r}_1)^T \text{col}(\boldsymbol{G}_n,1) \circ \text{col}(\boldsymbol{K}_1 \boldsymbol{H}_{c13}^{-T},3) & \dots & (\boldsymbol{a}_{1,n}^{np} + \boldsymbol{G}_n \delta \boldsymbol{r}_1)^T \text{col}(\boldsymbol{G}_n,3) \circ \text{col}(\boldsymbol{K}_1 \boldsymbol{H}_{c13}^{-T},3) \\
\vdots & & \vdots
\end{bmatrix} \\
&-\begin{bmatrix}
\vdots & & \vdots \\
(\boldsymbol{a}_{3,n}^{np} + \boldsymbol{G}_n \delta \boldsymbol{r}_3)^T \text{col}(\boldsymbol{G}_n,1) \circ \text{col}(\boldsymbol{K}_3 \boldsymbol{H}_{c13}^{-T},1) & \dots & (\boldsymbol{a}_{3,n}^{np} + \boldsymbol{G}_n \delta \boldsymbol{r}_3)^T \text{col}(\boldsymbol{G}_n,3) \circ \text{col}(\boldsymbol{K}_3 \boldsymbol{H}_{c13}^{-T},1) \\
\vdots & & \vdots \\
(\boldsymbol{a}_{3,n}^{np} + \boldsymbol{G}_n \delta \boldsymbol{r}_3)^T \text{col}(\boldsymbol{G}_n,1) \circ \text{col}(\boldsymbol{K}_3 \boldsymbol{H}_{c13}^{-T},2) & \dots & (\boldsymbol{a}_{3,n}^{np} + \boldsymbol{G}_n \delta \boldsymbol{r}_3)^T \text{col}(\boldsymbol{G}_n,3) \circ \text{col}(\boldsymbol{K}_3 \boldsymbol{H}_{c13}^{-T},2) \\
\vdots & & \vdots \\
(\boldsymbol{a}_{3,n}^{np} + \boldsymbol{G}_n \delta \boldsymbol{r}_3)^T \text{col}(\boldsymbol{G}_n,1) \circ \text{col}(\boldsymbol{K}_3 \boldsymbol{H}_{c13}^{-T},3) & \dots & (\boldsymbol{a}_{3,n}^{np} + \boldsymbol{G}_n \delta \boldsymbol{r}_3)^T \text{col}(\boldsymbol{G}_n,3) \circ \text{col}(\boldsymbol{K}_3 \boldsymbol{H}_{c13}^{-T},3) \\
\vdots & & \vdots
\end{bmatrix} \qquad \text{(B.27)} \\
&-\begin{bmatrix}
\vdots \\
\text{row}(\boldsymbol{G}_n,1) \\
\vdots \\
\text{row}(\boldsymbol{G}_n,2) \\
\vdots \\
\text{row}(\boldsymbol{G}_n,3) \\
\vdots
\end{bmatrix}.
\end{aligned}
$$

C

Planning

Figure C.1 shows the work breakdown structure to aid the research by giving a hierarchical view of the tasks in each phase of the thesis. It provides a framework to list down the major activities and break them into smaller tasks. Based on the work breakdown structure, a Gantt chart was proposed to keep track of the timeline highlighted by Figures C.2 to C.4.

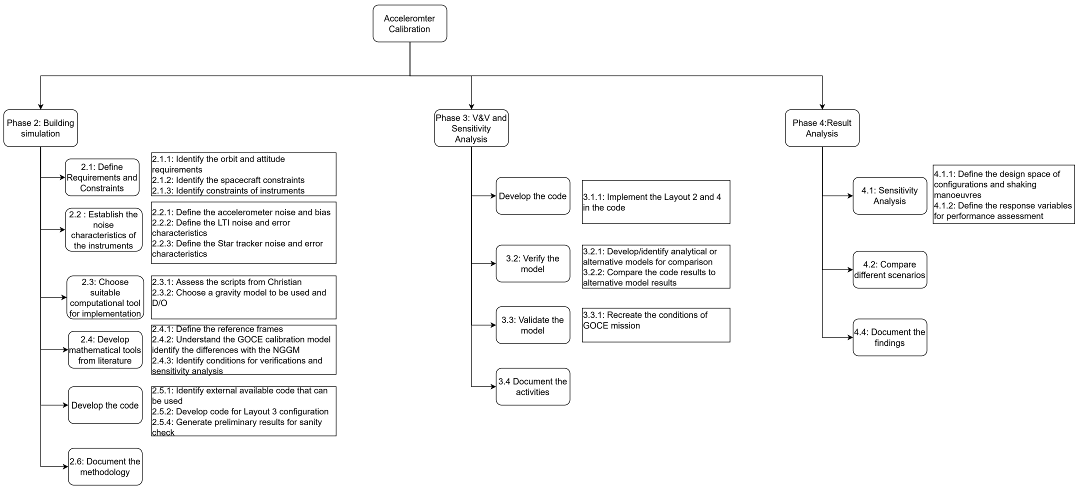

Figure C.1: Work breakdown structure

Figure C.2 shows the initial plan of the thesis after the literature review. The months of July and August were dedicated to developing the base methodology with Layout 3, y-axis placement, since it is the method detailed in the report. The mid-term review was planned to be in the last week of September. A total of six weeks of holidays were planned with two weeks in August, two after mid-term, and two weeks during the winter break.

Figure C.3 then shows the updated plan after the mid-term review. The mid-term review was delayed by three weeks. The delay was due to an additional two weeks of holidays taken in August, one of which was not planned due to medical reasons. An additional week was requested as I struggled with the implementation of the methodology due to code bugs. The two-week holiday after the mid-term was cut short to one week. The month of November was dedicated to the implementation of the other layouts in the methodology and the verification of them.

Figure C.4 shows the final schedule that resulted towards the end of the thesis. An additional week was holiday was added in December again due to medical reasons. The start of the sensitivity analysis was delayed by one week due to trouble with the implementation of other layouts and coding errors, which delayed the verification and validation. The results phase was tweaked to be fused with sensitivity analysis as the objective of the thesis was modified from finding a single best optimal solution to an exploratory study where a region of shaking manoeuvres was presented, which would be necessary for data calibration, given the physical constraints. One additional week was requested in the month of February, as I went off track in the month of January to understand and implement the factorial design method for sensitivity analysis, which eventually was not applicable for the number of combinations at hand due to multiple seed simulations.

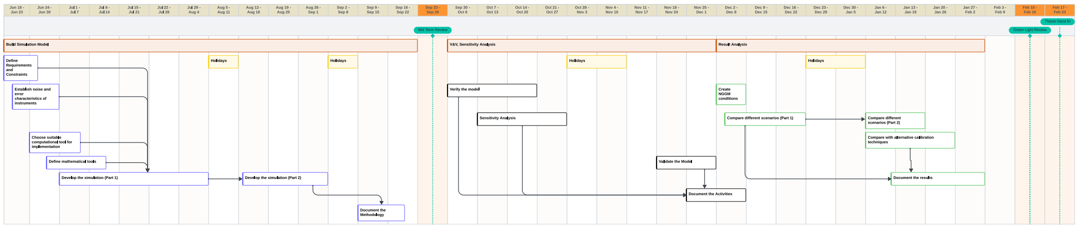

Figure C.2: Initial Plan.

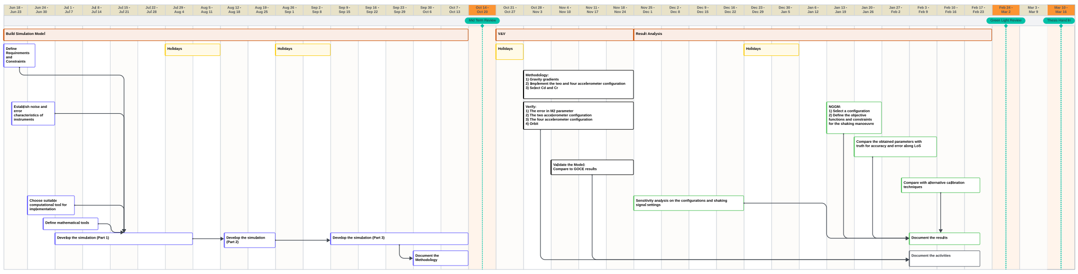

Figure C.3: Revised plan after mid-term review.

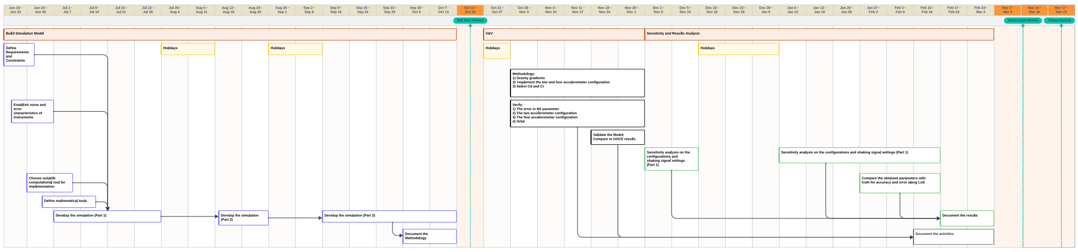

Figure C.4: Final schedule at the end of the thesis.

References

Bock, H., Jäggi, A., Meyer, U., Visser, P., Van Den IJssel, J., Van Helleputte, T., Heinze, M., & Hugentobler, U. (2011). GPS-derived orbits for the GOCE satellite. *Journal of Geodesy*, *85*(11), 807–818. https://doi.org/10.1007/s00190-011-0484-9

Bock, Y., & Melgar, D. (2016). Physical applications of GPS geodesy: A review. *Reports on Progress in Physics*, *79*(10), 106801. https://doi.org/10.1088/0034-4885/79/10/106801

Bouman, J., Koop, R., Tscherning, C. C., & Visser, P. (2004). Calibration of GOCE SGG data using high-low SST, terrestrial gravity data and global gravity field models. *Journal of Geodesy*, *78*(1-2). https://doi.org/10.1007/s00190-004-0382-5

Bouman, J., Fiorot, S., Fuchs, M., Gruber, T., Schrama, E., Tscherning, C., Veicherts, M., & Visser, P. (2011). GOCE gravitational gradients along the orbit. *Journal of Geodesy*, *85*(11), 791–805. https://doi.org/10.1007/s00190-011-0464-0

Bruinsma, S., Sutton, E., Solomon, S. C., Fuller Rowell, T., & Fedrizzi, M. (2018). Space Weather Modeling Capabilities Assessment: Neutral Density for Orbit Determination at low Earth orbit. *Space Weather*, *16*(11), 1806–1816. https://doi.org/10.1029/2018SW002027

Cesare, S., Dionisio, S., Saponara, M., Bravo-Berguño, D., Massotti, L., Teixeira da Encarnação, J., & Christophe, B. (2022). Drag and Attitude Control for the Next Generation Gravity Mission. *Remote Sensing*, *14*(12), 2916. https://doi.org/10.3390/rs14122916

Cesare, S., & Sechi, G. (2013). Next Generation Gravity Mission. In M. D'Errico (Ed.), *Distributed Space Missions for Earth System Monitoring* (pp. 575–598). Springer.

Chen, J. L., Wilson, C. R., & Tapley, B. D. (2006). Satellite Gravity Measurements Confirm Accelerated Melting of Greenland Ice Sheet. *Science*, *313*(5795), 1958–1960. https://doi.org/10.1126/science.1129007

Christophe, B., Boulanger, D., Foulon, B., Huynh, P.-A., Lebat, V., Liorzou, F., & Perrot, E. (2015). A new generation of ultra-sensitive electrostatic accelerometers for GRACE Follow-on and towards the next generation gravity missions. *Acta Astronautica*, *117*, 1–7. https://doi.org/10.1016/j.actaastro.2015.06.021

Christophe, B., Foulon, B., Liorzou, F., Lebat, V., Boulanger, D., Huynh, P.-A., Zahzam, N., Bidel, Y., & Bresson, A. (2018). Status of Development of the Future Accelerometers for Next Generation Gravity Missions. In J. T. Freymueller & L. Sánchez (Eds.), *International Symposium on Advancing Geodesy in a Changing World* (pp. 85–89, Vol. 149). Springer International Publishing. https://doi.org/10.1007/1345_2018_42

Danzmann, K. (2000). LISA mission overview. *Advances in Space Research*, *25*(6), 1129–1136. https://doi.org/10.1016/S0273-1177(99)00973-4

Dionisio, S., Anselmi, A., Bonino, L., Cesare, S., Massotti, L., & Silvestrin, P. (2018). The "Next Generation Gravity Mission": Challenges and consolidation of the system concepts and technological innovations. *2018 SpaceOps Conference*. https://doi.org/10.2514/6.2018-2495

Dirkx, D., Fayolle, M., Garrett, G., Avillez, M., Cowan, K., Cowan, S., Encarnacao, J., Lombrana, C. F., Gaffarel, J., Hener, J., Hu, X., Nistelrooij, M. v., Oggionni, F., & Plumaris, M. (2023, September). *The open-source astrodynamics Tudatpy software - overview for planetary mission design and science analysis* (tech. rep. No. EPSC2022-253). Europlanet Science Congress 2022. Granada, Spain. https://doi.org/10%20.5194/epsc2022-253

Drinkwater, M. R., Floberghagen, R., Haagmans, R., Muzi, D., & Popescu, A. (2003). GOCE: ESA's First Earth Explorer Core Mission. *Space Science Reviews*, *108*(1/2), 419–432. https://doi.org/10.1023/A:1026104216284

Elsaka, B., Raimondo, J.-C., Brieden, P., Reubelt, T., Kusche, J., Flechtner, F., Iran Pour, S., Sneeuw, N., & Müller, J. (2014). Comparing seven candidate mission configurations for temporal gravity field retrieval through full-scale numerical simulation. *Journal of Geodesy*, *88*(1), 31–43. https://doi.org/10.1007/s00190-013-0665-9

Encarnação, J., Siemes, C., Daras, I., Carraz, O., Strangfeld, A., Zingerle, P., & Pail, R. (2024). Towards a realistic noise modelling of quantum sensors for future satellite gravity missions [Archive: arXiv, print: 2404.07835].

ESA, Daras, I., March, G., Mass Chnge Mission Expert Group, J., Wiese, D., Blackwood, C., Forman, F., Loomis, B., Luthcke, S., Peralta-Ferriz, C., Sauber-Rosenberg, J., Eicker, A., Panet, I., Visser, P., Meyssignac, B., Wouters, B., Bamber, J., Pail, R., & Flechtner, F. (2023, September). *Next Generation Gravity Mission (NGGM) Mission Requirements Document* (tech. rep.). ESA.

Flechtner, F., Neumayer, K.-H., Dahle, C., Dobslaw, H., Fagiolini, E., Raimondo, J.-C., & Güntner, A. (2016). What Can be Expected from the GRACE-FO Laser Ranging Interferometer for Earth Science Applications? *Surveys in Geophysics*, *37*(2), 453–470. https://doi.org/10.1007/s10712-015-9338-y

Flechtner, F., Reigber, C., Rummel, R., & Balmino, G. (2021). Satellite Gravimetry: A Review of Its Realization. *Surveys in Geophysics*, *42*(5), 1029–1074. https://doi.org/10.1007/s10712-021-09658-0

Floberghagen, R., Fehringer, M., Lamarre, D., Muzi, D., Frommknecht, B., Steiger, C., Piñeiro, J., & Da Costa, A. (2011). Mission design, operation and exploitation of the gravity field and steady-state ocean circulation explorer mission. *Journal of Geodesy*, *85*(11), 749–758. https://doi.org/10.1007/s00190-011-0498-3

Frommknecht, B., Oberndorfer, H., Flechtner, F., & Schmidt, R. (2003). Integrated sensor analysis for GRACE – development and validation. *Advances in Geosciences*, *1*, 57–63. https://doi.org/10.5194/adgeo-1-57-2003

Frommknecht, B., Lamarre, D., Meloni, M., Bigazzi, A., & Floberghagen, R. (2011). GOCE level 1b data processing. *Journal of Geodesy*, *85*(11), 759–775. https://doi.org/10.1007/s00190-011-0497-4

Goswami, S., Francis, S. P., Bandikova, T., & Spero, R. E. (2021). Analysis of GRACE Follow-On Laser Ranging Interferometer Derived Inter-Satellite Pointing Angles. *IEEE Sensors Journal*, *21*(17), 19209–19221. https://doi.org/10.1109/JSEN.2021.3090790

Haagmans, R., Siemes, C., Massotti, L., Carraz, O., & Silvestrin, P. (2020). ESA's next-generation gravity mission concepts. *Rendiconti Lincei. Scienze Fisiche e Naturali*, *31*(S1), 15–25. https://doi.org/10.1007/s12210-020-00875-0

Harris, F. (1978). On the use of windows for harmonic analysis with the discrete Fourier transform. *Proceedings of the IEEE*, *66*(1), 51–83. https://doi.org/10.1109/PROC.1978.10837

Helleputte, T. V., Doornbos, E., & Visser, P. (2009). CHAMP and GRACE accelerometer calibration by GPS-based orbit determination. *Advances in Space Research*, *43*(12), 1890–1896. https://doi.org/10.1016/j.asr.2009.02.017

Herceg, M., Jørgensen, P., & Jørgensen, J. (2017). Characterization and compensation of thermo-elastic instability of SWARM optical bench on micro Advanced Stellar Compass attitude observations. *Acta Astronautica*, *137*, 205–213. https://doi.org/10.1016/j.actaastro.2017.04.018

Ince, E. S., & Pagiatakis, S. D. (2017). GOCE Gradiometer Measurements Response to Ionospheric Dynamics. *Journal of Geophysical Research: Space Physics*, *122*(10), 10, 712–10, 726. https://doi.org/10.1002/2017JA023890

Josselin, V., Rodrigues, M., & Touboul, P. (2001). INERTIAL SENSOR CONCEPT FOR THE GRAVITY WAVE MISSIONS. *Acta Astronautica*, *49*(2), 95–103. https://doi.org/10.1016/S0094-5765(00)00159-4

Knocke, P., Ries, J., & Tapley, B. (1988). Earth radiation pressure effects on satellites. *Astrodynamics Conference*. https://doi.org/10.2514/6.1988-4292

Kornfeld, R. P., Arnold, B. W., Gross, M. A., Dahya, N. T., Klipstein, W. M., Gath, P. F., & Bettadpur, S. (2019). GRACE-FO: The Gravity Recovery and Climate Experiment Follow-On Mission. *Journal of Spacecraft and Rockets*, *56*(3), 931–951. https://doi.org/10.2514/1.A34326

Landerer, F. W., Flechtner, F. M., Save, H., Webb, F. H., Bandikova, T., Bertiger, W. I., Bettadpur, S. V., Byun, S. H., Dahle, C., Dobslaw, H., Fahnestock, E., Harvey, N., Kang, Z., Kruizinga, G. L. H., Loomis, B. D., McCullough, C., Murböck, M., Nagel, P., Paik, M., … Yuan, D.-N. (2020). Extending the Global Mass Change Data Record: GRACE Follow On Instrument and Science Data Performance. *Geophysical Research Letters*, *47*(12). https://doi.org/10.1029/2020GL088306

Markley, F. L., & Crassidis, J. L. (2014). *Fundamentals of Spacecraft Attitude Determination and Control*. Springer New York.

Massotti, L., Amata, G. B., Anselmi, A., Cesare, S., Martimort, P., & Silvestrin, P. (2020, September). Next generation gravity mission: Status of the design and discussion on alternative drag compensation scenarios. In S. P. Neeck, T. Kimura, & A. Hélière (Eds.), *Sensors, Systems, and Next-Generation Satellites XXIV* (p. 8). SPIE. https://doi.org/10.1117/12.2573924

Massotti, L., Bulit, A., Daras, I., Carnicero Dominguez, B., Carraz, O., Hall, K., Hélière, A., March, G., Martimort, P., Rodrigues, G., Silvestrin, P., & Wallace, N. (2022, October). Next generation gravity mission design activities within the mass change and geoscience international constellation. https://indico.esa.int/event/416/contributions/7507/attachments/4913/7529/Clean%20Space%20Industrial%20Days_NGGM%20w_video_v3.pdf

Massotti, L., Siemes, C., March, G., Haagmans, R., & Silvestrin, P. (2021). Next Generation Gravity Mission Elements of the Mass Change and Geoscience International Constellation: From Orbit Selection to Instrument and Mission Design. *Remote Sensing*, *13*(19), 3935. https://doi.org/10.3390/rs13193935

McPherson, K., Kelly, E., & Keller, J. (2009). Acceleration Environment of the International Space Station. *47th AIAA Aerospace Sciences Meeting including The New Horizons Forum and Aerospace Exposition*. https://doi.org/10.2514/6.2009-957

Montenbruck, O., Van Helleputte, T., Kroes, R., & Gill, E. (2005). Reduced dynamic orbit determination using GPS code and carrier measurements. *Aerospace Science and Technology*, *9*(3), 261–271. https://doi.org/10.1016/j.ast.2005.01.003

Nati, M., Bernard, A., Foulon, B., & Touboul, P. (1994). ASTRE - A Highly Performant Accelerometer for the Low Frequency Range of the Microgravity Environment, 941366. https://doi.org/10.4271/941366

National Academies of Sciences, Engineering, and Medicine. (2018, December). *Thriving on Our Changing Planet: A Decadal Strategy for Earth Observation from Space*. National Academies Press.

National Research Council, Division on Earth and Life Studies, Commission on Geosciences, Environment and Resources, & Committee on Earth Gravity from Space. (1997, September). *Satellite Gravity and the Geosphere: Contributions to the Study of the Solid Earth and Its Fluid Envelopes* [ISBN: 978-0-309-05792-9]. National Academies Press.

Nicklaus, K., Cesare, S., Massotti, L., Bonino, L., Mottini, S., Pisani, M., & Silvestrin, P. (2019, July). Laser metrology concept consolidation for NGGM. In N. Karafolas, Z. Sodnik, & B. Cugny (Eds.), *International Conference on Space Optics — ICSO 2018* (p. 151). SPIE. https://doi.org/10.1117/12.2536071

Nicklaus, K., Voss, K., Feiri, A., Kaufer, M., Dahl, C., Herding, M., Curzadd, B. A., Baatzsch, A., Flock, J., Weller, M., Müller, V., Heinzel, G., Misfeldt, M., & Delgado, J. J. E. (2022). Towards NGGM: Laser Tracking Instrument for the Next Generation of Gravity Missions. *Remote Sensing*, *14*(16), 4089. https://doi.org/10.3390/rs14164089

O'Keefe, J. A., Eckeis, A., & Squires, R. K. (1959). Vanguard Measurements Give Pear-Shaped Component of Earth's Figure. *Science*, *129*(3348), 565–566. https://doi.org/10.1126/science.129.3348.565

Reigber, C., Bock, R., Förste, C., Grunwaldt, L., Jakowski, N., Lühr, H., Schwintzer, P., Tilgner, C., Gravity Field and Gravimetry -2009, G. C., 1. 0 Geodesy and Remote Sensing, D., & 1. 1 GPS/GALILEO Earth Observation, 1. 0. G. a. R. S. (1996). CHAMP Phase B: Executive Summary. https://doi.org/10.2312/gfz.b103-96131

Reigber, C., Balmino, G., Schwintzer, P., Biancale, R., Bode, A., Lemoine, J.-M., König, R., Loyer, S., Neumayer, H., Marty, J.-C., Barthelmes, F., Perosanz, F., & Zhu, S. Y. (2002). A high-quality global gravity field model from CHAMP GPS tracking data and accelerometry (EIGEN-1S). *Geophysical Research Letters*, *29*(14), 37–1–37–4. https://doi.org/10.1029/2002GL015064

Rispens, S., & Bouman, J. (2009). Calibrating the GOCE accelerations with star sensor data and a global gravity field model. *Journal of Geodesy*, *83*(8), 737–749. https://doi.org/10.1007/s00190-008-0290-1

Rummel, R., & Colombo, O. L. (1985). Gravity field determination from satellite gradiometry. *Bulletin géodésique*, *59*(3), 233–246. https://doi.org/10.1007/BF02520329

Rummel, R., Yi, W., & Stummer, C. (2011). GOCE gravitational gradiometry. *Journal of Geodesy*, *85*(11), 777–790. https://doi.org/10.1007/s00190-011-0500-0

Siemes, C. (2012). *Digital Filtering Algorithms for Decorrelation within Large Least Squares Problems* [Doctoral dissertation] [Doctoral dissertation, IGG].

Siemes, C. (2018). Improving GOCE cross-track gravity gradients. *Journal of Geodesy*, *92*(1), 33–45. https://doi.org/10.1007/s00190-017-1042-x

Siemes, C., Rexer, M., Schlicht, A., & Haagmans, R. (2019). GOCE gradiometer data calibration [b]. *Journal of Geodesy*, *93*(9), 1603–1630. https://doi.org/10.1007/s00190-019-01271-9

Smith, D. E., Kolenkiewicz, R., & Dunn, P. J. (1972). Geodetic Studies by Laser Ranging to Satellites. In *The Use of Artificial Satellites for Geodesy* (pp. 187–196). American Geophysical Union (AGU).

Smith, S. W. (1999). *The scientist and engineer's guide to digital signal processing* (2nd edition). California Technical Pub.

Stiller, D. (2023, August). *Short-term orbital effects of radiation pressure on the Lunar Reconnaissance Orbiter* (tech. rep.). TU Delft. https://repository.tudelft.nl/record/uuid:8a82400a-2233-4a84-98be-ed37f7eeb620

Strugarek, D., Sośnica, K., Arnold, D., Jäggi, A., Zajdel, R., Bury, G., & Drożdżewski, M. (2019). Determination of Global Geodetic Parameters Using Satellite Laser Ranging Measurements to Sentinel-3 Satellites. *Remote Sensing*, *11*(19), 2282. https://doi.org/10.3390/rs11192282

Stummer, C., Fecher, T., & Pail, R. (2011). Alternative method for angular rate determination within the GOCE gradiometer processing. *Journal of Geodesy*, *85*(9), 585–596. https://doi.org/10.1007/s00190-011-0461-3

Tapley, B. D., Bettadpur, S., Watkins, M., & Reigber, C. (2004). The gravity recovery and climate experiment: Mission overview and early results. *Geophysical Research Letters*, *31*(9). https://doi.org/10.1029/2004GL019920

Tapley, B. D., Watkins, M. M., Flechtner, F., Reigber, C., Bettadpur, S., Rodell, M., Sasgen, I., Famiglietti, J. S., Landerer, F. W., Chambers, D. P., Reager, J. T., Gardner, A. S., Save, H., Ivins, E. R., Swenson, S. C., Boening, C., Dahle, C., Wiese, D. N., Dobslaw, H., … Velicogna, I. (2019). Contributions of GRACE to understanding climate change. *Nature Climate Change*, *9*(5), 358–369. https://doi.org/10.1038/s41558-019-0456-2

Touboul, P., Foulon, B., Christophe, B., & Marque, J. P. (2012). CHAMP, GRACE, GOCE Instruments and Beyond. In S. Kenyon, M. C. Pacino, & U. Marti (Eds.), *Geodesy for Planet Earth* (pp. 215–221, Vol. 136). Springer Berlin Heidelberg.

Touboul, P., Foulon, B., Rodrigues, M., & Marque, J. (2004). In orbit nano-g measurements, lessons for future space missions. *Aerospace Science and Technology*, *8*(5), 431–441. https://doi.org/10.1016/j.ast.2004.01.006

Touboul, P., Métris, G., Sélig, H., Traon, O. L., Bresson, A., Zahzam, N., Benavent, C., & Rodrigues, M. (2016). Gravitation and Geodesy with Inertial Sensors, from Ground to Space. (12).

Touboul, P., Willemenot, E., Foulon, B., & Josselin, V. (1999). Accelerometers for CHAMP, GRACE and GOCE space missions: Synergy and evolution. *Bulletin of Geophysics and Oceanography*, *40*(3-4), 321–327.

Touboul, P., Foulon, B., & Willemenot, E. (1999). Electrostatic space accelerometers for present and future missions. *Acta Astronautica*, *45*(10), 605–617. https://doi.org/10.1016/S0094-5765(99)00132-0

Visser, P. N. A. M. (2008). Exploring the possibilities for star-tracker assisted calibration of the six individual GOCE accelerometers. *Journal of Geodesy*, *82*(10), 591–600. https://doi.org/10.1007/s00190-007-0205-6

Visser, P. N. A. M., & van den IJssel, J. A. A. (2016). Calibration and validation of individual GOCE accelerometers by precise orbit determination. *Journal of Geodesy*, *90*(1), 1–13. https://doi.org/10.1007/s00190-015-0850-0

Visser, P. (2007). GOCE gradiometer validation by GPS. *Advances in Space Research*, *39*(10), 1630–1637. https://doi.org/10.1016/j.asr.2006.09.014

Welch, P. (1967). The use of fast Fourier transform for the estimation of power spectra: A method based on time averaging over short, modified periodograms. *IEEE Transactions on Audio and Electroacoustics*, *15*(2), 70–73. https://doi.org/10.1109/TAU.1967.1161901

Wen, H. Y., Kruizinga, G., Paik, M., Landerer, F., Bertiger, W., Sakumura, C., Bandikova, T., & Mccullough, C. (2019, September). *Gravity Recovery and Climate Experiment Follow-On (GRACE-FO) Level-1 Data product User handbook* (tech. rep.). NASA Jet Propulstion Laboratory. https://podaac.jpl.nasa.gov/gravity/gracefo-documentation

Wertz, J. R., Everett, D. F., & Puschell, J. J. (Eds.). (2011). *Space mission engineering: The new SMAD*. Microcosm Press.

Willemenot, E., Touboul, P., & Josselin, V. (1999). Gradiometer calibration and performance verification: GOCE approach. *Bulletin of Geophysics and Oceanography*, *40*(3-4), 527–532.

Willis, P., Fagard, H., Ferrage, P., Lemoine, F. G., Noll, C. E., Noomen, R., Otten, M., Ries, J. C., Rothacher, M., Soudarin, L., Tavernier, G., & Valette, J.-J. (2010). The International DORIS Service (IDS): Toward maturity. *Advances in Space Research*, *45*(12), 1408–1420. https://doi.org/10.1016/j.asr.2009.11.018

Wolff, M. (1969). Direct measurements of the Earth's gravitational potential using a satellite pair. *Journal of Geophysical Research*, *74*(22), 5295–5300. https://doi.org/10.1029/JB074i022p05295

Wöske, F., Kato, T., Rievers, B., & List, M. (2019). GRACE accelerometer calibration by high precision non-gravitational force modeling. *Advances in Space Research*, *63*(3), 1318–1335. https://doi.org/10.1016/j.asr.2018.10.025